The Study of Various Anode Materials for Sodium (or Lithium)-Ion Batteries

By **Tao Li**

A thesis submitted for the degree of Doctor of Philosophy

DIBRIS, University of Genova

Italian Institute of Technology

February 2019

Table of contents

List of figures

List of tables

Acknowledgements

First I would like to express my sincere gratitude to my supervisors Prof. Remo Porietti and Prof. Claudio Capiglia for their kindness in accepting me as a student to do my PhD research in such an international institute of IIT. I really enjoy my collaboration with them. And their advice, support, and guidance helped me a lot in the last three years, allowing me to grow as a research scientist.

I am thankful to Prof. Francesco De Angelis (my coordinator) for providing me the opportunity to be a group member of him and funding me in the participation in international conferences. I would also like to thank Prof. Liberato Manna for allowing me to carry out my research activities in his Nanochemistry Lab which has such a good research environment.

Thanks to the technicians for their efforts in organizing the chemistry lab to provide a neat and orderly working environment and for their assistance on my research. A special thanks to the researchers Dr. Sergio Marras, Mirko Prato, Rosaria Brescia, and Zhiya Dang for their contributions to my publications and Ph.D. thesis for the materials physical measurements.

Many thanks to my colleague Dr. Umair Gulzar for his help, discussion, and friendly collaboration on different projects. Thanks also to all my friends in IIT and University of Genova. Thank for you the understanding and encouragement, and the happy time we had together.

Finally, I want to thank my grandparents, parents, sister, and fiancee. Words cannot express how grateful I am to them. Without your continuous support and endless love, I would not have achieved so much.

Declaration

This thesis is the result of my own work and includes nothing, which is the outcome of work done in collaboration except where specifically indicated in the text. It has not been previously submitted, in part or whole, to any university or institution for any degree, diploma, or other qualification.

Signed: Tao Li

Date: 06/02/2019

Tao Li
DIBRIS, University of Genova
Italian Institute of Technology

Abstract

Recently, room-temperature sodium-ion batteries (NIBs or SIBs) have raised a great deal of attention for grid-level applications considering the sustainability advantages of NIBs. Significant progress has been made for NIB cathodes by adapting the knowledge learned on lithium-ion batteries (LIBs). Simultaneously, numerous attempts have been made to find suitable anodes for NIBs, however, the research to improve NIB technologies remains a challenge. This thesis presents fundamental studies of various anode materials for NIBs from different aspects.

Surface and interface engineering of nanostructured anatase TiO_2 anode through Al_2O_3 surface modification and wise electrolyte selection is conducted. The results show that Al_2O_3 coating provides beneficial effects to the TiO_2-based anodes and the modified TiO_2 exhibits significant improvements in cycling performance using electrolyte with binary ethylene carbonate (EC) and propylene carbonate (PC) solvent mixture without the need of the commonly used fluoroethylene carbonate (FEC) additive. The achieved excellent electrochemical performance (a high reversible capacity of 188.1 mAh g^{-1} at 0.1C after 50 cycles, good rate capability up to 5C, and long-term cycling performance for 650 cycles at a high rate of 1C) can be ascribed to the synergistic effects of surface and interface engineering enabling the formation of a stable and highly ionic conductive interface layer in EC:PC based electrolyte which combines the native SEI film and an 'artificial' SEI layer of irreversibly formed Na−Al−O.

A dual-modification approach of Mo doping combined with AlF_3 coating is also introduced to enhance the sodium storage activity of anatase TiO_2. The Mo-doped anatase TiO_2 synthesized by a simple co-precipitation method delivers an enhanced reversible capacity compare to pristine TiO_2 (139.8 *vs.* 100.7 mAh g^{-1} at 0.1C after 50 cycles) due to enhanced electronic/ionic conductivity. Via further coating AlF_3 using a modified solid-state method, a much higher reversible capacity of 178.9 mAh g^{-1} with good cycle stability and excellent rate capabilities up to 10C can be finally obtained. The experimental results indicate that AlF_3 surface coating could effectively reduce solid electrolyte interfacial resistance, enhance electrochemical reactivity at the surface/interface region, and lower polarization during cycling.

As for alloy-type anode of Sn with high theoretical capacity of 847 mAh g^{-1} but experiences a high volume expansion of 420% upon sodiation, we carry out a fundamental study of the degradation mechanisms that occur in Sn during sodiation-desodiation by employing a Sn thick film as the anode. Electron microscopy reveals new deformation mechanisms, as multiple Sn whiskers nucleate on the surface of the Sn, while pores form within the Sn (over the Na-ion penetration distance) after electrochemical cycling. These mechanisms are in addition to the dry lake-bed fracture that is also observed. Such whiskers and pores may be more-subtle at the

nanoscale, and therefore have not been reported for sub-micron Sn particles in porous electrodes. The simplified planar geometry of the Sn sheet allows to dispense with the influence of the binder and carbon additives that are required in porous electrodes and the implementation of the Randles-Sevick equation provides a first experimental estimate for the diffusion coefficient of Na^+ in Sn as 6.45×10^{-12} cm^2 s^{-1}.

Finally, we explore facile synthesis of carbon materials from low cost carbon source of CaC_2 using a novel sulfur-based thermo-chemical etching technique. Comprehensive analysis using X-ray diffraction (XRD), Raman spectroscopy, X-ray photoelectron spectroscopy (XPS) and N_2 adsorption−desorption isotherms, reveals a highly graphitized mesoporous structure for the CaC_2-derived carbon with a specific surface area of 159.5 m^2 g^{-1}. Microscopic analysis displays micron-scale mesoporous frameworks (4–20 μm) with a distinct layered structure along with agglomerates of highly graphitized nanosheets (about 10 nm in thickness and 1–10 μm of lateral size). The application of the as-prepared carbon materials as anode for NIBs and LIBs is also preliminarily studied.

Chapter 1 Introduction

Sodium-ion batteries (NIBs or SIBs) have been considered as the most promising candidate for large-scale energy storage system (ESS) owing to the economic efficiency resulting from abundant sodium resources, superior safety, and similar chemical properties to the commercial lithium-ion batteries (LIBs).[1] *The practical commercialization of NIBs and their use in large-scale electrical energy storage (EES) technology for renewable energy sources (e.g., wind, solar, etc.) in the near future will surely bring our modern society significant influences.*

1.1 The development and principle of sodium-ion batteries

Historically, the study of Na^+ ions as charge carriers for electrochemical energy storage at ambient temperature started before 1980, almost at the same stage when the study of rechargeable lithium batteries namely the currently so-called lithium-ion batteres (LIBs) started. In 1980, electrochemical and highly reversible sodium insertion into TiS_2 at room temperature was demonstrated immediately after the report in 1970s of electrochemical lithium insertion into TiS_2 and its application for energy storage devices.[2,3] Also in 1980, $LiCoO_2$, which is a lithium-containing layered cobalt oxide and is still widely used as high energy positive electrode materials in LIBs, was first reported.[4] Inspired by this finding, similarly, the electrochemical properties of sodium containing layered oxides, Na_xCoO_2, were also reported later.[5] However, the available energy density of Na system was much lower compared with the Li system due to the different chemistry of Na from Li. Thus, after 1980, significant research work was conducted only for LIBs, and studies on NIBs materials almost disappeared. Research interest of LIBs was further accelerated by the finding of graphite, which delivers high reversible capacity (theoretically 372 mAh g^{-1}) with a low and flat

operating potential (0.1−0.2 V *vs* Li^+/Li), and finally led to the first commercialization of LIBs, graphite//$LiCoO_2$ cell, in 1991 by SONY. Another important reason for the standstill of development of NIBs was the absence of suitable negative electrodes for a long period of time as Na cannot be inserted into the graphite layer and there was only a few studies on potential negative electrode materials for NIBs before 1990s.[6]

In 2000, the research for NIBs witnessed its first turning point, as Stevens and Dahn reported a high reversible capacity of 300 mAh g^{-1} with hard carbon, which is now extensively studied as an anode material for NIBs.[7] Then in 2006 Okada and coworkers reported that $NaFeO_2$ is electrochemically active in Na cells based on the Fe^{3+}/Fe^{4+} redox couple.[8] These new findings were crucial for the development of NIBs electrode materials. Today the research interest for NIBs is changing because of those important findings and because of the controversial debates regarding the limited global lithium reserves and higher cost to obtain Li, and considering the increasing worldwide demand for electric vehicles (EVs) and ESS with large-scale batteries. Therefore, though LIBs are still the dominate energy storage devices in the market until now, the number of publications on NIBs has drastically increased in recent years after 2010 indicating the increasing interests in NIBs and some promising progress on sodium-ion-based full-cell system has been achieved.[1,6,9,10]

NIBs operate at ambient temperature, and are different from the already commercialized Na-based technology, *e.g.*, Na/S and Na/$NiCl_2$ batteries.[6] These batteries usually operate at high temperature (~ 300 ºC) with alumina-based solid (ceramic) electrolyte and molten sodium and sulfur as active materials, which induces safety issue that is still a tough problem for large-scale applications. Naturally, research interest in NIBs that could operate at room-temperature is renewed recently because of the abundance and low cost of sodium resources.

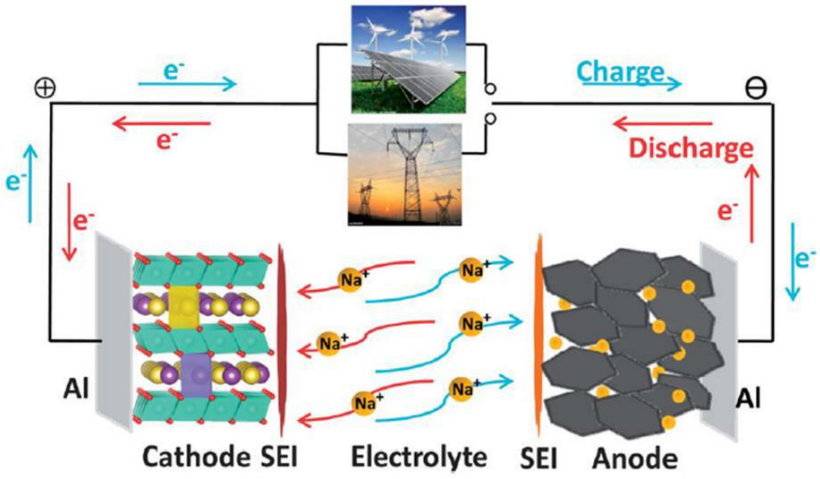

Figure 1.1 Schematic illustration of room-temperature "rocking chair" sodium-ion batteries.[9]

The working principle of room-temperature "rocking-chair" NIBs is similar to that of LIBs as the structures, components, and charge storage mechanisms of NIBs are essentially the same for LIBs except that lithium ions are replaced with sodium ions. Figure 1.1 shows the schematic illustration of a room-temperature NIB. A NIB consists of two sodium insertion materials, positive electrode (cathode side, where reduction takes place during discharge) and negative electrode (anode side, where oxidation takes place during discharge), and an electrically insulated electrolyte (in general, electrolyte salts dissolved in aprotic polar solvents) soaked in a separator between the two electrodes. During charge process, an oxidation reaction occurs at the cathode side with Na de-insertion and electron loss. The Na^+ ions migrate to the anode side through the electrolyte, and electrons simultaneously transfer to the anode via external circuit to keep charge balance. This leads to a reduction reaction occurring at the anode with Na insertion. The opposite process occurs during discharge. The Na^+ ions as charge carriers migrate back and forth between the cathode and anode during repeated charge and discharge processes, just like a "rocking chair", thus we call the battery a "rocking chair" NIB. Take an example, if in a NIB system the cathode materials and anode materials are layered $NaMnO_2$ and hard carbon, respectively, the charge/discharge mechanism can be represented by the following chemical reactions:

Charge

$$\text{Cathode: } NaMnO_2 \rightarrow Na_{1-x}MnO_2 + xNa^+ + xe^- \quad (1)$$

$$\text{Anode: } C + xNa^+ + xe^- \rightarrow Na_xC \quad (2)$$

$$\text{Overall: } NaMnO_2 + C \rightarrow Na_{1-x}MnO_2 + Na_xC \quad (3)$$

Discharge

$$\text{Cathode: } Na_{1-x}MnO_2 + xNa^+ + xe^- \rightarrow NaMnO_2 \quad (4)$$

$$\text{Anode: } Na_xC \rightarrow C + xNa^+ + xe^- \quad (5)$$

$$\text{Overall: } Na_{1-x}MnO_2 + Na_xC \rightarrow NaMnO_2 + C \quad (6)$$

1.2 Comparison between sodium-ion batteries and lithium-ion batteries

With the rapid development of our modern society, the traditional energy supplied from fossil fuels cannot meet the increasing demands. Meanwhile, the environmental problems resulting from the continuous consumption of the fossil fuels and their limited resources have spurred us to exploit renewable and green energy sources such as solar and wind. However, these renewable energy sources are variable in time. Therefore, to smooth out the intermittency of renewable energy production, large-scale EES technology will become necessary.[11] LIBs, one of the most important electrochemical energy storage technologies, have been widely used in portable electronic devices, EVs, and hybrid EVs due to their high output voltages, high energy densities, and long cycle life.[12] Although LIBs potentially provide a solution to meet the above mentioned tough challenges, we must reconsider the feasibility of lithium. Indeed, the cost of lithium raw materials is increasing in recent years with the increasing market for electric vehicles. Therefore, there is an urgent and desired need to explore low-cost alternatives based on abundant resources. In this case, NIB technology is considered to be a promising system as a substitute for LIBs due to the lower price, natural abundance, and similar intercalation chemistry.

As shown in Table 1, the cost of sodium is much lower than that for lithium

because it is very abundant in the Earth's crust compared with lithium (Figure 1.2a) and the sodium resource are everywhere and also found in the ocean. However, it must be pointed out that the gravimetric and volumetric densities of NIB would not exceed those of its Li analogue because of the relatively heavier and larger Na atom and less-reducing potential of Na (Table 1).[9] However, energy density is not a critical issue in the field of large-scale ESS where cost and safety are more concerned. Thus, developing room-temperature NIBs is still a reasonable alternative.

Table 1. 1 The comparison between Na and Li elements.[6,9]

Characteristics	Na	Li
Shannon's ionic radii	1.02 Å	0.76 Å
Atomic weight	23 g mol^{-1}	6.94 g mol^{-1}
E^o *vs.*SHE[a]	−2.71 V	−3.04 V
Melting point	97.7 ºC	180.5 ºC
Distribution	Everywhere	70% in South America
Price (for carbonates)[12]	~ 0.5 US $ per kg[b]	~ 13.9 US $ per kg[b]

[a] SHE: Standard Hydrogen Electrode. [b] Battery grade (≥99.5%).

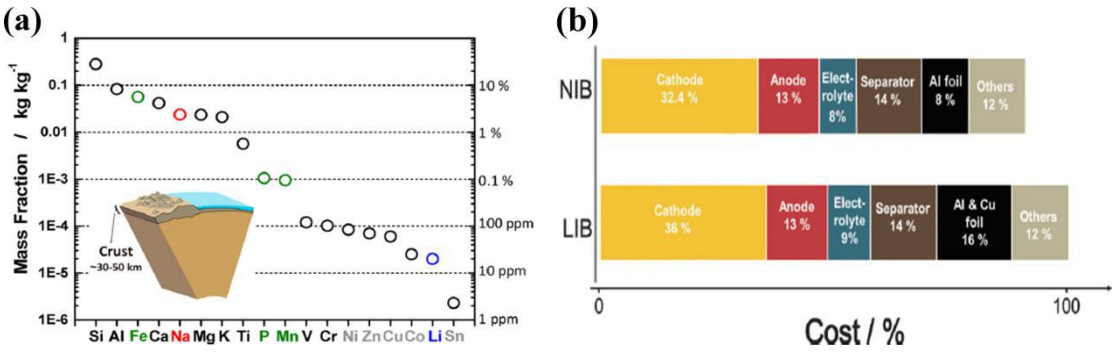

Figure 1.2 (a) Elemental abundance in the Earth's crust.[6] *(b) Comparison of the manufacturing costs for LIBs and NIBs.*[14]

Another point in favour of NIBs is that aluminium can be used as the current collector for the anode, which is different from LIBs where copper foil must be used

for the anode as lithium forms a binary alloy with aluminium while sodium does not alloy with aluminium at low potentials.[13] By replacing the conventional, heavier and more expensive copper anode current collector with an aluminium anode current collector, the performance decrease of NIBs owing to the drawbacks of sodium compared with lithium can be mitigated, and in particular, the cost of the battery can be lower. Therefore, NIBs are considered to be potentially about 10% less expensive in total cost than commercialized LIBs (Figure 1.2b), assuming they deliver the same energy density.[12,14] In addition, the expensive and flammable organic liquid electrolyte for NIBs can be replaced by aqueous electrolytes, and cheap inorganic Na salts, such as Na_2SO_4, NaCl, and $NaNO_3$, can be used in a large-scale, which could further enhance the safety and decrease the cost.[9,15,16] Thus developing aqueous NIBs rather than LIBs is another important aspect and trend.

1.3 Electrode materials of sodium-ion batteries

For a NIB (full cell), the difference in the electrochemical potential between the two electrode materials (cathode and anode, as illustrated in Figure 1.1) provides the theoretical voltage (V). The charge storage capacity of an electrode material (C), determined by the ability of the material to uptake a certain amount of Na ions, is often expressed by gravimetric (Ah g^{-1}) or volumetric (Ah cm^{-3}) units. Gravimetric charge storage capacity is often named specific capacity and is most commonly reported in units of mAh g^{-1}. Figure 1.3 displays the theoretical specific capacities and voltages of some known NIB cathode and anode materials. In the following part a brief overlook of the currently studied various classes of active cathode and anode materials is provided. Specifically, on the cathode side two most extensively studied topics of layered transition metal oxides and polyanionic compounds will be introduced while on the anode side, the most widely studied and promising materials like carbon-based materials, Ti-based compounds, and Na alloys and compounds will be discussed.

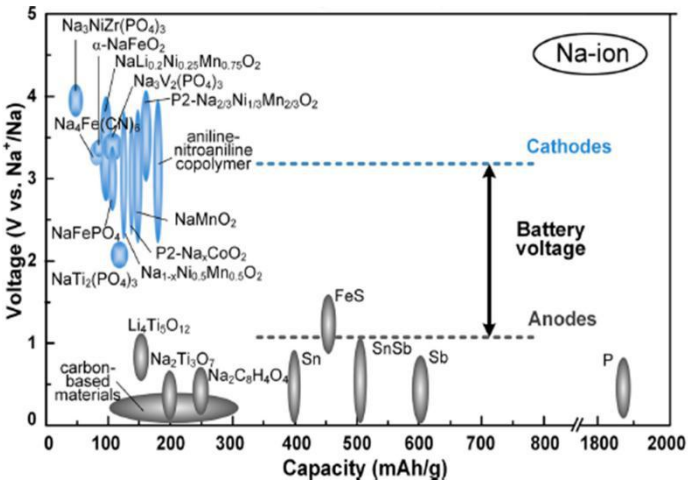

Figure 1.3 Capacities and voltages of some known cathode and anode materials for sodium-ion batteries.[17]

1.3.1 Cathode materials

1.3.1.1 Layered transition metal oxides

Na-based layered transition metal oxides (TMOs) of general formula Na_xMeO_2 (Me = 3d transition metal, *e.g.*, Ni, Co, Mn, Fe, Cr, V, Ti, *etc*.) can reversibly intercalate Na^+ ions, most of which can be used as cathode materials (except for low potential $NaTiO_2$), because of their high redox potentials and high theoretical capacities.[18] Layered Na_xMeO_2 are built up of repeating sheets of edge-sharing MeO_6 octahedra layers with Na ions being sandwiched in between the oxide layers. As shown in Figure 1.4, typical Na-based layered TMOs can be categorized into four main groups P3, O3, P2, and O2 type depending on the surrounding Na environment and the number of unique oxide layer packings. The letter indicates the environment where Na ions are accommodated (O: octahedral, P: prismatic) and the number indicates the number of crystallographic different MeO_2 layers within each unit cell. Sodium extraction from O3- and P2-type phases generally induces phase transitions (O3→O'3→P3→P'3 and P2→O2, respectively, the prime symbol (') indicates a distorted phase) due to the gliding of MeO_2 slabs but without breaking Me−O bonds.[5] O3- and P2-type phases are the most-common structural polymorphs and hot topics of layered oxides which being widely studied as cathodes for NIBs because they are

stable phases at high temperatures and can be easily synthesized in air by solid-state reactions, co-precipitation routes, and hydrothermal methods.[19] The most widely investigated P2-type layered materials are Na_xCoO_2 and Na_xMnO_2 with x around 0.7 while the commonly studied O3-type layered materials are Na_xMeO_2 with Me = Mn, Cr, Fe, and Ni with the Na content x close to 1.

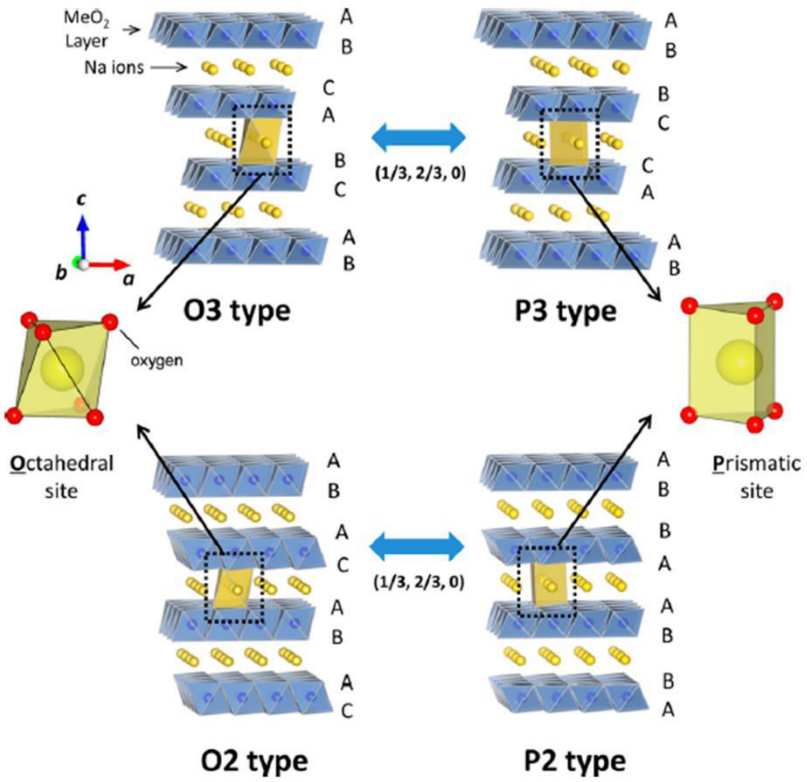

Figure 1.4 Classification of layered TMO materials with sheets of edge-sharing MeO_6 octahedra and phase transition processes induced by sodium extraction.[15]

Detailed discussion on performance and sodium storage mechanisms of each kind of these widely investigated P2- and O3-type layered materials have been reported in many review articles[6,9,10,18–21] and thus will not be given here. Compared with the Li-based intercalation metal oxide Li_xMeO_2 in LIB systems, the Na_xMeO_2 having the same Me for NIBs behaves quiet differently showing more complicated electrochemical behaviors accompanied by structural evolution during reversible charge and discharge, owing to the large ionic radius of the Na^+ ion. Deep insertion or de-insertion of Na^+ ions inevitably causes large expansion or shrinkage of the lattice volume and easily induces irreversible phase transformations, leading to capacity

fading. Strategies like forming mixed cation oxides, doping or cationic substitution with inactive metals, surface modification, and morphology tuning have been shown to be effective to enhance the structural stability and reaction kinetics thus to improve the cycling performance.

1.3.1.2 Polyanionic compounds

This class of compounds derives its name from the tetrahedral XO_4 and trigonal XO_3 groups that partially replace MeO_6 octahedral metal clusters. Polyanionic compounds feature a 3D open-framework structure created by edge or corner sharing polyhedrons, which is permeated by straight or tangled channels with relatively low Na^+ diffusion energies. In comparison with the layered TMOs, polyanionic compounds have shown significant structural stability, thermal safety, and an overall higher operating voltage, attributing to the strong inductive effect arising from the large anion groups (formed by *e.g.* P–O covalent bonds) with high electronegativity.[18] Therefore, a variety of polyanionic compounds are being intensively pursued as promising Na intercalation host for NIB cathode.

Figure 1.5 shows the crystal structures of representative polyanionic cathode materials: phosphates ($NaMPO_4$, NASICON (Na^+ superionic conductor)-type $Na_3V_2(PO_4)_3$), pyrophosphates ($Na_2MP_2O_7$, $Na_4M_3(PO_4)_2P_2O_7$), and fluorophosphates (Na_2MPO_4F, $Na_3M_2(PO_4)_2F_3$) (M = Fe, Co, Mn). By anion substitution with F^- ion (fluorination) or transition metal substitution (doping) in polyanionic compounds, many new phosphate-class materials could be obtained with improved performances in terms of specific capacity, cycling stability or operational voltage owing to the enhanced Na diffusion and/or enhanced electronic conductivity after modification.[10,18,20] In addition to these widely studied phosphate-class polyanionic compounds, other polyanion-type compounds like transition metal sulfates $Na_xM_y(SO_4)_z$ and silicates Na_2MSiO_4 (M = Fe, Co, Mn) are also being considered as cathode candidates.

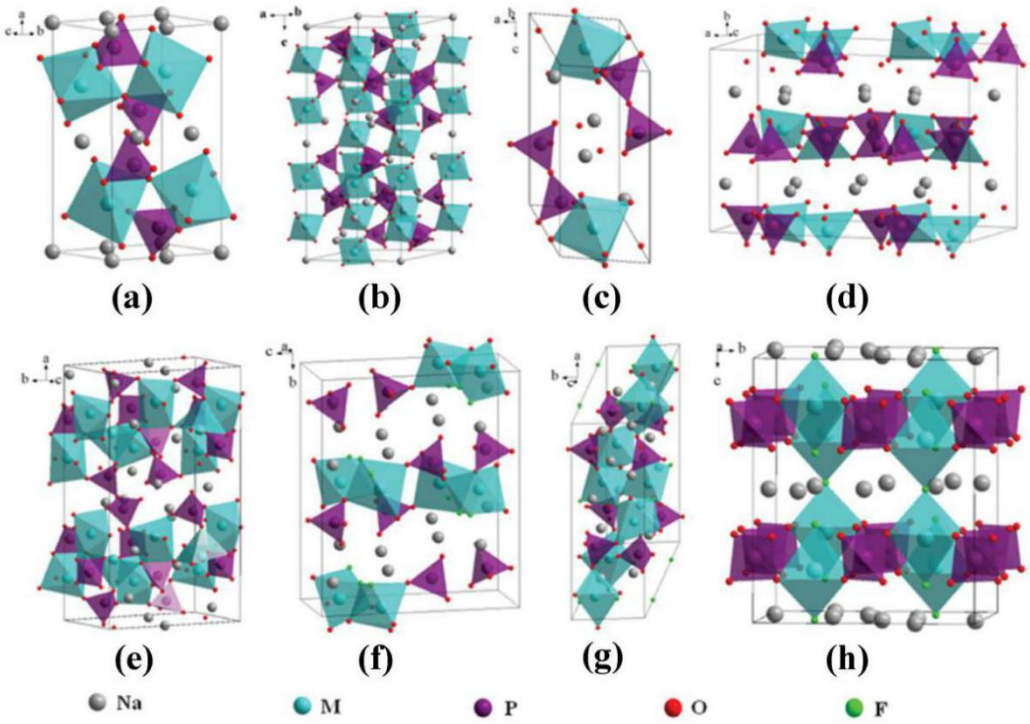

Figure 1.5 Crystal structures of (a) olivine $NaMPO_4$, (b) NASICON $Na_3V_2(PO_4)_3$, (c) triclinic $Na_2MP_2O_7$, (d) orthorhombic $Na_2MP_2O_7$, (e) orthorhombic $Na_4M_3(PO_4)_2P_2O_7$, (f) orthorhombic Na_2MPO_4F, (g) monoclinic Na_2MPO_4F, and (h) tetragonal $Na_3M_2(PO_4)_2F_3$ (M represents transition metals).[19]

However, polyanionic compounds usually suffer from a low electron conductivity, which limits their rate performance. Combining carbon incorporation, particle nanosizing, and pore design to fabricate porous micro-/nanostructures is an effective strategy to enhance the rate performance due to a large improvement of the reaction kinetics.[19] The carbon network enables fast electron conduction and improved structural integrity of the cathode particles, the particle nanosizing shortens the diffusion paths of Na^+ while the hierarchical structure could increase the specific surface area of the material and therefore ensures sufficient contact with the electrolyte. Furthermore, though the high operating potential is a typical advantage of polyanionic compounds, high-potential reactions are usually accompanied by electrolyte decomposition, therefore electrolyte optimization is necessary and the effect of the electrolyte system on the performance needs to be systematically studied to meet the practical application of high power NIBs.

1.3.1.3 Other cathode materials

Other Na insertion hosts like metal hexacyanometalates (prussian blue analogues) $KM[Fe(CN)_6]$ and $Na_xM[M'(CN)_6]$ (M and M′ = Fe, Co, Mn, Ni), organic compounds (*e.g.*, aromatic carbonyl derivatives, pteridine derivatives, and polymers), and some conversion-type materials like metal fluorides have also been tested as cathodes for NIBs.[6,18–21]

1.3.2 Anode materials

1.3.2.1 Carbon-based materials

Graphitic carbon

Graphite, the most commonly used anode in LIBs, does not intercalate sodium to any appreciable extent due to the fact that sodium hardly forms staged intercalation compounds with graphite because is electrochemically less active. In 2014, Adelhelm *et al.* reported a co-intercalation approach to form a Na−solvent−graphite ternary graphite intercalation compounds (GICs) anode for NIBs.[22] With the use of a diglyme-based electrolyte, the graphite exhibited a reversible capacity of about 100 mAh g^{-1} at 0.1 C with a potential plateau at 0.6 V. Later, Kang *et al.* found that the natural graphite could also deliver a reasonable performance with a capacity of 150 mAh g^{-1} over 2500 cycles in ether-based electrolytes.[23] However, capacity of graphite achieved by co-intercalation approach is relatively low and co-intercalation of solvents causes a high level of volume change, limiting its practical application. On the other hand, Wang *et al.* proposed another method to utilize graphite by expanding its interlayer distance to 0.43 nm from its typical value of 0.34 nm.[24] The expanded graphite (EG) is a graphite-derived material formed by a two-step oxidation−reduction process that retains the long range-ordered layered structure of graphite, as schematized in Figure 1.6a. As a result, the EG delivers a moderate capacity of 284 mAh g^{-1} at a current density of 20 mA g^{-1} and a good capacity retention of 73.92% after 2000 cycles at 100 mA g^{-1}. In their work, the Na^+

intercalation mechanism of the EG material through reversible interlayer expansion/shrinkage during sodiation/desodiation has also been confirmed by cyclic voltammetry and *in situ* TEM observations .

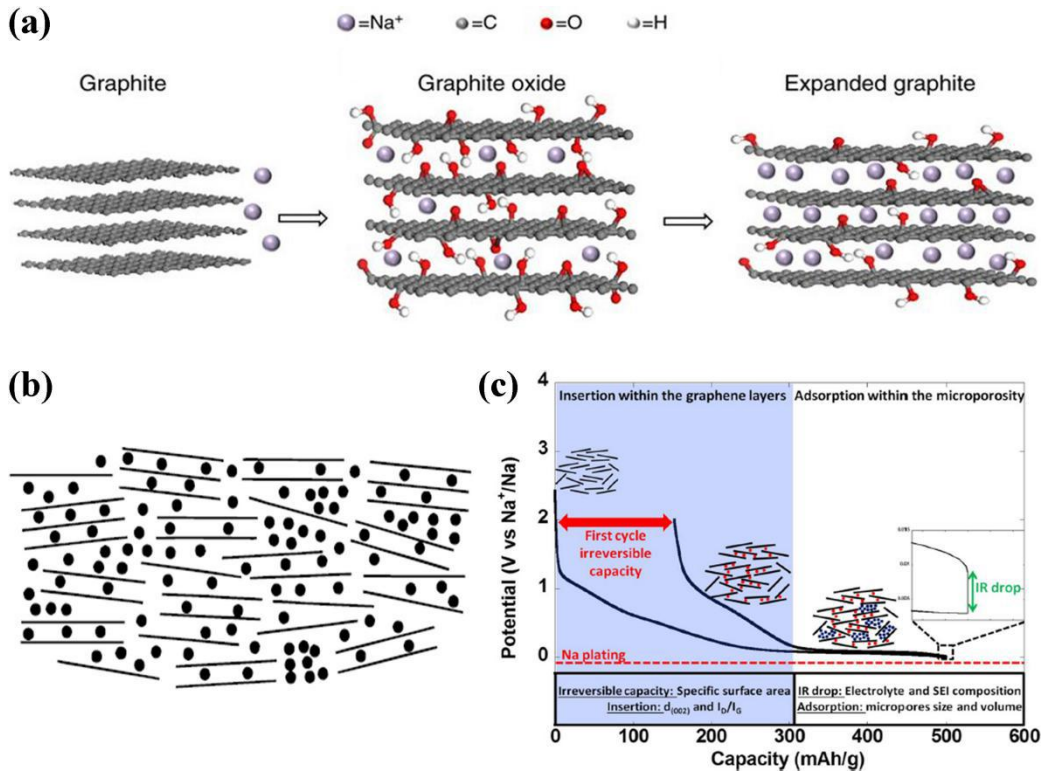

Figure 1.6 (a) Schematic illustration of sodium storage in graphite-based materials. (left) Na^+ cannot be electrochemically intercalated into graphite because of the small interlayer spacing. (middle) Electrochemical intercalation of Na^+ into graphite oxide is enabled by the enlarged interlayer distance because of oxidation. However, the intercalation is limited by steric hindering from large amounts of oxygen-containing groups. (right) A significant amount of Na^+ can be electrochemically intercalated into expanded graphite owing to suitable interlayer distance and reduced oxygen-containing groups in the interlayers.[24] (b) "House of cards" model for sodium filled hard carbon.[7] (c) Typical potential vs. capacity profile for hard carbon when tested against sodium metal counter electrodes.[26]

Hard carbon

Hard carbon, also known as non-graphitizable carbon, cannot be graphitized through thermal treatment. They can be obtained from solid-phase pyrolysis of phenol-formaldehyde resins, cellulose, charcoal, sugar, coconut and other biomass wastes. In 2000, Stevens and Dahn first demonstrated the reversible insertion of

sodium into hard-carbon host structures at room temperature.[7] The hard carbon prepared by carbonization of glucose at 1000 ºC exhibits a reversible capacity of 300 mAh g^{-1}. To interpret the data the authors proposed a "house of cards" model for sodium filled hard-carbon, as shown in Figure 1.6b, where expanded graphitic domains are randomly arranged conveying a microporous structure to the carbon structure. They attribute the sloping potential profile to insertion of sodium between parallel or nearly parallel layers and the low-potential plateau to insertion of sodium into the nanopores between randomly stacked layers through a process analogous to adsorption.[7] The involved mechanisms in sodium uptake were studied in detail later by their *in situ* X-ray scattering study of carbon materials in electrochemical cells, which verified the two-step storage mechanism proposed in the card-house model.[25] Figure 1.6c shows the typical potential *vs.* capacity profile for hard carbon when tested against sodium metal counter electrodes.[26] The different steps of the mechanism are also labeled and depicted. Tsai *et al.* further confirmed the reaction process through density functional theory (DFT) calculation showing that large initial interlayer distance is not the only factor that favours Na^+ ion intercalation into layered domains. In particular, the vacancy defects in hard carbon can greatly enhance the Na^+ ion intercalation.[27] However, Bommier *et al.* in a very recent study suggested that the storage mechanism may be a three-step process rather than the widely believed two-step storage mechanism based on the card-house model, consisting of Na-ion storage at defect sites, by intercalation and last via pore-filling.[28] Such research results show that the mechanisms of Na storage in hard carbon is still controversial. Therefore, further theoretical and experimental investigation should be conducted.

To date, numerous carbon-based materials with various morphologies, such as porous hard carbons,[29–32] carbon microspheres,[33,34] carbon nanosheets,[35,36] hollow carbon spheres,[37,38] carbon nanofibers,[39–41] carbon nanofiber films,[42,43] and graphene paper[44] have been proposed for NIBs and display promising storage performances with reversible capacity higher than 200 mAh g^{-1}. In addition, biomass derived carbons also attract much interest due to their low production cost and low energy

consumption during the synthesis procedure.[20,45–47] In particular, noted that most of the research work have adopted heteroatom (such as N, P, Sand F) doping strategy to enhance the electrochemical properties. Doping heteroatom into a carbon structure tends to enhance the electronic conductivity, to create more defect site (reaction sites) for Na^+ ions accommodation, and to improve the electrode−electrolyte interaction by functionalizing the carbon surface.[20] Even though significantly improved performance has been achieved, the first cycle irreversible capacity (or low first cycle Coulombic efficiency) and poor rate capability are still serious issues which hinder the practical applications of hard carbons. To solve these problems, systematic studies of the relationship between structure (such as specific surface area, porosity, vacancy defects and graphitization degree) and property of carbon materials and the effect of electrolytes and additives (solid electrolyte interface (SEI) layer), as well as computational works such as DFT calculation and *ab initio* calculation are of vital importance.

1.3.2.2 Ti-based compounds

Anatase TiO_2

Titanium dioxides (TiO_2) are the most common form of titanium compounds, has several polymorphs such as amorphous, anatase, rutile, brookite, and monoclinic TiO_2(B)-type have attracted significant attention as typical intercalation anode materials for LIBs owing to their properties of stable, reasonable operation voltage, nontoxic, inexpensive, and abundant materials. Recently, TiO_2 of different phases has been investigated as anode for NIBs. Among them, most research results were reported using anatase TiO_2 because the activation barrier for Na^+ insertion into the anatase lattice is comparable to that of lithium, which is rather remarkable considering its larger ionic radius.[20] Anatase TiO_2 (Figure 1.7a) features a 3D framework structure built by the stacking of 1D zigzag chains assembling of edge-sharing TiO_6 octahedra. The unique structure with empty zigzag channels enables the reversible insertion of Na^+ and provides suitable pathways for Na^+ diffusion.

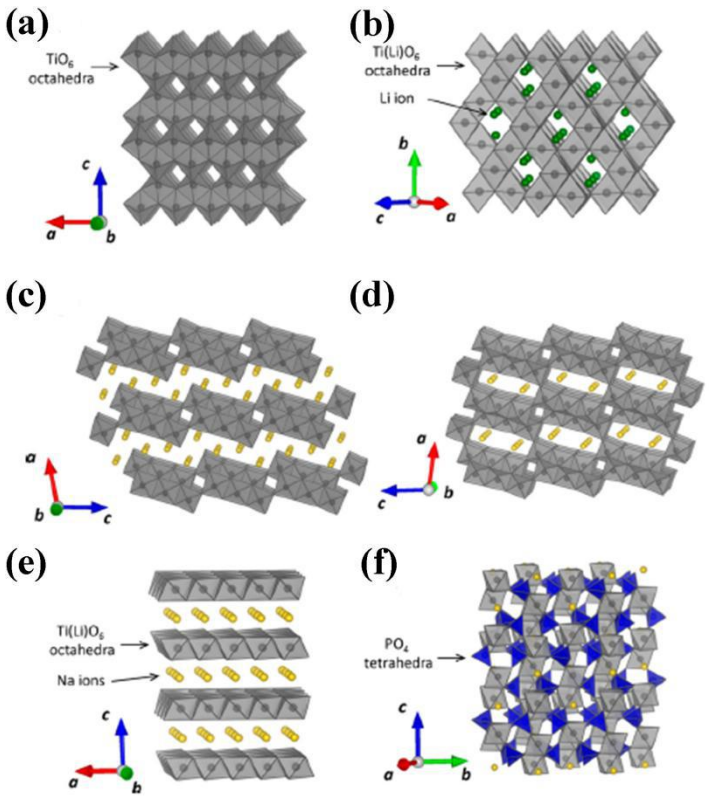

Figure 1.7 Schematic illustrations of (a) anatase-type TiO_2, (b) $Li[Li_{1/3}Ti_{5/3}]O_4$, (c) $Na_2Ti_3O_7$, (d) $Na_2Ti_6O_{13}$, (e) P2-$Na_{0.66}[Li_{0.22}Ti_{0.78}]O_2$, and (f) $NaTi_2(PO_4)_3$.[15]

Mitlin *et al.* first reported anatase TiO_2 nanocrystals composite with amorphous carbon as anodes for NIBs, which showed a stable performance of 150 mAh g^{-1} over 100 cycles at a rate of 50 mA g^{-1} and good rate capabilities.[48] About the sodium storage mechanism of anatase TiO_2, Myung *et al.*[49] first claimed an intercalation mechanism based on the $Ti^{4+/3+}$ redox reaction by using the *ex situ* X-ray diffraction (XRD) and X-ray absorption spectroscopy (XANES) analysis of cycled electrodes. They observed the reversible variation of the lattice parameter by the *ex situ* XRD analysis but no new peaks for Ti and Na_2O in the sodiated or desodiated state, indicating that no conversion reaction occurred. Similarly, Kim's, Sun's and Yang's groups[50–53] also obtained the same results based on an *ex situ* XRD or X-ray photoelectron spectroscopy (XPS) measurements. However, in Wang's study on anatase TiO_2 hollow nanospheres as NIB anode,[54] the authors also conducted *ex situ* XRD measurement but found that all anatase-related diffraction peaks disappeared after discharge to 0.01 V and did not reappear in the following charge state, which

they attributed to the reversible conversion reaction between the Na ions and TiO_2. However, other reaction mechanisms of TiO_2 for NIBs may exist, and some objective factors may influence the experimental results. First, some amorphous phases in the cycled electrodes may exist even if can not be detected by the *ex situ* XRD. Second, the formation of SEI layer on the active materials and its variation induced by electrolytes may contribute to the experimental results, which might be the reason for the groups to not find the presence of metallic Ti by XPS and XANES. Therefore, to remove the effect of the SEI layer as well as possible oxidation processes occurring during sample preparation is urgent to acquire accurate experimental results.

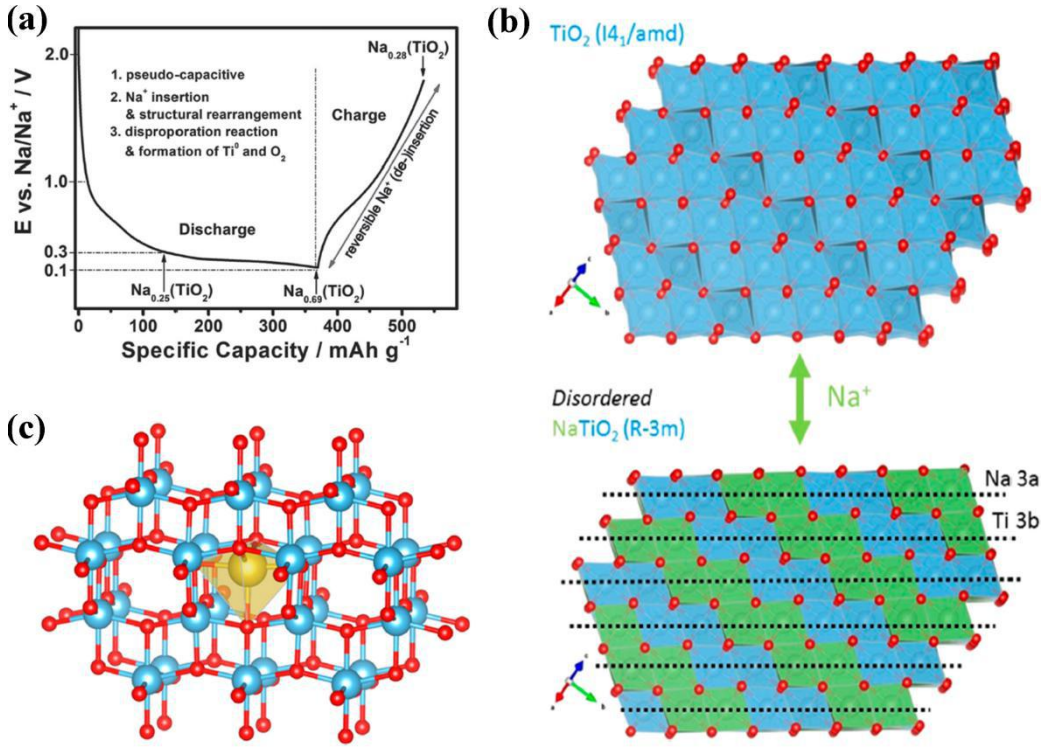

Figure 1.8 (a) Potential profile of the first (dis-)charge cycle of an anatase TiO_2-based electrode at 0.01C (cut-off potentials: 0.1 and 2.0 V) including the proposed reaction mechanism and the sodiation degree of the newly formed titanate phase at 0.3, 0.1, and 2.0 V.[55] (b) A scheme highlighting the structural relationship between the pristine tetragonal and sodiated rhombohedral phases, view is along the (100) direction.[56] (c) DFT optimized structure for Na in anatase TiO_2, showing the preferred off-center coordination.[56]

Passerini *et al.*[55] carried out a systematic study on anatase nanoparticles by means of *in situ* and *ex situ* XRD, *ex situ* XPS and Raman spectroscopy, *in situ* gas

chromatography and mass spectrometry (GC-MS), as well as electrochemical methods with the aim of unfolding the reaction mechanism of anatase as a NIB anode. The *in situ* and *ex situ* XRD measurements showed that almost all anatase-related reflections disappeared except for the most intense (101) reflection at the end of the first discharge step (sodiated state), revealing that the particles remained partially crystalline. The anatase diffraction peaks were not observed at the subsequent charge step (desodiated state), implying that new amorphous materials may form after the desodiation process. The *ex situ* XPS analysis with the assistance of argon ion etching revealed that during sodiation Ti^{4+} was reduced to Ti^{3+} and Ti^{0} and the Ti^{3+}:Ti^{4+} ratio increased upon continuous discharge to 0.1 V while decreased again on the subsequent charge. The XPS results indicated that a new reversible sodium titanate ($Na_x(TiO_2)$) was formed at the different charged and discharged states, which was able to reversibly (de-)insert sodium ions. The *in situ* GC-MS results showed that the steadily increasing oxygen (O_2) evolution was remarkable during the initial discharge, which indicated the reduction of TiO_2 to Ti and accompanied the structural rearrangement and amorphization of the active material. Based on the systematic study the authors propose a new reaction mechanism of TiO_2 (as shown in Figure 1.8a) including the initial formation of an intermediately sodium titanate phase which disproportionate into another sodium titanate phase, metallic Ti, NaO_2 and O_2. All these processes are irreversible, but the newly formed amorphous sodium titanate phase can reversibly uptake and release sodium ions. In a more recent study, Dambournet *et al.*[56] reported the reversible phase transition for sodium insertion in anatase TiO_2 based on the XRD, high resolution of high angle annular dark-field scanning transmission electron microscope (HAADF-STEM), and pair distribution function (PDF) analysis results. The authors claimed that the sodiated phase displays a layered-like rhombohedral $R\bar{3}m$ structure built from the stacking of Ti and Na slabs, which shows strong disorder due to cationic intermixing between the Ti and Na slabs with the refined chemical formula of $(Na_{0.43}Ti_{0.57})_{3a}\square_{0.22}Na_{0.39}Ti_{0.39})_{3b}O_2$, where $\square$ refers to vacancy (Figure 1.8b). Upon desodiation, the structure transforms to a

heavily disordered three-dimensional network (amorphous phase) with a similar local structure to anatase. The reversible sodium insertion/de-insertion is ensured by these two phases and due to the amorphous nature of the two phases the electrochemical process shows sloping composition-potential curves. In addition, the authors also performed DFT calculations for Na_xTiO_2 to better understand the insertion of sodium into anatase TiO_2, revealing that Na^+ ion adopts a five-coordinate off-center position in the octahedral interstitial site (Figure 1.8c). The reversible phase transition theory proposed by Dambournet *et al.* could well explain the sodium storage mechanism occurring in anatase.

As anode materials for NIBs, however, TiO_2 suffers from the low electric conductivity and the slow ion diffusion. Downsizing the active material particles to nanoscale, which has already proven successful for active materials in LIBs, is an effective approach to improve the electrochemical performance. Thus, anatase TiO_2 nanostructures with different morphologies such as hollow nanospheres,[54] nanocubes,[57] nanoplates,[58] and mesoporous microparticles[59] have been prepared. To further enhance the electrochemical performance by increasing the electronic and ionic conductivity of TiO_2 materials, carbonaceous coating/hybridizing,[49–53,60–63] element doping,[52,64–69] and introducing defects[70–72] have also been demonstrated to be effective methods in recent years. In addition, the influence of the electrolyte on the electrochemical performance of TiO_2 has also been concerned. Passerin's group[73] investigated the electrochemical performance dependence of anatase TiO_2 on various electrolyte compositions (different salts and solvents). They found that anatase TiO_2 presents the best performance in terms of specific capacity, cycling stability, and Coulombic efficiency when using an electrolyte of 1 M $NaClO_4$ in ethylene carbonate : propylene carbonate (EC:PC) binary solvents.

Lithium/sodium titanates

Spinel $Li[Li_{1/3}Ti_{5/3}]O_4$ (or $Li_4Ti_5O_{12}$, Figure 1.7b), which is well known as a high-safety and "zero-strain" anode for LIBs, has also been investigated as an anode

material in SIBs in recent years. Zhao *et al.* reported its application in sodium storage for the first time in 2012.[74] The $Li_4Ti_5O_{12}$ electrode exhibited an average storage voltage at ca. 0.9 V and a reversible capacity of 145 mAh g^{-1}. Later they further investigated the influence of binders on the electrochemical performance of $Li_4Ti_5O_{12}$ electrode which exhibited an improved performance with a reversible capacity of 155 mAh g^{-1} and excellent cyclability when using an appropriate binder of carboxymethyl-cellulose sodium (Na-CMC).[75] More importantly, the authors first interpreted the sodium insertion behavior in $Li_4Ti_5O_{12}$ via DFT calculations, *in situ* synchrotron XRD and advanced electron microscopy through a new reversible three-phase reaction of $2Li_4Ti_5O_{12} + 6Na^+ + 6e^- \rightarrow Li_7Ti_5O_{12} + Na_6LiTi_5O_{12}$, which is quite different from the well-known two-phase reaction of $Li_4Ti_5O_{12}/Li_7Ti_5O_{12}$ during lithium insertion. Like TiO_2, the intrinsically low electronic and ionic conductivity of $Li_4Ti_5O_{12}$ is a significant challenge to obtain high rate performance. Therefore nanosizing the $Li_4Ti_5O_{12}$,[76,77] elements doping[78] and carbon coating[79] have been reported to improve the performance recently.

Sodium titanates, especially $Na_2Ti_3O_7$, have been extensively studied as anodes for rechargeable NIBs in the past few years, due to its lower Na^+ insertion voltage and the open layered framework. The structure of $Na_2Ti_3O_7$ is composed of zigzag TiO_6 octahedra layers with Na-ions in the interlayer space (Figure 1.7c). Palacin *et al.* first reported $Na_2Ti_3O_7$ as an effective low-voltage insertion sodium compound which shows the ability to reversibly uptake 2 Na ions per formula unit (200 mAh g^{-1}) at an average potential of 0.3 V.[80] Wang *et al.*[81] predicted by first-principles simulations that $Na_2Ti_3O_7$ could uptake 3.5 Na ions per formula unit giving the theoretical capacity of 311 mAh g^{-1}, however no more than 2 sodium ions have been reversibly inserted. The thermodynamic and kinetic properties of the sodium storage in $Na_2Ti_3O_7$ as well as the sodium diffusion trajectories based on a vacancy-hopping mechanism were systematically investigated by Chen *et al.*[82] Though $Na_2Ti_3O_7$ is promising to be used as anode for NIBs, its practical application is still challenging owing to some serious issues. To address the insulating nature and to reduce the irreversible capacity

occurring at the initial cycle to extend cycle life, surface engineering including carbonaceous coating/hybridizing is needed and has been conducted.[83–86] Compared to $Na_2Ti_3O_7$, another type of sodium titanate $Na_2Ti_6O_{13}$ (Figure 1.7d), which has lower sodium content presenting the tunnel monoclinic structure, has also been tested in NIBs.[87–90] During discharge it displays a higher voltage plateau at approximately 0.8 V and the reversible capacity is much lower than that of layered $Na_2Ti_3O_7$.

Interestingly, a Li/Na-mixed titanate, $Na_{0.66}[Li_{0.22}Ti_{0.78}]O_2$ (Figure 1.7e), is also studied as the insertion host for Na ions.[91] The crystal structure is classified as the P2-type layered structure, where Ti and Li ions are located at the edge-shared octahedral sites forming $[Li_{0.22}Ti_{0.78}]O_2^{0.66-}$ layers while Na ions are located at six oxygen-coordinated prismatic sites between the layers. This layered titanate material allows 0.37 Na insertion into the host yielding a theoretical capacity of 116 mAh g^{-1} at an average storage voltage of 0.75 V. Specifically, it exhibits only ~ 0.77% volume change during sodium insertion/extraction. Such a nearly zero-strain character with a single phase reaction could be the remarkable advantage of $Na_{0.66}[Li_{0.22}Ti_{0.78}]O_2$ as the electrode materials with good cyclability. Indeed, an excellent long cycle life over 1200 cycles with a small capacity decay of 0.02% per cycle has been demonstrated. Though the practical capacity is relatively low (~ 100 mAh g^{-1}) the excellent cyclability and potential safety makes $Na_{0.66}[Li_{0.22}Ti_{0.78}]O_2$ a good candidate for the development of long-life sodium-ion batteries for large-scale energy storage systems

Titanium phosphate

NASICON-type $NaTi_2(PO_4)_3$, can be used as an electrode material for NIBs. In the crystal structure (Figure 1.7f), TiO_6 octahedra are isolated from each other by corner-shared PO_4 tetrahedra, forming the open structure with some vacant sites for alkali ions. Delmas *et al.*[92] first reported reversible electrochemical Na insertion into NASICON-type $NaTi_2(PO_4)_3$. Two mol of Na ions can be reversibly inserted in $NaTi_2(PO_4)_3$ based on a Ti^{3+}/Ti^{4+} redox couple, giving a theoretical capacity of 133 mAh g^{-1} with a flat operating voltage of 2.1 V in non-aqueous electrolyte. It is

considered as one excellent electrode material in large-scale application, due to the open 3D framework with the large interstitial spaces, fast Na^+ diffusion, low cost, structural stability and intrinsic safe property even at high charge states. Nevertheless, the low electronic conductivity inhibits its potential in battery applications. Developing composites of $NaTi_2(PO_4)_3$ with conductive carbonaceous materials have been recognized as one of the most effective ways to improve the rate and cycle performance.[93–96] Furthermore, the performance of $NaTi_2(PO_4)_3$ in aqueous electrolyte has also been studied.[97,98] Park *et al.*[97] compared the electrochemical performance of $NaTi_2(PO_4)_3$ in non-aqueous and aqueous electrolytes and found that it exhibited almost the same capacity at the first cycle for both cases but a smaller overpotential in aqueous electrolyte at a large current density of 2.0 mA cm^{-2}. The Na^+ insertion/extraction potential was found to be located at the lower limit of the electrochemical stability window of the aqueous Na_2SO_4 electrolyte. In addition, the cycling performance and rate capability were better in aqueous electrolyte. The reason can be ascribed to the usage of aqueous electrolyte with high conductivity and low viscosity. Via compositing with graphene Li *et al.*[98] obtained excellent cycle stability at 20 C for 2000 cycles. These results indicate that $NaTi_2(PO_4)_3$ is an attractive anode for low cost and high safety aqueous NIBs (*vs.* non-aqueous systems).

1.3.2.3 Na alloys and compounds

In the former sections, insertion-type anodes of carbon-based and Ti-based materials, which show relatively small volume expansion upon sodiation, were reviewed. In this section, alloy-type electrode materials (*e.g.*, Sn and Sb) that undergo huge volume changes during the sodiation/desodiation process are reviewed. Alloy-type materials have recently received increasing attention as anode materials, because they can alloy with sodium to form Na-metal-alloy phases, generating much higher capacities compared to the above discussed insertion-type materials. However, the extremely high volumetric expansion–contraction during the repetitive alloying–dealloying process caused by large sodium ions restricts the practical application of these

alloy-type anodes for NIBs. Because it will lead to electrode fracture or pulverization, thus the loss of electrical contact and consequent capacity decay during cycling. To date, strategies such as designing efficient nanostructures and introducing conductive carbon host/substrate (*e.g.*, carbon nanofibers, graphene) have been developed to tackle this problem. Additionally, engineering binary inter-metallic compounds and utilizing suitable binders and electrolytes (additives) also turn out to be effective approaches for enhanced sodium storage properties.

Tin (Sn)

Sn has been regarded as one of the most promising anode materials owing to its low reaction potential (< 0.6 V) and high theoretical specific capacity of 847 mAh g^{-1} based on the full sodiation state of $Na_{15}Sn_4$.[99] Huang *et al.*[100] investigated the microstructural evolution and phase transformation with volumetric expansions of tin nanoparticles during electrochemical sodiation using *in situ* TEM. According to their report, Sn undergoes a two-step sodiation process to form a Na-poor, amorphous Na_xSn (*a*-NaxSn, $x \sim 0.5$) alloy phase (56% expansion) via a two-phase reaction with a migrating phase boundary in the first step, and sequentially to form several Na-rich amorphous phases and finally the crystalline *c*-$Na_{15}Sn_4$ phase (420% expansion) via a single-phase reaction (Figure 1.9a). Actually, the electrochemical insertion process of sodium into Sn has not been fully elucidated and it has been suggested to be more complicated than that for LIBs. The structure and composition of the intermediate Na_xSn phases still need further investigation to better understand the sodium storage mechanism of Sn though till now there have been some studies on this topic by using various techniques and DFT calculations.[99–106] The large volume variation during the uptake–release process of 3.75 Na atoms in Sn is the main obstacle for full use of the tin-based anode. Because it would result in substantial pulverization of the active materials and loss of electrical contact with the current collector, leading to poor cycling capability. Therefore, most works focused on dealing with this issue.

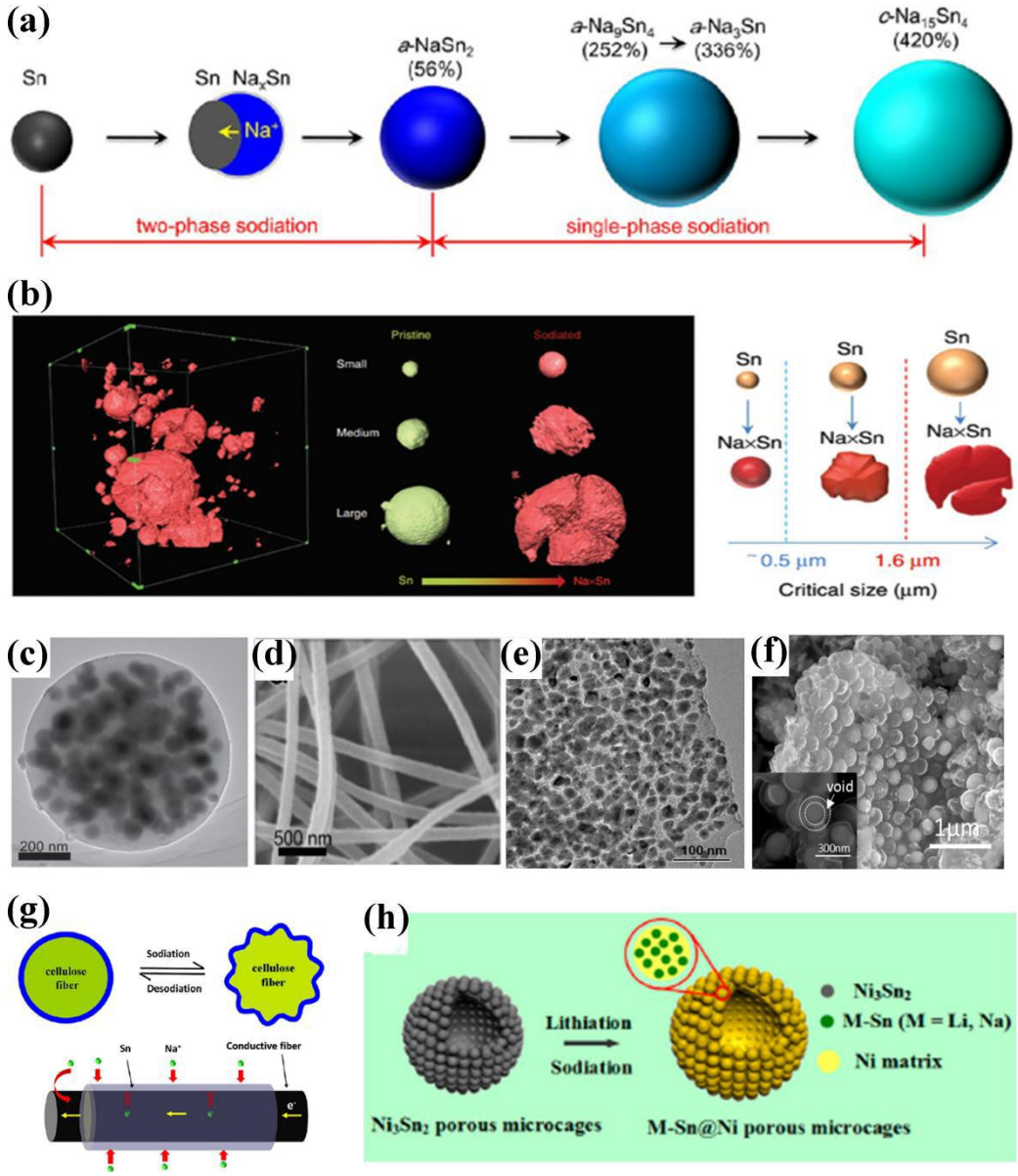

Figure 1.9 (a) Schematic illustration of the structural evolution of Sn during the sodiation.[100] (b) 3D morphologies of the sodiated electrode and selected three particles with different sizes and fracture and a schematic illustration of two critical sizes for Sn fracture in NIB.[107] (c) TEM image of Sn@C sphere.[108] (d) SEM image of Sn NDs@PNC nanofibers.[109] (e) TEM image of F-G/Sn@C composites.[110] (f) TEM image of yolk–shell Sn@C eggette-like nanostructure.[111] (g) Soft wood fiber substrates effectively release sodiation generated stresses by structural wrinkling and dual pathways for ion transport.[112] (h) Schematic representation of the first lithiation and sodiation of porous Ni_3Sn_2 intermetallic microcages, forming 0D electroactive M−Sn (M = Li, Na) particles embedded in 3D conducting Ni hollow matrix.[132]

Wang *et al.*[107] has visualized the 3D structural/chemical evolution of the Sn electrode during multi-electrochemical cycles (sodiation–desodiation) via *in situ*

synchrotron hard X-ray nanotomography (Figure 1.9b, left), which shows that small particle is robust enough to survive the big volume expansion (no cracks, fracture or pulverization) after Na ions insertion/extraction. Based on the statistical result they also suggest two important critical sizes of 0.5 μm for low complexity (negligible structural degradation) and 1.6 μm for high complexity (Figure 1.9b, right), which provide valuable information for better understanding the failure mechanisms of Sn in NIBs. Obviously, reducing the size of active materials to nanoscale is one effective strategy to endure the huge volume change during (de)sodiation. In this approach, electrodeposited Sn thin film anodes composed of fine grains exhibited a stable cycle performance with a reversible capacity of 607.51 mAh g^{-1} after 40 cycles, which is much better than that composed of coarse and isolated particles showing obvious capacity fading.[102] Furthermore, Sn nanofiber electrode synthesized by Nam *et al.*[105] exhibited a high reversible capacity of 776.3 mAh g^{-1} after 100 cycles, which corresponds to the capacity retention of 95.1%. Another effective approach is constructing Sn/C nanocomposites by introducing conductive carbon host/substrate, which can physically buffer the volume strain, prevent the nanoparticles from migrating and agglomerating, and create the electric conducting pathways. To this end, various nanostructured Sn/C composites[108–112] with different morphologies (Figure 1.9c−g) have been fabricated and exhibited excellent cycling stability with high capacity above 400 mAh g^{-1} and superior rate capabilities. In addition, it has been demonstrated that binders in the electrode and electrolyte additives also play critical roles in battery performance.[113,114] For instance, Komaba *et al.*[113] found that the reversibility of the Sn powder electrodes was effectively improved by adopting polyacrylate (PAA) as a binder instead of the mainstream binder of polyvinylidene fluoride (PVDF), though the Sn−PAA electrode still showed insufficient capacity retention due to the inevitable volume change of the electrode material and electrolyte decomposition at the active surface of Na−Sn alloys. They also found that when a small amount of fluoroethylene carbonate (FEC) was added to the propylene carbonate-based electrolyte, the performance of the Sn electrode with PAA binder was further improved.

Antimony (Sb)

Antimony could deliver a theoretical capacity of 660 mAh g^{-1} according to formation of Na_3Sb (fully sodiation state).[99] It has also been emerging as one of the popular alloy-type anode materials for NIBs. However, Sb also meets the challenge of huge volume change (~ 390%) during the Na alloying/dealloying process, which could cause capacity fading. Similar to the investigation of Sn/C nanocomposite anodes, the investigation of Sb also focuses on constructing Sb/C nanocomposites.[115–124] For example, a novel Sb@C nanosphere anode with biomimetic yolk−shell structure has been prepared via a nanoconfined galvanic replacement route.[122] The hollow Sb@C yolk−shell particles displayed a reversible capacity of approximate 280 mAh g^{-1} at 1000 mA g^{-1} after 200 cycles. The excellent performance can be ascribed to the novel hollow Sb@C yolk−shell structures which allows for the full volume expansion of inner Sb while maintaining the framework of the Sb@C anode and developing a stable SEI film on the outside carbon shell.

Binary inter-metallic compounds

In addition to the investigation of single element alloy based materials, some binary inter-metallic compounds also have drawn attention and many nanostructured materials have been designed. Binary alloy of SnSb[125,126] and its composites with carbon[127–131] have been designed for NIB anodes. The formed SnSb alloy usually exhibits better electrochemical performance than that of single one because the two different metal phases can work as mutual buffers for each other to alleviate the volume fluctuations. Besides, other binary inter-metallic compounds of Sn−M and Sb−M, in which secondary mental M is an electrochemically inactive metal element (*e.g.*, Cu, Ni, Mo, and Fe), such as Ni_3Sn_2,[132] NiSb,[133] $Sn_{0.9}Cu_{0.1}$,[134] $FeSn_2$,[135] Cu_6Sn_5,[136] Mo_3Sb_7,[137] and Cu_2Sb,[138] provide candidates as substitutes for the pure elemental electrodes, since the lower volume changes and the presence of the inactive element can provide a more stable structure and more efficient electronic conduction within the expanding/shrinking framework. For instance, Yu *et al.*[132] reported highly porous Ni_3Sn_2 microcages composed of tiny nanoparticles as anode materials for

high-capacity and high-rate-capability LIBs and NIBs (Figure 1.9h). The porous Ni_3Sn_2 microcages were synthesized by a facile template-free solvothermal method based on Ostwald ripening and etching mechanism. For Na-ions storage performance, a reversible capacity of approximate 270 mAh g^{-1} was stably maintained at 1C for 300 cycles and excellent rate capabilities up to 10 C was also obtained. The reason for the excellent performance is owing to the following aspects: i) mechanical strain of the Sn during charge/discharge processes is effectively suppressed by the hollow cores structure and the presence of the Ni matrix in the hollow microcages; ii) the homogeneously encapsulated Ni converted from lithiation or sodiation of Ni_3Sn_2 is certainly beneficial for the necessary electron transport. Mullins *et al.*[134] prepared $Sn_{0.9}Cu_{0.1}$ nanoparticles (~ 100 nm) via a surfactant-assisted wet chemistry route carried out at room temperature. The electrodes made with the $Sn_{0.9}Cu_{0.1}$ nanoparticles exhibited a stable capacity of greater than 420 mAh g^{-1} at 0.2 C rate, retaining 97% of their capacity after 100 cycles, much better than that of the Sn microparticles and Sn nanoparticles which respectively retained only 13 and 49% of their capacities after 100 cycles. The good performance is attributed to the addition of copper in the tin which could effectively reduce the interfacial charge transfer resistance and suppress aggregation among the nanoparticles.

1.3.2.4 Other materials

Besides, many other anodes have also appeared, such as metal oxides (except TiO_2) and metal sulfides based on a conversion reaction mechanism or a conversion-dealloying mechanism, insertion-type organic anode materials (for example, $Na_2C_8H_4O_4$) and carboxylate-based materials.[9,14,20,139,140] However, the electronic conductivity and cyclability still remain the significant challenge.

1.4 The basic requirements for sodium-ion battery electrode materials

The ideal electrode materials of NIBs generally need to meet the following basic requirements:

(1) High electrochemical activity and specific capacity for reversible Na ions.

(2) To ensure a high voltage output of the cell, the cathode materials should have high potential versus sodium while the anode materials should have close potential with sodium.

(3) Good structural stability and electrochemical stability during Na ions insertion /de-insertion, so that good reversibility and cycling performance can be expected.

(4) High ionic conductivity (Na ions diffusion coefficient) and electronic conductivity, thus the electrode materials could exhibit lower polarization and ensure the good capability of fast charge/discharge under high current densities.

(5) Good compatibility with the electrolytes, and high chemical and thermal stability after the formation of SEI layer.

(6) Simple and efficient synthetic strategy, which is suitable for large-scale commercial applications.

(7) The resources used for making cathode and anode should be abundant, low cost and environmentally friendly.

1.5 General strategies for performance enhancement

To enable the application of the above mentioned promising cathode and anode materials of NIBs in Section 1.3, various strategies have been used. These strategies for performance enhancement are summarized from six aspects as shown in Figure 1.10, and are often similar regardless of type of material, crystal structure, or operating mechanism.[141] Essentially, all these strategies are talking about the same topic of surface and interface engineering, which has been proven effective in improving the electrochemical performance of electrode materials and has received

more and more attention recently.

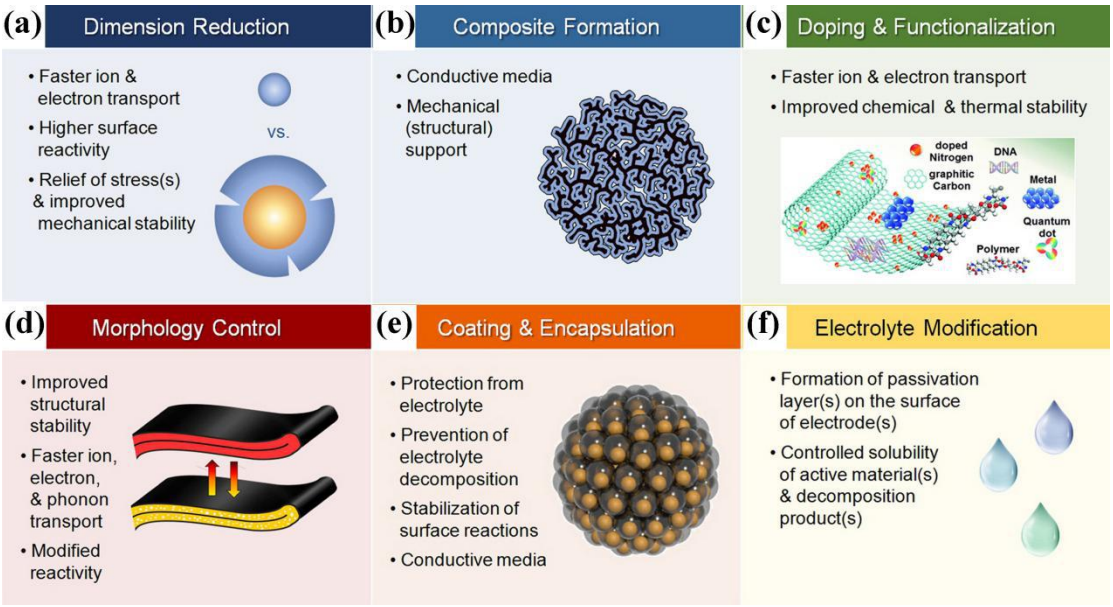

Figure 1.10 General strategies for performance enhancement and their rationale: (a) reducing dimensions of active materials, (b) formation of composites, (c) doping and functionalization, (d) tuning particle morphology, (e) formation of coatings or shells around active materials, (f) modification of electrolyte. Note: these general strategies are summarized for LIBs materials by Nitta, et al.,[141] but can also be applied to NIBs materials because of their similar electrochemistry.

1.6 Aims of thesis

The past decade has witnessed plenty of breakthroughs in the study of electrode materials of NIBs. A variety of layered sodium metal oxides have been proven to be suitable cathode materials and can be commercialized for practical uses. One of the major challenges in NIB research is the search for suitable anode materials with long lifetimes and high specific capacities. This thesis presents fundamental studies of various anode materials for NIBs from different aspects.

Chapter 3 and Chapter 4 are concerned with surface modification of anatase TiO_2 nanoparticles with the aim of improving the sodium storage performance by using a simple but effective approach. Especially, in Chapter 2 the influence of different electrolytes on the performance of TiO_2 is also investigated.

Chapter 5 investigates the Na-ion diffusivity and mechanical instability in Sn anodes in the form of thick film, to better understand the seldomly studied degradation mechanisms that occur in Sn anode during sodiation-desodiation.

Chapter 6 explores facile synthesis of carbon materials from low cost carbon source of CaC_2 using a novel sulfur-based thermo-chemical etching technique. The application of the as-prepared carbon materials as anode for NIBs and LIBs is also preliminarily studied.

1.7 References

1. J. Deng, W. Luo, S. Chou, H. Liu, S. Dou, *Adv. Energy Mater.* 8 (2018) 1701428.
2. M.S. Whittingham, *Science* 192 (1976) 1126–1127.
3. G.H. Newman, L.P. Klemann, *J. Electrochem. Soc.* 127 (1980) 2097–2099.
4. K. Mizushima, P.C. Jones, P.J. Wiseman, J.B. Goodenough, *Mater. Res. Bull.* 15 (1980) 783–789.
5. C. Delmas, J.-J. Braconnier, C. Fouassier, P. Hagenmuller, *Solid State Ionics* 3-4 (1981) 165–169.
6. N. Yabuuchi, K. Kubota, M. Dahbi, S. Komaba, *Chem. Rev.* 114 (2014) 11636–11682.
7. D.A. Stevens, J.R. Dahn, *J. Electrochem. Soc.* 147 (2000) 1271–1273.
8. S. Okada, Y. Takahashi, T. Kiyabu, T. Doi, J.-I. Yamaki, T. Nishida, *210th ECS Meet. Abstr.* 2006, MA2006-02, 201.
9. H. Pan, Y. Hu, L. Chen, *Energy Environ. Sci.* 6 (2013) 2338–2360.
10. L. Chen, M. Fiore, J.E. Wang, R. Ruffo, D.-K. Kim, G. Longoni, *Adv. Sustainable Syst.* 2 (2018) 1700153.
11. Z.G. Yang, J.L. Zhang, M.C.W. Kintner-Meyer, X.C. Lu, D.W. Choi, J.P. Lemmon, J. Liu, *Chem. Rev.* 111 (2011) 3577–3613.
12. C. Vaalma, D. Buchholz, M. Weil, S. Passerini, *Nat. Rev. Mater.* 3 (2018) 18013.
13. J.L. Murray, *Bull. Alloy Phase Diagrams* 4 (1983) 407–410.
14. Y. Kim, K.-H. Ha, S.M. Oh, K.T. Lee, *Chem. Eur. J.* 20 (2014) 11980–11992.
15. H. Kim, J. Hong, K.-Y. Park, H. Kim, S.-W. Kim, K. Kang, *Chem. Rev.* 114 (2014) 11788–11827.
16. W. Ren, Z. Zhu, Q. An, L. Mai, *Small* 13 (2017) 1604181.
17. M.F. Oszajca, M.I. Bodnarchuk, M.V. Kovalenko, *Chem. Mater.* 26 (2014) 5422–5432.

18. C. Fang, Y. Huang, W. Zhang, J. Han, Z. Deng, Y. Cao, H. Yang, *Adv. Energy Mater.* 6 (2016) 1501727.
19. X. Xiang, K. Zhang, J. Chen, *Adv. Mater.* 27 (2015) 5343–5364.
20. J.-Y. Hwang, S.-T. Myung, Y.-K. Sun, *Chem. Soc. Rev.* 46 (2017) 3529–3614.
21. M.H. Han, E. Gonzalo, G. Singh, T. Rojo, *Energy Environ. Sci.* 8 (2015) 81–102.
22. B. Jache, P. Adelhelm, *Angew. Chem. Int. Ed.* 53 (2014) 10169–10173.
23. H. Kim, J. Hong, Y.-U. Park, J. Kim, I. Hwang, K. Kang, *Adv. Funct. Mater.* 25 (2015) 534–541.
24. Y. Wen, K. He, Y. Zhu, F. Han, Y. Xu, I. Matsuda, Y. Ishii, J. Cumings, C. Wang, *Nat. Commun.* 5 (2014) 4033.
25. D.A. Stevens, J.R. Dahn, *J. Electrochem. Soc.* 148 (2001) A803–A811.
26. E. Irisarri, A. Ponrouch, M.R. Palacin, *J. Electrochem. Soc.* 162 (2015) A2476–A2482.
27. P.-C. Tsai, S.-C. Chung, S.-K. Lin, A. Yamada, *J. Mater. Chem. A* 3 (2015) 9763–9768.
28. C. Bommier, T.W. Surta, M. Dolgos, X. Ji, *Nano Lett.* 15 (2015) 5888–5892.
29. K. Zhou, M. Hu, Y. He, L. Yang, C. Han, R. Lv, F. Kang, B. Li, *Carbon* 129 (2018) 667–673.
30. N. Wang, Y. Wang, X. Xu, T. Liao, Y. Du, Z. Bai, S. Dou, *ACS Appl. Mater. Interfaces* 10 (2018) 9353–9361.
31. Y. Zhu, M. Chen, Q. Li, C. Yuan, C. Wang, *Carbon* 129 (2018) 695–701.
32. H. Hou, C.E. Banks, M. Jing, Y. Zhang, X. Ji, *Adv. Mater.* 27 (2015) 7861–7866.
33. D. Xu, C. Chen, J. Xie, B. Zhang, L. Miao, J. Cai, Y. Huang, L. Zhang, *Adv. Energy Mater.* 6 (2016) 1501929.
34. W. Xiong, Z. Wang, J. Zhang, C. Shang, M. Yang, L. He, Z. Lu, *Energy Storage Mater.* 7 (2017) 229–235.
35. Y. Qiao, M. Ma, Y. Liu, S. Li, Z. Lu, H. Yue, H. Dong, Z. Cao, Y. Yin, S. Yang, *J. Mater. Chem. A* 4 (2016) 15565–15574.
36. T. Yang, T. Qian, M. Wang, X. Shen, N. Xu, Z. Sun, C. Yan, *Adv. Mater.* 28 (2016) 539–545.
37. K. Huo, W. An, J. Fu, B. Gao, L. Wang, X. Peng, G.J. Cheng, P.K. Chu, *J. Power Sources* 324 (2016) 233–238.
38. K. Tang, L. Fu, R.J. White, L. Yu, M.M. Titirici, M. Antonietti, J. Maier, *Adv. Energy Mater.* 2 (2012) 873–877.
39. Y. Cao, L. Xiao, M.L. Sushko, W. Wang, B. Schwenzer, J. Xiao, Z. Nie, L.V. Saraf, Z. Yang, J. Liu, *Nano Lett.* 12 (2012) 3783–3787.
40. H.J. Yoon, M.E. Lee, N.R. Kim, S.J. Yang, H.-J. Jin, Y.S. Yun, *Electrochim. Acta* 242 (2017) 38–46.

41. R. Hao, Y. Yang, H. Wang, B. Jia, G. Ma, D. Yu, L. Guo, S. Yang, *Nano Energy* 45 (2018) 220–228.
42. H. Zhu, C. Wang, C. Li, L.Guan, H. Pan, M. Yan, Y. Jiang, *Carbon* 130 (2018) 145–152.
43. M. Wang, Y. Yang, Z. Yang, L. Gu, Q. Chen, Y. Yu, *Adv. Sci.* 4 (2017) 1600468.
44. H. An, Y. Li, Y. Gao, C. Cao, J. Han, Y. Feng, W. Feng, *Carbon* 116 (2017) 338–346.
45. J. Deng, M. Li, Y. Wang, *Green Chem.* 18 (2016) 4824–4854.
46. R.R. Gaddam, D. Yang, R. Narayan, K.V.S.N. Raju, N.A. Kumar, X.S. Zhao, *Nano Energy* 26 (2016) 346–352.
47. H. Wang, W. Yu, J. Shi, N. Mao, S. Chen, W. Liu, *Electrochim. Acta* 188 (2016) 103–110.
48. Y. Xu, E.M. Lotfabad, H. Wang, B. Farbod, Z. Xu, A. Kohandehghan, D. Mitlin, *Chem. Commun.* 49 (2013) 8973–8975.
49. K.T. Kim, G. Ali, K.Y. Chung, C.S. Yoon, H. Yashiro, Y.-K. Sun, J. Lu, K. Amine, S.T. Myung, *Nano Lett.* 14 (2014) 416–422.
50. Y. Yeo, J.-W. Jung, K. Park, I.-D. Kim, *Sci. Rep.* 5 (2015) 13862.
51. S.-M. Oh, J.-Y. Hwang, C.S. Yoon, J. Lu, K. Amine, I. Belharouak, Y.-K. Sun, *ACS Appl. Mater. Interfaces* 6 (2014) 11295–11301.
52. J.-Y. Hwang, S.T. Myung, J.-H. Lee, A. Abouimrane, I. Belharouak, Y.-K. Sun, *Nano Energy* 16 (2015) 218–226.
53. Y. Xiong, J. Qian, Y. Cao, X. Ai, H. Yang, *ACS Appl. Mater. Interfaces* 8 (2016) 16684–16689.
54. D. Su, S. Dou, G. Wang, *Chem. Mater.* 27 (2015) 6022–6029.
55. L.M. Wu, D. Bresser, D. Buchholz, G. Giffin, C.R. Castro, A. Ochel, S. Passerini, *Adv. Energy Mater.* 5 (2015) 1401142.
56. W. Li, M. Fukunishi, B.J. Morgan, O.J. Borkiewicz, K.W. Chapman, V. Pralong, A. Maignan, O.I. Lebedev, J. Ma, H. Groult, S. Komaba, D. Dambournet, *Chem. Mater*. 29 (2017) 1836–1844.
57. X. Yang, C. Wang, Y. Yang, Y. Zhang, X. Jia, J. Chen, X. Ji, *J. Mater. Chem. A* 3 (2015) 8800–8807.
58. H. Yang, J.-G. Duh, *RSC Adv.* 6 (2016) 37160–37166.
59. L. Ling, Y. Bai, H. Wang, Q. Ni, J. Zhang, F. Wu, C. Wu, *Nano Res.* 11 (2018) 1563–1574.
60. Y. Wen, J.-H. Yun, B. Luo, M. Lyu, L. Wang, *Electrochim. Acta* 219 (2016) 163–169.
61. N. Wang, Y. Gao, Y. Wang, K. Liu, W. Lai, Y. Hu, Y. Zhao, S. Chou, L. Jiang, *Adv. Sci.* 3 (2016) 1600013.
62. M.N. Tahir, B. Oschmann, D. Buchholz, X. Dou, I. Lieberwirth, M. Panthofer, W.

Tremel, R. Zentel, S. Passerini, *Adv. Energy Mater.* 6 (2016) 1501489.

63. S. Qiu, L. Xiao, X. Ai, H. Yang, Y. Cao, *ACS Appl. Mater. Interfaces* 9 (2017) 345–353.
64. J. Ni, S. Fu, C. Wu, J. Maier, Y. Yu, L. Li, *Adv. Mater.* 28 (2016) 2259–2265.
65. Y. Yang, X. Ji, M. Jing, H. Hou, Y. Zhu, L. Fang, X. Yang, Q. Chen, C.E. Banks, *J. Mater. Chem. A* 3 (2015) 5648–5655.
66. B. Wang, F. Zhao, G. Du, S. Porter, Y. Liu, P. Zhang, Z. Cheng, H.K. Liu, Z. Huang, *ACS Appl. Mater. Interfaces* 8 (2016) 16009–16015.
67. D. Yan, C. Yu, Y. Bai, W. Zhang, T. Chen, B. Hu, Z. Sun, L. Pan, *Chem. Commun.* 51 (2015) 8261–8264.
68. H. Liao, L. Xie, Y. Zhang, X. Qiu, S. Li, Z. Huang, H. Hou, X. Ji, *Electrochim. Acta* 219 (2016) 227–234.
69. F. Zhao, B. Wang, Y. Tang, H. Ge, Z. Huang, H.K. Liu, *J. Mater. Chem. A* 2015, 3, 22969–22974.
70. J. Chen, Z. Ding, C. Wang, H. Hou, Y. Zhang, C. Wang, G. Zou, X. Ji, *ACS Appl. Mater. Interfaces* 8 (2016) 9142–9151.
71. H. He, Q. Zhang, H. Wang, H. Zhang, J. Li, Z. Peng, Y. Tang, M. Shao, *J. Power Sources* 354 (2017) 179–188.
72. Q. Gan, H. He, K. Zhao, Z. He, S. Liu, S. Yang, *ACS Appl. Mater. Interfaces* 10 (2018) 7031–7042.
73. L.M. Wu, D. Buchholz, D. Bresser, L.G. Chagas, S. Passerini, J. Power Sources 251 (2014) 379–385.
74. L. Zhao, H. Pan, Y.-S. Hu, H. Li, L.Q. Chen, *Chin. Phys. B* 21 (2012) 028201.
75. Y. Sun, L. Zhao, H. Pan, X. Lu, L. Gu, Y.-S. Hu, H. Li, M. Armand, Y. Ikuhara, L. Chen, X. Huang, *Nat. Commun.* 4 (2013) 1870.
76. X. Yu, H. Pan, W. Wan, C. Ma, J. Bai, Q. Meng, S.N. Ehrlich, Y.-S. Hu, X. Yang, *Nano Lett.* 13 (2013) 4721–4727.
77. P. Yu, C. Li, X. Guo, *J. Phys. Chem. C* 118 (2014) 10616–10624.
78. Y. Ge, H. Jiang, K. Fu, C. Zhang, J. Zhu, C. Chen, Y. Lu, Y. Qiu, X. Zhang, *J. Power Sources* 272 (2014) 860–865.
79. C. Chen, H. Xu, T. Zhou, Z. Guo, L. Chen, M. Yan, L. Mai, P. Hu, S. Cheng, Y. Huang, J. Xie, *Adv. Energy Mater.* 6 (2016) 1600322.
80. P. Senguttuvan, G. Rousse, V. Seznec, J.M. Tarascon, M.R. Palacin, *Chem. Mater.* 23 (2011) 4109–4111.
81. W. Wang, C. Yu, Z. Lin, J. Hou, H. Zhu, S. Jiao, *Nanoscale* 5 (2013) 594–599.
82. H. Pan, X. Lu, X. Yu, Y.-S. Hu, H. Li, X. Yang, L.Q. Chen, *Adv. Energy Mater.* 3 (2013) 1186–1194.
83. Z. Zhou, H. Xiao, F. Zhang, X. Zhang, Y. Tang, *Electrochim. Acta* 211 (2016) 430–436.

84. J. Ni, S. Fu, C. Wu, Y. Zhao, J. Maier, Y. Yu, L. Li, *Adv. Energy Mater.* 6 (2016) 1502568.

85. Z. Yan, L. Liu, H. Shu, X. Yang, H. Wang, J. Tan, Q. Zhou, Z. Huang, X. Wang, *J. Power Sources* 274 (2015) 8–14.

86. C. Ding, T. Nohira, R. Hagiwara, *J. Power Sources* 354 (2017) 10–15.

87. A. Rudola, K. Saravanan, S. Devaraj, H. Gong, P. Balaya, *Chem. Commun.* 49 (2013) 7451–7453.

88. Q. Zhang, T. Zhang, Y. Wei, T. Zhai, H. Li, *J. Mater. Chem. A* 5 (2017) 18691–18697.

89. K. Cao, L. Jiao, W. Pang, H. Liu, T. Zhou, Z. Guo, Y. Wang, H. Yuan, *Small* 12 (2016) 2991–2997.

90. Y. Zhang, H. Hou, X. Yang, J. Chen, M. Jing, Z. Wu, X. Jia, X. Ji, *J. Power Source*s 305 (2016) 200–208.

91. Y. Wang, X. Xu, S. Xu, J. Bai, R. Xiao, Y.-S. Hu, H. Li, X. Yang, L. Chen, X. Huang, *Nat. Commun.* 4 (2013) 2365.

92. C. Delmas, F. Cherkaoui, A. Nadiri, P. Hagenmuller, *Mater. Res. Bull*. 22 (1987) 631–639.

93. Y. Jiang, J. Shi, M. Wang, L. Zeng, L. Gu, Y. Yu, *ACS Appl. Mater. Interfaces* 8 (2016) 689–695.

94. J. Song, S. Park, J. Gim, V. Mathew, S. Kim, J. Jo, S. Kim, J. Kim, *J. Mater. Chem. A* 4 (2016) 7815–7822.

95. C. Xu, Y. Xu, C. Tang, Q. Wei, J. Meng, L. Huang, L. Zhou, G. Zhang, L. He, L. Mai, *Nano Energy* 28 (2016) 224–231.

96. C. Wu, P. Kopold, Y.-L. Ding, P.A. van Aken, J. Maier, Y. Yu, *ACS Nano* 9 (2015) 6610–6618.

97. S.I. Park, I. Gocheva, S. Okada, J.-I. Yamaki, *J. Electrochem. Soc.* 158 (2011) A1067–A1070.

98. X. Li, X. Zhu, J. Liang, Z. Hou, Y. Wang, N. Lin, Y. Zhu, Y. Qian, *J. Electrochem. Soc.* 161 (2014) A1181–A1187.

99. V.L. Chevrier, G. Ceder, *J. Electrochem. Soc.* 158 (2011) A1011–A1014.

100. J.W. Wang, X.H. Liu, S.X. Mao, J.Y. Huang, *Nano Lett.* 12 (2012) 5897–5902.

101. L.D. Ellis, T.D. Hatchard, M.N. Obrovac, *J. Electrochem. Soc.* 159 (2012) A1801–A1805.

102. D.H. Nam, K.S. Hong, S.J. Lim, T.H. Kim, H.S. Kwon, *J. Phys. Chem. C* 118 (2014) 20086–20093.

103. L. Baggetto, C.A. Bridges, J.-C. Jumas, D.R. Mullins, K.J. Carroll, R.A. Meisner, E.J. Crumlin, X. Liu, W. Yang, G.M. Veith, *J. Mater. Chem. A* 2 (2014) 18959–18973.

104. L. Baggetto, P. Ganesh, R.P. Meisner, R.R. Unocic, J.-C. Jumas, C.A. Bridges,

G.M. Veith, *J. Power Sources* 234 (2013) 48–59.

105. D.-H. Nam, T.-H. Kim, K.-S. Hong, H.-S. Kwon, *ACS Nano* 8 (2014) 11824–11835.

106. J.M. Stratford, M. Mayo, P.K. Allan, O. Pecher, O.J. Borkiewicz, K.M. Wiaderek, K.W. Chapman, C.J. Pickard, A.J. Morris, C.P. Grey, *J. Am. Chem. Soc.* 139 (2017) 7273–7286.

107. J. Wang, C. Eng, Y. K. Chen-Wiegart, J. Wang, *Nat. Commun.* 6 (2015) 7496.

108. Y. Liu, N. Zhang, L. Jiao, Z. Tao, J. Chen, *Adv. Funct. Mater.* 25 (2015) 214–220.

109. Y. Liu, N. Zhang, L. Jiao, J. Chen, *Adv. Mater.* 27 (2015) 6702–6707.

110. B. Luo, T. Qiu, D. Ye, L. Wang, L. Zhi, *Nano Energy* 22 (2016) 232–240.

111. S. Li, Z. Wang, J. Liu, L. Yang, Y. Guo, L. Cheng, M. Lei, W. Wang, *ACS Appl. Mater. Interfaces* 8 (2016) 19438–19445.

112. H. Zhu, Z. Jia, Y. Chen, N. Weadock, J. Wan, O. Vaaland, X. Han, T. Li, L. Hu, *Nano Lett.* 13 (2013) 3093–3100.

113. S. Komaba, Y. Matsuura, T. Ishikawa, N. Yabuuchi, W. Murata, S. Kuze, *Electrochem. Commun.* 21 (2012) 65–68.

114. K. Dai, H. Zhao, Z. Wang, X. Song, V. Battaglia, G. Liu, *J. Power Sources* 263 (2014) 276–279.

115. J. Qian, Y. Chen, L. Wu, Y. Cao, X. Ai, H. Yang, *Chem. Commun.* 48 (2012) 7070–7072.

116. L. Wu, X. Hu, J. Qian, F. Pei, F. Wu, R. Mao, X. Ai, H. Yang, Y. Cao, *Energy Environ. Sci.* 7 (2014) 323–328.

117. W. Luo, P. Zhang, X. Wang, Q. Li, Y. Dong, J. Hua, L. Zhou, L. Mai, *J. Power Sources* 304 (2016) 340–345.

118. J. Duan, W. Zhang, C. Wu, Q. Fan, W. Zhang, X. Hu, Y. Huang, *Nano Energy* 16 (2015) 479–487.

119. G. Wang, X. Xiong, Z. Lin, C. Yang, Z. Lin, M. Liu, *Electrochim. Acta* 242 (2017) 159–164.

120. F. Wan, J. Guo, X. Zhang, J. Zhang, H. Sun, Q. Yan, D. Han, L. Niu, X. Wu, *ACS Appl. Mater. Interfaces* 8 (2016) 7790–7799.

121. H. Hou, M. Jing, Y. Yang, Y. Zhang, W. Song, X. Yang, J. Chen, Q. Chen, X. Ji, *J. Power Sources* 284 (2015) 227–235.

122. J. Liu, L. Yu, C. Wu, Y. Wen, K. Yin, F.-K. Chiang, R. Hu, J. Liu, L. Sun, L. Gu, J. Maier, Y. Yu, M. Zhu, *Nano Lett.* 17 (2017) 2034–2042.

123. L. Hu, X. Zhu, Y. Du, Y. Li, X. Zhou, J. Bao, *Chem. Mater.* 27 (2015) 8138–8145.

124. X. Liu, Y. Du, X. Xu, X. Zhou, Z. Dai, J. Bao, *J. Phys. Chem. C* 120 (2016) 3214–3220.

125. A. Darwiche, M.T. Sougrati, B. Fraisse, L. Stievano, L. Monconduit, *Electrochem. Commun.* 32 (2013) 18–21.

126. M. He, M. Walter, K.V. Kravchyk, R. Erni, R. Widmer, M.V. Kovalenko, *Nanoscale* 7 (2015) 455–459.

127. L. Li, K.H. Seng, D. Li, Y. Xia, H.K. Liu, Z. Guo, *Nano Res.* 7 (2014) 1466–1476.

128. H. Jia, M. Dirican, C. Chen, J. Zhu, P. Zhu, C. Yan, Y. Li, X. Dong, J. Guo, X. Zhang, *ACS Appl. Mater. Interfaces* 10 (2018) 9696–9703.

129. L. Ji, M. Gu, Y. Shao, X. Li, M.H. Engelhard, B.W. Arey, W. Wang, Z. Nie, J. Xiao, C. Wang, J. Zhang, J. Liu, *Adv. Mater*. 26 (2014) 2901–2908.

130. Z. Yi, Q. Han, D. Geng, Y. Wu, Y. Cheng, L. Wang, *J. Power Sources* 342 (2017) 861–871.

131. I.T. Kim, S.-O. Kim, A. Manthiram, *J. Power Source*s 269 (2014) 848–854.

132. J. Liu, Y. Wen, P.A. van Aken, J. Maier, Y. Yu, *Nano Lett.* 14 (2014) 6387–6392.

133. J. Liu, Z. Yang, J. Wang, L. Gu, J. Maier, Y. Yu, *Nano Energy* 16 (2015) 389–398.

134. Y.-M. Lin, P.R. Abel, A. Gupta, J.B. Goodenough, A. Heller, C.B. Mullins, *ACS Appl. Mater. Interfaces* 5 (2013) 8273–8277.

135. E. Edison, R. Satish, W.C. Ling, N. Bucher, V. Aravindan, S. Madhavi, *J. Power Sources* 343 (2017) 296–302.

136. I.T. Kim, E. Allcorn, A. Manthiram, *J. Power Sources* 281 (2015) 11–17.

137. L. Baggetto, E. Allcorn, R.R. Unocic, A. Manthiram, G.M. Veith, *J. Mater. Chem. A* 1 (2013) 11163–11169.

138. L. Wang, C. Wang, N. Zhang, F. Li, F. Cheng, J. Chen, *ACS Energy Lett*. 2 (2017) 256–262.

139. L. Li, Y. Zheng, S. Zhang, J. Yang, Z. Shao, Z. Guo, *Energy Environ. Sci.* 11 (2018) 2310–2340.

140. Y. Xiao, S.H. Lee, Y.-K. Sun, *Adv. Energy Mater.* 7 (2017) 1601329.

141. N. Nitta, F. Wu, J.T. Lee, G. Yushin, *Mater. Today* 18 (2015) 252–264.

Chapter 2 Experimental

2.1 Chemicals and experimental instruments

2.1.1 Chemicals

All chemicals were used as received. A detailed list of chemicals used in this thesis is shown in Table 2.1.

Table 2.1 List of chemicals required in experiment process.

Chemical	Formula	Purity & Supplier
Tetrabutyl titanate	$C_{16}H_{36}O_4Ti$	97%, Sigma-Aldrich
Aluminum nitrate nonahydrate	$Al(NO_3)_3{\cdot}9H_2O$	98%, Sigma-Aldrich
Ammonium fluoride	NH_4F	99.99%, Sigma-Aldrich
Molybdenum(V) chloride	$MoCl_5$	99.99%, Sigma-Aldrich
Tin (foil)	Sn	99.998%, Sigma-Aldrich
Sulfur	S	99%, ---
Calcium carbide	CaC_2	97%, ---
Sodium perchlorate	$NaClO_4$	98−102%, Alfa Aesar
Carbon black	C	≥ 99%, Alfa Aesar
Ethanol	C_2H_5OH	99.8%, Sigma-Aldrich
Ammonia solution	NH_4OH	25%, Merck KGaA
Hydrochloric acid	HCl	30%, Merck KGaA
N-methylpyrrolidone (NMP)	C_5H_9NO	Sigma-Aldrich
Polyvinylidene fluoride (PVDF)	$(C_2H_2F_2)_x$-	Average M_w ~ 534,000 Sigma-Aldrich
Sodium metal	Na	≥ 99.8%, Sigma-Aldrich
Propylene carbonate (PC)	$C_4H_6O_3$	99.7%, Sigma-Aldrich
Ethylene carbonate (EC)	$C_3H_4O_3$	99%, Sigma-Aldrich
Fluoroethylene carbonate (FEC)	$C_3H_3FO_3$	99%, Sigma-Aldrich

2.1.2 Experimental instruments

The list of main instruments used in experiments is shown in Table 2.2.

Table 2.2 List of main instruments used in experiments.

Instrument	Model	Supplier
Analytical balance	Cubis, MSA324S	Sartorius
Heating magnetic stirrer	AREC.X	VELP Scientifica
Ultrasonic bath	USC600THD	VWR
Muffle furnace	LHT 01/17 D	Nabertherm
Stainless steel autoclave	30 mL capacity	---
Disc cutter	MSK-T-07	MTI Corp
Electric Crimper	MSK-160E	MTI Corp
Hydraulic Crimper	MSK-110	MTI Corp
Glass oven	B-585	BUCHI
Glove box	UNILAB PRO	MBRAUN
Battery cycling/testing system	BCS-805	BioLogic

2.2 Materials characterization

The structures of the samples were characterized by X-ray diffraction (XRD) using a Rigaku SmartLab X-ray powder diffractometer with Cu Kα radiation at 40 kV and 150 mA. Raman spectra were tested on a Lab-RAM HR800 spectrometer with excitation from an argon ion laser (632.81 nm). X-ray photoelectron spectroscopy (XPS) was collected using a Kratos Axis Ultra DLD spectrometer with a monochromatic Al Kα source (15 kV, 20 mA). Scanning electron microscopy (SEM) images were obtained using a JEOL JEM 6490LA equipped with a cold field emission gun, operating at 15 kV acceleration voltage. A transmission electron microscope (TEM, JEOL JEM-2200FS), capable of high resolution TEM imaging with resolution

of 0.09 Angstrom, high angle annular dark field (HAADF) scanning transmission electron microscope (STEM) imaging, as well as energy dispersive X-ray spectroscopy (EDS) analysis was used for investigating the sample morphology and the detailed crystal structure and elemental distribution of single nanoparticle. Nitrogen adsorption−desorption isotherms were acquired at –196 °C in a Quadrasorb SI sorption analyzer with the samples being degassed at 300 °C for 3 h under a vacuum in the degas port. The specific surface area was calculated with the Brunauer–Emmett–Teller (BET) model, and the pore-size distribution was calculated in accordance with the Barrett–Joyner–Halenda (BJH) method.

2.3 Electrochemical tests

2.3.1 Preparation of electrode

The working electrode was prepared by casting the thoroughly mixed slurry of active material, carbon black, and PVDF (7:2:1 or 8:1:1 in a weight ratio) in NMP solvent onto a copper foil disk (current collector， Ø = 15 mm), which was then dried at 120 °C for 12 h in a vacuum glass oven. The mass loading of active material was around 1.2 mg cm^{-2} in each electrode.

2.3.2 Assembly of CR2032 coin-type half cell

Type 2032 coin-type half cells were assembled inside an Ar filled MBraun glovebox with moisture and oxygen levels maintained below 0.1 ppm. In the Na half-cells used for tests, a sodium metal disc was used as counter and reference electrode, 1.0 M of $NaClO_4$ in only PC or a mixture solvent of EC and PC (1:1 by volume) with or without 5% FEC addition was used as electrolyte, and glass filter (Whatman) was used as a separator. In the Li half-cells used for tests, a lithium metal disc was used as the counter and reference electrode, and the electrolyte used was a solution of 1.0 M $LiPF_6$ in EC and dimethyl carbonate (DMC) (1:1 by volume).

2.3.3 Test technologies of electrochemical performance

2.3.3.1 Galvanostatic charge-discharge test

To test the cycling performance of the assembled cells, galvanostatic charge-discharge tests under different current densities were carried out on a Biologic BCS-805 multichannel battery cycling/testing system at room temperature.

2.3.3.2 Cyclic voltammetry

Cyclic voltammetry (CV) test of the cells was performed in the voltage range 0.01−2.5 V or 0.05−2.0 V (*vs.* Na^+/Na) with a scan rate of 0.1 mV s^{-1}.

2.3.3.3 Electrochemical impedance spectroscopy

Electrochemical impedance spectroscopy (EIS) of the cells before and after cycling was performed in the frequency range from 10 kHz to 0.01 Hz with an AC voltage amplitude of 5 mV. The obtained EIS was fitted by Zsimpwin software to obtain the corresponding equivalent circuit.

Chapter 3 Surface and interface engineering of anatase TiO_2 anode for sodium-ion batteries through Al_2O_3 surface modification and wise electrolyte selection

3.1 Introduction

TiO_2, with the merits of low cost, environmental friendliness, intrinsic safety and negligible volume variation, has been intensively explored as a promising anode material for secondary batteries.[1–5] Especially for NIBs,[1–3] the most electrochemically active polymorphs of TiO_2 is considered to be anatase owing to its suitable Na^+ diffusion pathways and abundance of sites for Na^+ insertion. However, it still suffers the shortcomings of low electronic and ionic conductivity.[3] Therefore, these critical issues have to be addressed before the practical application of TiO_2 within NIBs can become reality.

To date, various strategies have been proposed to improve the conductivity of active materials. Nanostructuring and surface modification are, for instance, effective solutions. In particular, active surface engineering achieved by downsizing the particles dimension to the nanometer scale benefits the reduction of ionic migration and electronic path length.[6,7] Contemporary, it also results in the realization of electrode materials with larger active surface area.[1,3] With respect to the interface engineering through surface modification, it has been suggested that the coating of TiO_2 with carbon materials could effectively separate it from the caustic electrolyte so to suppress undesirable interfacial side reactions, alleviate the decomposition of electrolytes, and enhance the electronic conductivity of the electrode.[1,2,8–12] Besides carbon materials, solid electrolytes, oxides and metal fluorides have been actively employed for the surface modification of LIBs cathode and anode. Indeed, coatings realized by employing these electrochemically less active non-carbon compounds do

not simply effectively suppress any undesired interfacial side reaction but also improve ionic conductivity, structural reversibility, and reliability of the electrode. Furthermore, with respect to the common strategies used for carbon coating, it is more feasible to realize uniform non-carbon coatings due to an easier thickness control. Specific examples are Al_2O_3-coated $LiCoO_2$,[13–15] Al_2O_3-coated $LiNi_{1/3}Co_{1/3}Mn_{1/3}O_2$,[16] Li_2SiO_3-coated $Li_{1.13}Ni_{0.30}Mn_{0.57}O_2$,[17] AlF_3-coated $Li[Li_{0.19}Ni_{0.16}Co_{0.08}Mn_{0.57}]O_2$,[18] Al_2O_3-coated $Li_4Ti_5O_{12}$[19,20] and silicon,[21,22] while reports on adopting non-carbon coating materials to modify NIBs positive or negative active materials are very scarce.

In particular, LIBs oriented electrode materials modified by Al_2O_3 coating using various methods such as physical vapour deposition (PVD), vapour-assisted hydrolysis technique, atomic layer deposition (ALD), radio frequency magnetron sputtering method and sol-gel processing have showed enhanced capacity retention and rate capability.[13–16,19–22] The reason is generally explained by the improved structural stability of the electrode, an effective surface protection capable of preventing electrolyte side reactions, and improved electrode/electrolyte interface properties owing to the formation of Li−Al−O solid solution phase coating characterized by high Li^+ ion conductivity. Similarly, when it comes to the study of Al_2O_3 coating in emerging NIBs, in 2013 Han *et al.*[23] investigated the effect of an Al_2O_3 atomic layer deposition on the cycling performance of a hybrid anode of Sn nanoparticles attached on carbon nanofibers (SnNPs@CNF). Their results revealed that the ALD-Al_2O_3 coating (6 nm thick) remarkably boosted the cycling performance of the Sn anode. This effect was attributed to the unique features of the Na−Al−O layer, being it irreversibly formed after the reaction between the Al_2O_3 coating and Na^+, similarly to the lithiation process occurring with Al_2O_3. The *in situ* TEM study confirmed the irreversible conversion from Al_2O_3 coating to Na−Al−O structure in the first sodiation stage. The authors concluded that the Na−Al−O layer acts not only as an ion transport channel for Na^+ diffusion but also as a stretchable mechanical protection layer to buffer the severe volume changes of Sn under charging/discharging process. Jung *et al.*[24] reported about sodiation and lithiation processes in Al_2O_3 using

ab initio molecular dynamics simulations. Despite the larger radius for Na^+ than Li^+, they found a much higher diffusivity for Na^+ in $Na_xAl_2O_3$ than for Li^+ in $Li_xAl_2O_3$ due to the weaker Na−O bond strength than the Li−O counterpart. These inspiring and interesting studies convey a vision that in the emerging field of NIBs, surface modification using Al_2O_3 coating could provide similar benefits as in the LIBs counterpart.

Herein we merge anatase TiO_2 nanostructuring and Al_2O_3 surface coating for the first time by a facile two-step method in order to improve the electrochemical performance of TiO_2 anode for NIBs. The electrochemical tests show that Al_2O_3 coating of TiO_2 improves the NIBs initial reversible capacity when an easy-to-prepare electrolyte formed by 1.0 M of $NaClO_4$ in PC is utilized, followed by a gradual capacity decay upon cycling. The influence of different electrolytes ($NaClO_4$ salt in various solvents) on cycling performance was then investigated for the modified sample in order to improve the cycling stability.

3.2 Experimental

Materials preparation

The two-step approach followed for the fabrication of Al_2O_3-modified TiO_2 (named as *m*-TiO_2 hereafter) nanoparticles starts from the synthesis of TiO_2 nanoparticles through hydrolysis of tetrabutyl titanate (TBT). Briefly, a solution containing 50 mL of ethanol and 0.1 mol of TBT was dropwise added into 10 mL of deionized water under magnetic stirring at room temperature. The obtained white precipitate was then dried at 110 ^oC for 6 h and subsequently calcined inside an oven at 400 ^oC for 5 h in air to obtain pure TiO_2 nanoparticles. In the second step, involving surface modification, 0.3 g of the as-prepared pure TiO_2 and 0.007 g of $Al(NO_3)_3 \cdot 9H_2O$ (with Al:Ti molar percentage of 1%) were mixed in 20 mL of deionized water. The mixture solution was stirred under magnetic stirring for 2 h followed by ultrasonication for 0.5 h. Afterward, the mixture solution was thoroughly

dried at 110 °C for 12 h and then calcined in an oven at 400 °C for 5 h in air to obtain the Al_2O_3-modified TiO_2 product.

Materials characterization

The prepared powder samples were characterized by XRD, TEM, EDS, and XPS. Details were introduced in Section 2.2.

Electrochemical tests

In the Na half-cell configuration, the used electrolyte was 1.0 M of $NaClO_4$ in only PC or a mixture solvent of EC and PC (1:1 by volume) with or without 5% FEC addition. Galvanostatic charge-discharge test and EIS test were performed. Details were introduced in Section 2.3.

3.3 Results and discussion

3.3.1 Structure, morphology, and composition characterization

Figure 3.1a depicts the XRD patterns of the as-prepared pure TiO_2 and *m*-TiO_2. The two samples show similar XRD patterns with sharp and well-defined peaks corresponding to the anatase TiO_2 profile (JCPDS No. 21−1272). In fact, no other impurity phases can be observed for *m*-TiO_2, which indicates that the TiO_2 structure is not affected by the Al_2O_3 coating. In particular, during the heat treatment at 400 °C of the as-prepared pure TiO_2 mixed with $Al(NO_3)_3$ precursor (boiling point: 135 °C), the latter component was decomposed into Al_2O_3 even though no associated peaks can be clearly observed in Figure 3.1a, suggesting the amorphous nature of Al_2O_3 due to the relatively low calcination temperature. The selection of the relatively low 400 °C calcination temperature was to avoid the anatase-to-rutile transformation and the progressive nanoparticles coalescence of TiO_2 at higher temperatures. To compare the chemical state and surface chemical composition of pure TiO_2 and *m*-TiO_2, XPS was then performed. From the high resolution Ti 2p XPS spectra (Figure 3.1b), it is seen that Al_2O_3 surface modification brings very limited change to the Ti 2p component,

where for both samples the two Ti $2p_{3/2}$ and Ti $2p_{1/2}$ peaks are located at 458.8 and 464.5 eV, respectively. The positions and shapes of the Ti 2p peaks indicate that the predominant state of the Ti element in TiO_2, before and after Al_2O_3 surface modification, is in fact Ti^{4+}.[25–27] On the other hand, the observed Al 2p peak at 74.5 eV (Figure 3.1c) correlates to and confirms the presence of amorphous Al_2O_3 in the *m*-TiO_2.[28,29] This latter result, combined with the XRD analysis, indicates that amorphous Al_2O_3 coating is formed on the surface of nanostructured anatase TiO_2.

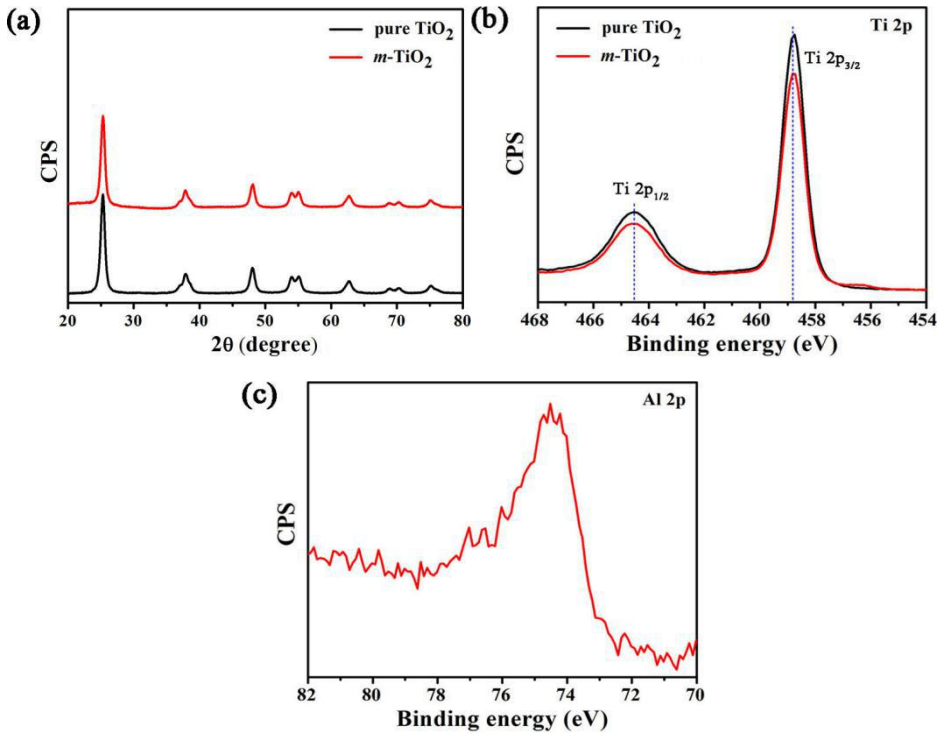

Figure 3.1 (a) XRD patterns of the as-prepared pure TiO_2 and m-TiO_2. (b) Ti 2p XPS spectra of pure TiO_2 and m-TiO_2 and (c) Al 2p XPS spectrum of m-TiO_2.

TEM images of pure TiO_2 and *m*-TiO_2 are compared in Figure 3.2a. The pure TiO_2 nanoparticles display a morphology of porous spherical aggregates with diameter of about 50−80 nm composed of many nanosized primary crystallites (Figure 3.2a) which is interestingly similar to the morphology of *m*-TiO_2 (Figure 3.2c). The high resolution TEM (HRTEM) images of pure TiO_2 and *m*-TiO_2 (Figure 3.2b and d, respectively) clearly reveal the lattice fringes of well crystallized TiO_2 nanocrystals with an average diameter of 13 nm in an aggregate configuration (*i.e.*, by employing

the Scherrer equation on XRD shown in Figure 3.1a we obtained 13.2 nm for pure TiO_2 and 13.6 nm for *m*-TiO_2). The interplanar spacing of 0.35 nm for both samples corresponds to the (101) lattice planes of anatase TiO_2. Notably, a thin layer of amorphous material (less than 1 nm) can be observed in Figure 3.2d, which is ascribed to Al_2O_3 based on the aforementioned XPS results. EDS mapping was also performed to check the uniformity of the Al_2O_3 coating layer on the surface of TiO_2 particles (Figure 3.2e). The results highlight the uniform dispersion of Al, Ti, and O elements in the Al_2O_3-modified TiO_2 sample, indicative of the existence and uniformity of Al_2O_3 coating. Based on the EDS analysis, the molar ratio of Al:Ti:O is found to be approximately 0.4:43.2:56.4, giving an Al:Ti molar percentage of about 0.9%, which well agrees with the expected value of 1%.

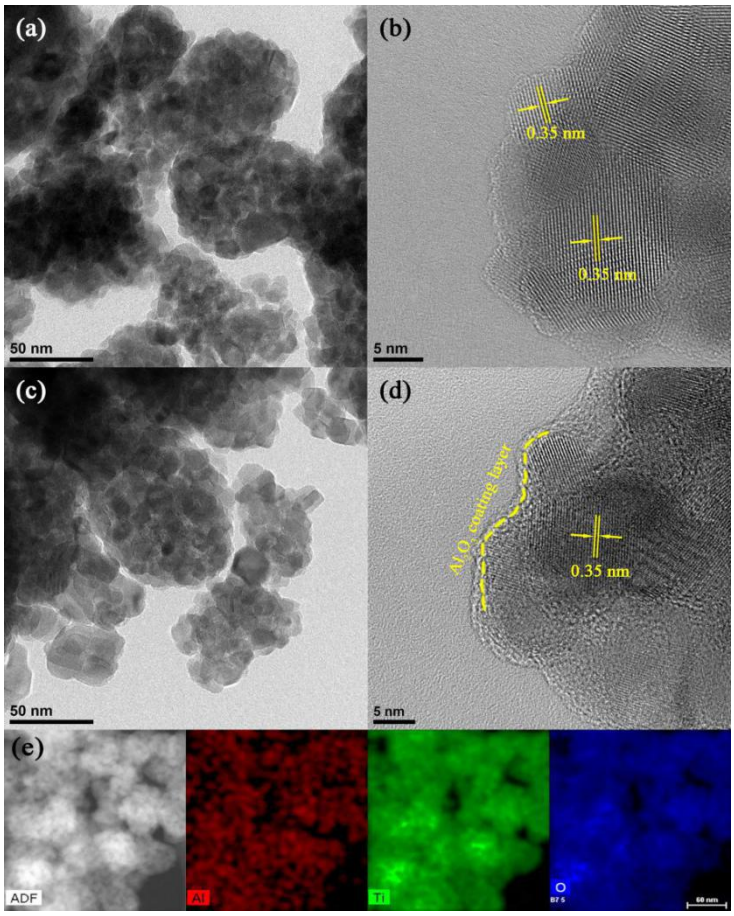

Figure 3.2 TEM and high resolution TEM (HRTEM) images of (a, b) pure TiO_2 and (c, d) m-TiO_2. (e) HAADF-STEM image of m-TiO_2 and the corresponding EDS elemental mappings of Al, Ti, and O.

3.3.2 Electrochemical properties for sodium storage

Effect of Al_2O_3 surface coating

The electrochemical performance of the pure TiO_2 and *m*-TiO_2 products as anodes for NIBs was first investigated using an easy-to-prepare electrolyte formed by 1.0 M of $NaClO_4$ in PC. From the initial charge/discharge voltage curves at 0.1C (1C= 335 mA g^{-1}) shown in Figure 3.3, *m*-TiO_2 with Al_2O_3 surface coating is found to deliver higher charge/discharge capacities than pure TiO_2. The large capacity loss during the first cycle for both samples can be attributed to the irreversible initial sodiation along with partial decomposition of TiO_2, to the decomposition of the PC solvent, and to the formation of solid electrolyte interface (SEI) layer as well as to some side reactions occurring in the interfaces with the electrolytes.[1,3,8–12,30] It should be pointed out that, especially for *m*-TiO_2, the Al_2O_3 surface coating can react, during the initial sodiation process, with Na^+ to form a Na−Al−O glass phase (see the following discussion on the role of Al_2O_3), which is responsible for a large irreversible capacity. On the other hand, owing to the beneficial sodium ion conductivity of Na−Al−O, the Al_2O_3 coated sample can deliver larger reversible (charge) capacity than pure TiO_2, although the initial Coulombic efficiency is slightly lower (as listed in Table 3.1). Moreover, both the voltage profiles of pure TiO_2 and *m*-TiO_2 present the typical electrochemical characteristics of anatase TiO_2, exhibiting a discharging/charging voltage plateau at about 0.5/0.8 V during the sodiation/desodiation processes .

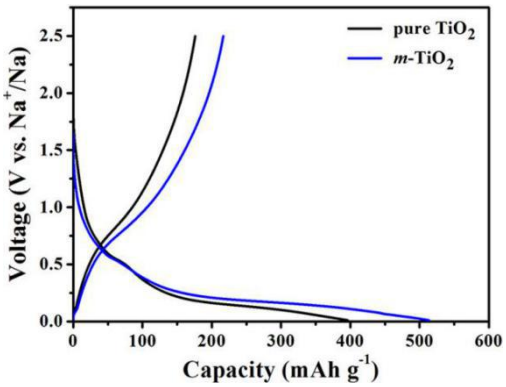

Figure 3.3 Galvanostatic charge-discharge voltage curves of the initial cycle for pure TiO_2 and m-TiO_2 at the rate of 0.1C using 1.0 M of $NaClO_4$ in PC as the electrolyte.

Table 3.1 Cycling properties of pure TiO_2 and m-TiO_2 at the rate of 0.1C using 1.0 M of $NaClO_4$ in PC as electrolyte.

Sample	1st charge capacity (mAh g^{-1})	1st Coulombic efficiency	Average Coulombic efficiency (from the 20th cycle)	Reversible (charge) capacity/50th cycle (mAh g^{-1})
pure TiO_2	176.0	44.3%	95.0%	111.7
m-TiO_2	216.6	42.2%	97.5%	131.4

The cycling performances at 0.1C of pure TiO_2 and *m*-TiO_2 based electrodes are displayed in Figure 3.4. For pure TiO_2 (Figure 3.4a), the capacity fades gradually during the first 30 cycles to end with an obvious decline during the last 20 cycles. The Coulombic efficiency rises quickly in the first few cycles to a high value of about 92% and sustains over this value throughout the following cycles. After implementing Al_2O_3 surface modification (Figure 3.4b), the sample is found to deliver an improved reversible capacity although a gradually fading trend could still be observed. The Coulombic efficiency increases slowly from the second cycle but reaches a high value around 98% after about 20 cycles and maintains an overall stability thereafter. The average Coulombic efficiency calculated from the 20th cycle and the reversible capacity after 50 cycles of both samples are also listed in Table 3.1. From these data it is clear the beneficial effect of Al_2O_3 coating with *m*-TiO_2 exhibiting improved performance compared to pure TiO_2 in terms of both achievable reversible capacity and Coulombic efficiency.

To better understand the Na ion storage mechanism into TiO_2 and the effect of Al_2O_3 coating on the cell overall performance, differential capacity plots at various cycles for pure TiO_2 and *m*-TiO_2 are reported. As shown in Figure 3.4c and d, the first cycle profiles are each other similar. For both samples, the small cathodic peak at around 0.75 V is due to the reductive electrolyte decomposition and irreversible

formation of SEI layer wheras the obvious cathodic peak occurring at about 0.55 V can be attributed to the reaction of Na^+ insertion into TiO_2 anatase lattice.[1,3,8–12,30] The large cathodic peak at lower voltage of 0.2 V which disappears in the following cycles can be assigned to the decomposition of electrolyte at lower potentials, the partial decomposition of TiO_2 as well as some side reactions at the interfaces.[1,12] The broad anodic peak centered at about 0.8 V results from the reversible desodiation process in TiO_2 matrix. In addition, another pair of small cathodic/anodic peaks at about 0.03/0.09 V can also be observed, which are ascribed to the reversible sodium storage in conductive carbon black.[2,7]

Notably, due to irreversible processes, the first cycle plot shows very different features from the subsequent cycles. To start, the TiO_2 sodiation peak located at about 0.55 V in the first cycle shifts towards higher potentials during the second cycle to maintain the new voltage position for the remaining cycling process (about 0.63 V for pure TiO_2 and 0.70 V for *m*-TiO_2), a behavior that can be explained through a decreased overpotential for the reversible sodium-ion storage. Furthermore, for pure TiO_2 the anodic peak referring to the typical desodiation of anatase TiO_2 is found not to be stable as gradually shifts towards higher potentials upon cycling (indicated by the black arrow) (Figure 3.4c), a different behavior from *m*-TiO_2 where the peak is stabilized at around 0.79 V for any considered cycle number (Figure 3.4d). In particular, the voltage difference between the sodiation/desodiation peaks of TiO_2 (ΔV) based on Ti^{3+}/Ti^{4+} redox couple is higher for pure TiO_2 than for *m*-TiO_2 and keeps increasing from the second cycle onward (see inset in Figure 3.4c). Vice versa, the ΔV for *m*-TiO_2 shows a stable behavior at a much lower potential set around 0.1 V after the first cycle (see inset in Figure 3.4d). These results suggest that Al_2O_3 coating can facilitate Na^+ insertion/extraction and a better reversibility of *m*-TiO_2 during cycling,[3] which could well explain the higher reversible capacity of *m*-TiO_2 shown in Figure 3.3 and Figure 3.4. Indeed, the surface coating of the electrochemically less active Al_2O_3, in complement of the native SEI layer, can surpress the electrolyte decomposition at lower potentials, namely acting as as an 'artificial' SEI layer.[21,31,32]

According to the report of Han *et al.*[23] we propose that this 'artificial' SEI layer associated to Al_2O_3 is actually an irreversibly formed Na-Al-O glass film upon the first sodiation. This mechanically durable Na−Al−O glass film with good ionic conductivity could improve the electrode/electrolyte interface properties and the structural stability of the active material upon repeated sodiation/desodiation processes. Finally, no visible peaks related to the reaction between Al_2O_3 coating and Na^+ can be found in the first cycle from Figure 3.4d, possibly due to the overlapping with other irreversible interface reactions at low potentials and/or because of the very low amount of applied Al_2O_3.

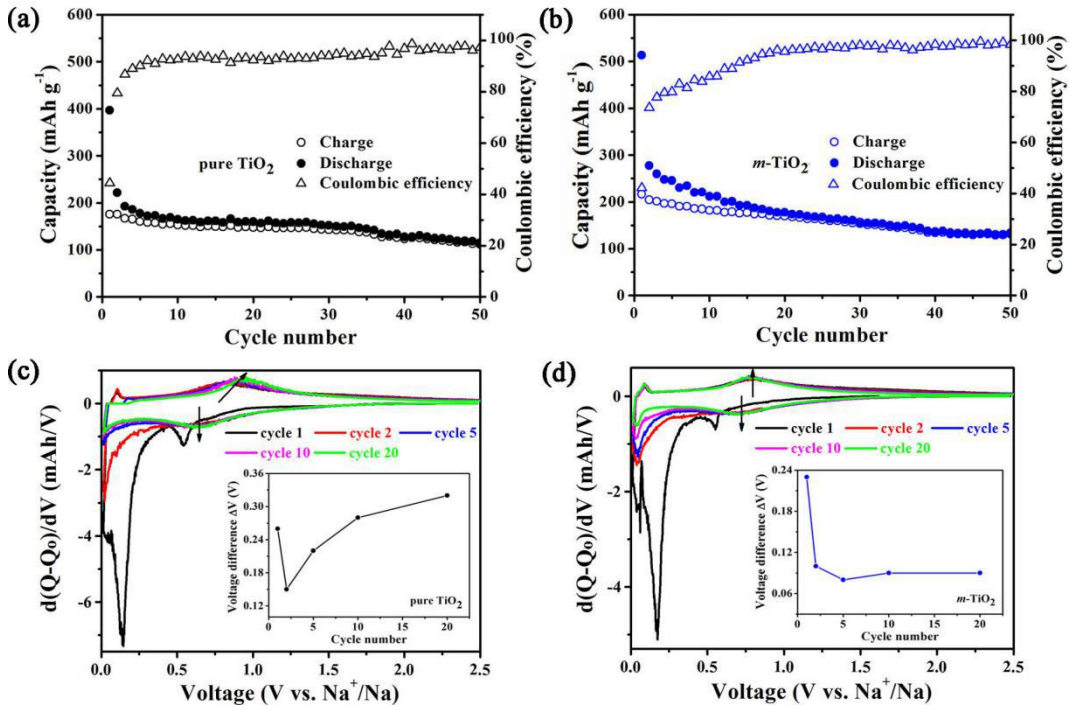

Figure 3.4 (a, b) Cycling performances at the rate of 0.1C of (a) pure TiO_2 and (b) m-TiO_2 using 1.0 M of $NaClO_4$ in PC. (c, d) Differential capacity plots at different cycles of (c) pure TiO_2 and (d) m-TiO_2 in the voltage range of 0.01−2.5 V vs. Na^+/Na. The insets in (c) and (d) are the corresponding voltage difference between the redox peaks of TiO_2 (ΔV) vs. cycle number plot illustrating the change of ΔV upon cycling.

These results strongly suggest that surface engineering through the coating of TiO_2 by a thin Al_2O_3 layer is beneficial for Na^+ diffusion kinetics hence for the specific anode capacity. However, the *m*-TiO_2 sample still displays a gradual capacity

decay upon cycling when an easy-to-prepare electrolyte composed by 1.0 M of $NaClO_4$ in PC is utilized. Therefore, we have analyzed the influence of different electrolytes ($NaClO_4$ salt with different solvents) on the cycling performance with the purpose of finding meaningful electrolyte formulation-TiO_2 coating correlations addressing the cycling stability.

Influence of different electrolytes

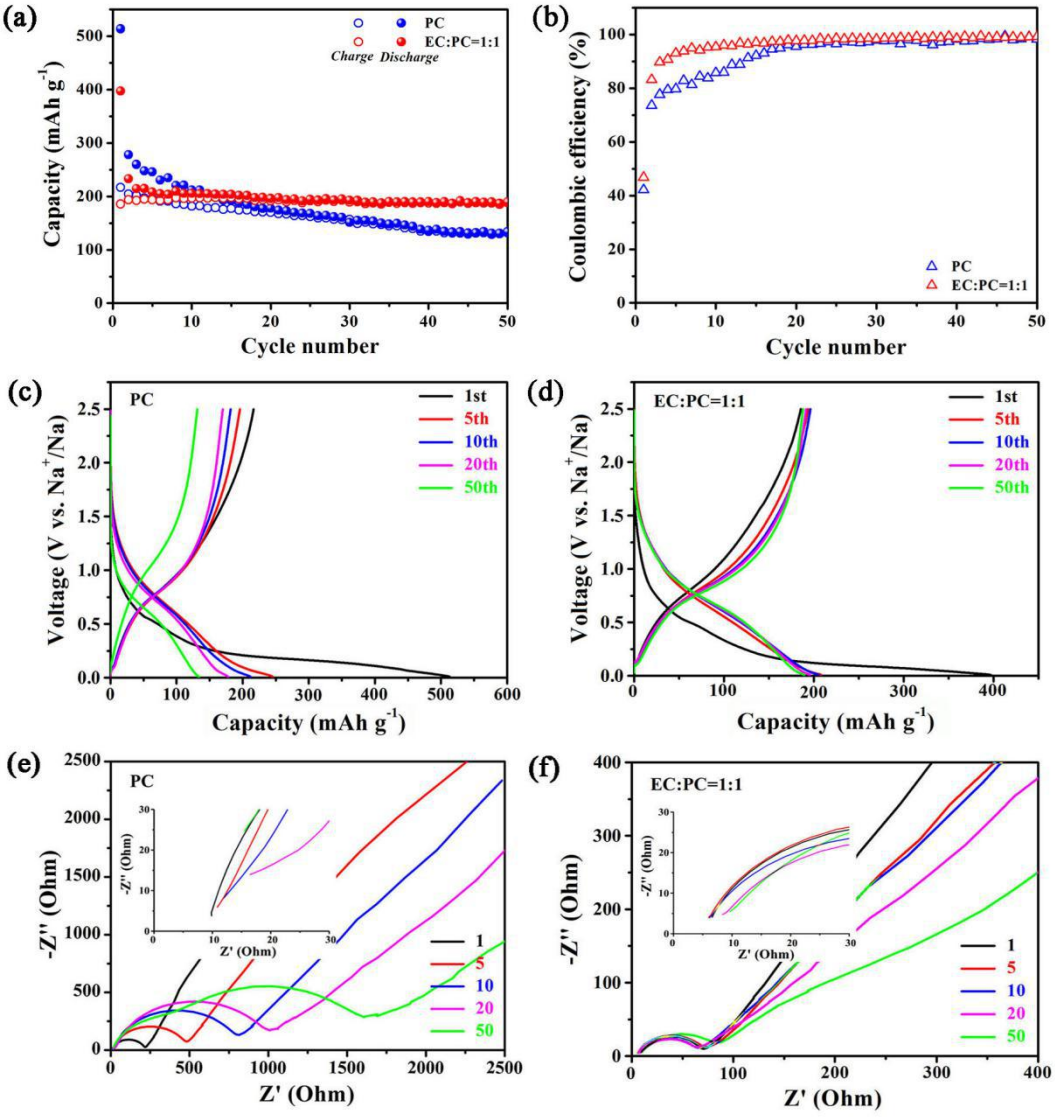

Figure 3.5 (a) Cycling performance and (b) Coulombic efficiency at 0.1C rate of m-TiO_2 in PC and EC:PC=1:1 based electrolyte. (c, d) Galvanostatic charge-discharge voltage curves of different cycles for m-TiO_2 at 0.1C rate in (c) PC based and (d) EC:PC=1:1 based electrolyte. (e, f) EIS at different cycle numbers of m-TiO_2 at fully charged state with (e) PC based and (f) EC:PC=1:1 based electrolyte. Enlarged views are shown in the insets.

The first new solvent that was considered in order to go beyond the PC related performance was realized by mixing EC:PC (1:1 by volume). In this new electrolytic environment, and as shown in Figure 3.5a, *m*-TiO_2 was found to exhibit far superior cycling stability and reversible capacity with respect to the data shown in Figure 3.4b, where simply PC is utilized. In particular, after 50 cycles, the reversible capacity in the binary EC:PC solvent mixture reaches 188.1 mAh g^{-1}, remarkably higher than the previously obtained 131.4 mAh g^{-1} for only PC. Similarly, the Coulombic efficiency in EC:PC is noticeably improved during the first 20 cycles (Figure 3.5b) with a first cycle efficiency of 46.7% (42.2% for PC) and an average Coulombic efficiency of 98.7% (97.5% for PC) from the 20th cycle onward. Figure 3.5a highlights the severe capacity fading in case of PC only configuration (0.73% per cycle) which is strongly suppressed when the EC:PC mixture is used (0.06% per cycle). This strong PC-only related capacity fading, together with a lower Coulombic efficiency, can be ascribed to an unstable SEI formation, as similar results have already been reported on hard carbon and anatase TiO_2 anodes for NIBs.[33,34]

It has been suggested that by adding into the electrolyte a few percent of FEC, one of the best-known and most studied molecule in LIBs and NIBs, could significantly enhance the cycling performance of the electrodes owing to the formation of a kinetically stable and highly ionically conductive fluorine-based SEI.[35–39] Hence, we further considered a mixture of 5% FEC in EC:PC, as shown in Figure 3.6a. Interestingly, our results demonstrate that FEC does not improve the performance of the cell compared with the FEC-free EC:PC configuration, on the contrary a slightly lower reversible capacity than the FEC-free configuration of 186.8 mAh g^{-1} is obtained after 50 cycles. It is worth stressing that this result seems to contradict a number of previous studies,[35–39] as here FEC does not improve in any way the performance of the TiO_2-based anodes. Nonetheless, a study on anatase TiO_2 for NIB anodes from Wu *et al.*[33] also showed that the addition of FEC into a EC:PC based electrolyte could slightly diminish the Coulombic efficiency and specific capacity of the cell, while Ponrouch *et al.*[40] found negative effects of FEC on hard

carbon electrode for NIBs, *i.e.*, a reduced first cycle efficiency and an increased polarization, presumably resulting from a less conductive SEI. From the initial charge-discharge voltage curve shown in Figure 3.6b we can see that when FEC is considered, besides the discharge voltage plateau at about 0.5 V due to TiO_2, another distinct discharge plateau around 1.1 V emerges, which is likely due to the decomposition of FEC.[3,10] Furthermore, it is clear from our data that a large capacity fading upon cycling is observed when only PC is employed (Figure 3.5c), whereas for EC:PC based electrolyte (regardless the presence of FEC) a remarkable overlapping among the profiles associated to different cycle numbers is noted (Figure 3.5d and Figure 3.6b), indicating a stable electrochemical performance during the charge/discharge process.

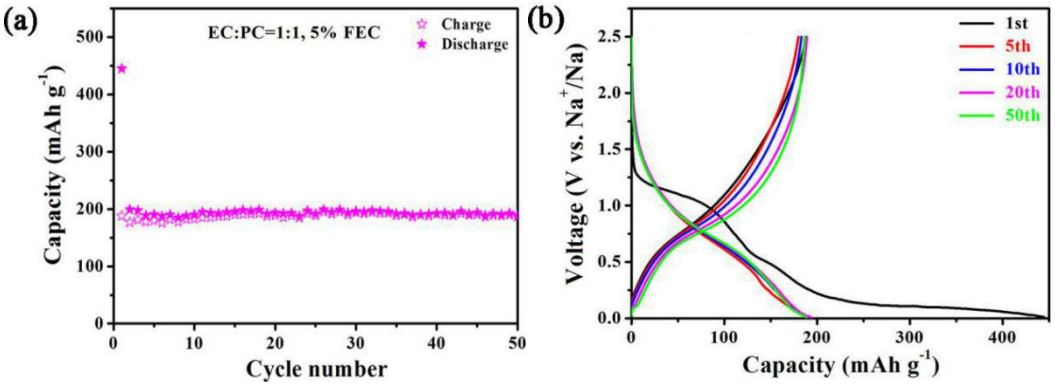

Figure 3.6 (a) Cycling performance and (b) galvanostatic charge-discharge voltage curves of different cycles for m-TiO_2 at 0.1C rate in EC:PC=1:1 based electrolyte with 5% FEC addition.

To further improve our knowledge on the effect of different electrolytes on the cycling performance of *m*-TiO_2, fully charged state Electron Impedance Spectroscopy (EIS) at different cycle numbers in only PC and EC:PC based electrolytes was conducted. As depicted in Figure 3.5e and f, in the high frequency region the Nyquist profiles show intercepts with the Z' axis which are related to the ohmic resistance (R_s) of the electrolyte, separator and current collector. From the enlarged views shown in the insets, we can notice a R_s reduction, regardless the cycle number, when moving from PC to EC:PC. In particular, when all cycles from 1 to 50 are considered, a

resistance in the range 10−15 Ω is found for PC, which reduces down to 6−10 Ω for EC:PC. Furthermore, both cases share the common feature of a depressed semicircle in the high-to-medium frequency region followed by an inclined line in the low frequency region.[41–44] Generally, these semicircles can be decomposed into two arcs (as clearly visible for PC at 50 cycles) which correspond to the resistance for Na^+ migration through the SEI film (R_{SEI}) and the charge transfer resistance (R_{ct}) at the electrode/electrolyte interface, whereas the inclined line represents the Warburg impedance (Z_w) associated with sodium ions diffusion in the bulk of the electrode.[44] From a quick reading of the figure, we can also clearly observe a much larger semicircle and an obvious increasing trend of the resistance with cycling in PC when compared with the EC:PC configuration. Specifically, an equivalent circuit (Figure 3.7) is proposed to fit the Nyquist plots. In this model, constant phase elements (CPE) replace the pure capacitance (CPE_1 and CPE_2) and the Warburg component (Z_W(CPE)) for a better fitting of the impedance data. The obtained values for the interface resistance $R_{int} = R_{SEI} + R_{ct}$, calculated under different cycle numbers using the equivalent circuit for *m*-TiO_2 in different electrolytes, are summarized in Table 3.2. The results clearly highlight two important aspects about R_{int} for PC only electrolyte: i) It is sensibly larger than in EC:PC based electrolytes regardless the cycle number; ii) It shows a significant increase upon cycling while no appreciable differences are found for EC:PC based electrolyte. These observations suggest the formation of a continuously growing (unstable) SEI layer for the PC only electrolyte whereas a stable and conductive SEI is formed when EC:PC is employed, confirming the superior capacity retention of the latter as shown in Figure 3.5a. The importance of the electrolyte is confirmed also by the cycling behaviour of pure TiO_2 at 0.1C in EC:PC=1:1, as shown in Figure 3.8. Indeed, the plot exhibits improved cycling stability, higher Coulombic efficiency (initial: 45.1%, average value from the 20th cycle: 96.7%) and enhanced reversible capacity than when PC-only electrolyte is considered (Figure 3.5a and Table 3.1). Furthermore, the figure again confirms the importance of a proper coating, being the reversible capacity of pure TiO_2 equals to

162.5 mAh g^{-1} after 50 cycles, about 13.6% lower than the corresponding value measured for *m*-TiO_2.

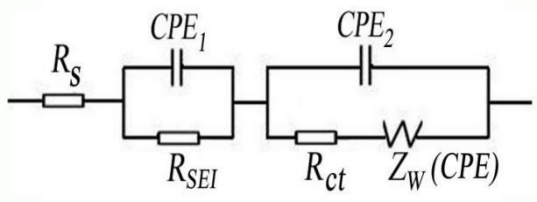

Figure 3.7 Equivalent circuit model to fit the Nyquist plots.

Table 3.2 R_{int} under different cycle numbers obtained by fitting the experimental data using the equivalent circuit for m-TiO_2 in different solvents (with 1.0 M of $NaClO_4$).

	R_{int} (Ω)				
electrolyte	1st cycle	5th cycle	10th cycle	20th cycle	50th cycle
1.0 M of $NaClO_4$ in PC	208	467	803	997	1604
1.0 M of $NaClO_4$ in EC:PC=1:1	64	68	60	58	74

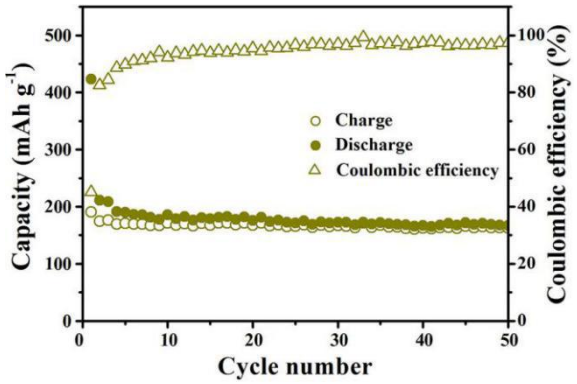

Figure 3.8 Cycling performance of pure TiO_2 at the rate of 0.1C employing 1.0 M of $NaClO_4$ in EC:PC=1:1 as the electrolyte.

The above cycling performance together with EIS study demonstrate that the formation of stable and conductive SEI film is of significant importance to make the modified TiO_2 fully play its potential in sodium-ion storage. In other words, besides surface coating, the electrolyte section also plays a key role in the final performance

of the electrode materials. Thus engineering the interface between the active materials and the electrolyte should be considered a crucial aspect to address, possibly also explaining the positive role of FEC additive especially in LIBs to limit the dramatic volume variation upon cycling. In the present study, our results show that for TiO_2, where a negligible volume modification occurs, the binary FEC-free EC:PC based electrolyte provides the best electrochemical performance.

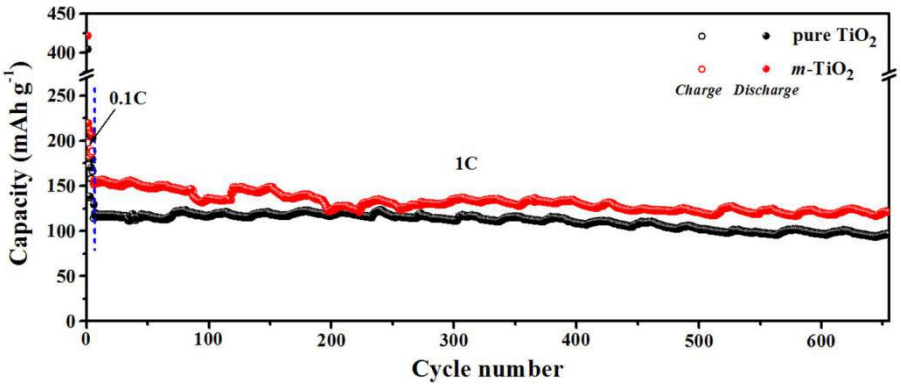

Figure 3.9 Long-term cycling performance at 1C rate for 650 cycles (with the electrode first activated at the low current of 0.1C for 5 cycles) of m-TiO_2 and pure TiO_2 employing 1.0 M of $NaClO_4$ in EC:PC=1:1 as electrolyte.

Figure 3.9 depicts the *m*-TiO_2 electrochemical response when FEC-free EC:PC is used as electrolyte with a cycling rate of 1C (with the electrode first activated at the low current of 0.1C for 5 cycles). As shown in the figure, an excellent enduring stability without evident capacity decay is achieved during the long-term cycling, and finally, a high reversible capacity of 120.8 mAh g^{-1} is measured after 650 cycles at 1C (red line). In contrast, a lower reversible capacity of 96.8 mAh g^{-1} is achieved after 650 cycles when pure TiO_2 is considered (black line). The rate capability of *m*-TiO_2 for C rates up to 5C was also evaluated, as illustrated in Figure 3.10. The charge capacities are 187.9, 151.1, 133.4, 118.7, and 94.3 mAh g^{-1} at the rates of 0.1, 0.5, 1, 2 and 5C, respectively. Importantly, when the current was set back to 0.1C after 50 cycles, the capacity could rise back up to 193.8 mAh g^{-1}, indicating an excellent tolerance for a rapid Na^+ insertion and extraction. In comparison, the charge capacities of pure TiO_2 at the corresponding rates are 176.9, 143.0, 126.8, 111.0, and

86.5 mAh g^{-1}, respectively. It is noticed that despite the Al_2O_3 layer, which has been demonstrated to introduce benefits in terms of achieved specific capacity, the rate capabilities of TiO_2 crystals are not negatively affected by a potentially resistive contribute.

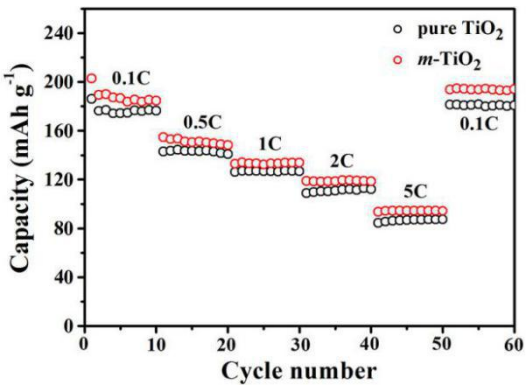

Figure 3.10 Rate performances (charge capacities) of pure TiO_2 and m-TiO_2 at rates from 0.1 to 5C employing 1.0 M of $NaClO_4$ in EC:PC=1:1 as the electrolyte.

Discussion on the role of Al_2O_3 surface coating

Based on previous reports,[23] the enhanced electrochemical performances of *m*-TiO_2 compared to pure TiO_2 can be ascribed to the Na−Al−O surface layer irreversibly formed from the reaction between the Al_2O_3 coating and Na^+ during the first sodiation stage. To tentatively confirm the formation of Na−Al−O surface layer, post-mortem XPS analysis on *m*-TiO_2 electrode was performed (Figure 3.11). After running for one cycle, we found a shift towards high binding energy of the Al 2p peak, reaching a value around 75.4 eV, which can be related to the formation of Na–Al–O glass phase during the initial sodiation process.[21] After five cycles, the peak position of Al 2p almost remains unchanged, implying an irreversible conversion from Al_2O_3 to Na−Al−O glass phase and a remarkable stability of Na−Al−O surface layer upon cycling. This mechanically durable layer is beneficial for the structural stability of the active materials upon cycling. However, the specific composition of the formed Na−Al−O layer is currently not known as it will be matter of future investigation.

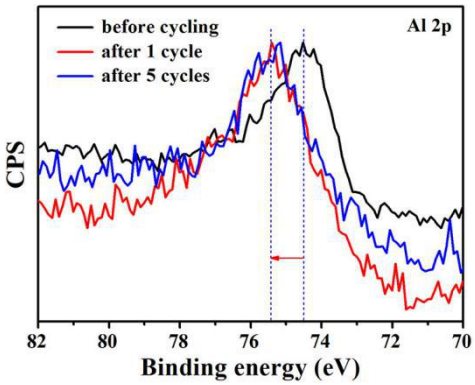

Figure 3.11 High resolution XPS spectra of Al 2p taken on m-TiO_2 before cycling, after 1 cycle and after 5 cycles at the rate of 0.1C .

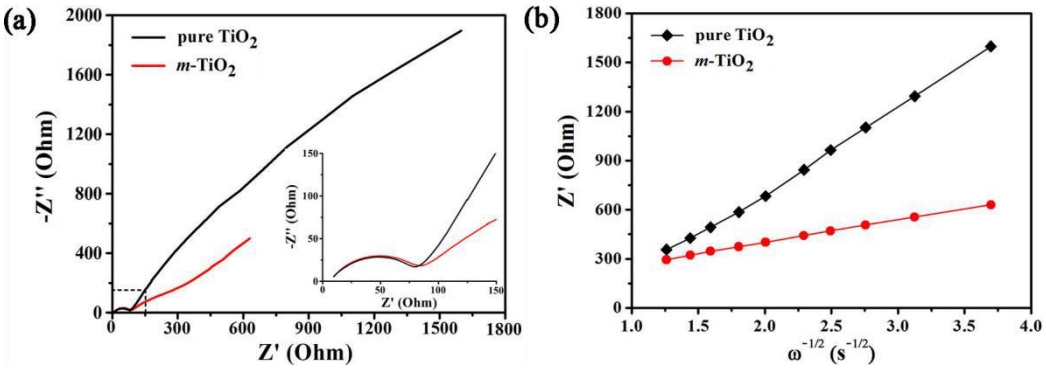

Figure 3.12 (a) EIS of m-TiO_2 and pure TiO_2 after 50 cycles at the rate of 0.1C employing the optimized electrolyte formed by 1.0 M of $NaClO_4$ in EC:PC=1:1. The inset is the enlarged view of the high frequency region. (b) Relationship between Z' and $\omega^{-1/2}$ in the low frequency region obtained from the EIS curves.

Finally, to better reveal the key role of Al_2O_3 surface coating in enhancing the reversible capacity and Coulombic efficiency of TiO_2, EIS of coated and uncoated samples after 50 cycles was conducted, as displayed in Figure 3.12a. The employed electrolyte is 1.0 M of $NaClO_4$ in EC:PC=1:1 without FEC additive. From the inset it is observed that the depressed semicircles for the two samples are very similar to each other, and the diameter associated to *m*-TiO_2 is only slightly larger than the corresponding diameter for pure TiO_2, which is explained through the introduction of a small amount of insulating layer (Al_2O_3 surface coating).[13,15,19] Indeed, the interface resistance R_{int} obtained using the equivalent circuit depicted in Figure 3.7 is about 69 Ω for pure TiO_2 and 74 Ω for *m*-TiO_2 after 50 cycles. Furthermore, considering that

the irreversibly formed Na–Al–O glass phase after the first cycle was reported to have high diffusivity for Na^+,[23,24] we compared the Na^+ diffusion kinetics associated Warburg impedance in the TiO_2 electrodes with and without Al_2O_3 coating. The Warburg impedance can be extrapolated from the liner contribution of EIS in the low frequency region. From the Z' *vs.* $\omega^{-1/2}$ plots of pure TiO_2 and *m*-TiO_2 shown in Figure 3.12b, the obtained Warburg factor σ (determined by the slope of the line) is 135.6 for *m*-TiO_2 and 508.7 for pure TiO_2, where smaller Warburg impedance means faster Na^+ diffusion. This result supports the thesis that irreversibly formed Na–Al–O glass phase acts as an ion transport channel and improves Na ions diffusion into the TiO_2 nanoparticles, thus delivering a higher reversible capacity and Coulombic efficiency.

3.4 Conclusions

Nanostructured anatase TiO_2 with Al_2O_3 surface coating has been successfully prepared by a facile two-step approach and investigated for the first time as anode for NIBs. This modified TiO_2 electrode exhibits enhanced cycling performance compared to the pristine one owing to the irreversible formation of Na−Al−O surface layer after sodiation which was confirmed by post-mortem XPS analysis. The study on the influence of different solvents on the electrode cycling performance revealed that the binary EC:PC solvent mixture could lead to an excellent cyclability with no need of the commonly used FEC additive. In particular, under the best configuration, the Al_2O_3-modified nanostructured anatase TiO_2 could deliver a reversible capacity as high as 188.1 mAh g^{-1} at 0.1C after 50 cycles, good rate capability up to 5C, and long-term cycling performance for 650 cycles at a high rate of 1C. This improved electrochemical performance makes nanostructured Al_2O_3-modified anatase TiO_2 a promising anode for cost-effective NIBs, and it suggests the importance of a proper surface and interface engineering. Indeed, the present study does not stress only on the importance of the morphological characteristics of engineered TiO_2 and Al_2O_3-modified surface, but also bounds its benefits to the boundary conditions such as the employed electrolytic solutions. This correlation is believed to be essential in

future design of composite anode materials for NIBs, where electrolytes stability, improved electronic and ionic transport and material integrity upon cycling can be achieved by proper functionalization of the active material surfaces.

3.5 References

1. M.N. Tahir, B. Oschmann, D. Buchholz, X. Dou, I. Lieberwirth, M. Panthofer, W. Tremel, R. Zentel, S. Passerini, *Adv. Energy Mater.* 6 (2016) 1501489.
2. X. Zhu, Q. Li, Y. Fang, X. Liu, L. Xiao, X. Ai, H. Yang, Y. Cao, *Part. Part. Syst. Charact.* 33 (2016) 545–552.
3. J. Chen, Z. Ding, C. Wang, H. Hou, Y. Zhang, C. Wang, G. Zou, X. Ji, *ACS Appl. Mater. Interfaces* 8 (2016) 9142–9151.
4. S. Goriparti, E. Miele, M. Prato, A. Scarpellini, S. Marras, S. Monaco, A. Toma, G.C. Messina, A. Alabastri, F.D. Angelis, L. Manna, C. Capiglia, R.P. Zaccaria, *ACS Appl. Mater. Interfaces* 7 (2015) 25139–25146.
5. S. Goriparti, E. Miele, F.D. Angelis, E.D. Fabrizio, R.P. Zaccaria, C. Capiglia, *J. Power Sources* 257 (2014) 421–443.
6. D. Su, S. Dou, G. Wang, *Chem. Mater.* 27 (2015) 6022–6029.
7. Y. Li, J. Su, X. Lv, Y. Long, Y. Wen, *Electrochim. Acta* 182 (2015) 596–603.
8. A. Henry, N. Louvain, O. Fontaine, L. Stievano, L. Monconduit, B. Boury, *ChemSusChem* 9 (2016) 264–273.
9. K.-T. Kim, G. Ali, K.Y. Chung, C.S. Yoon, H. Yashiro, Y.-K. Sun, J. Lu, K. Amine, S.-T. Myung, *Nano Lett.* 14 (2014) 416–422.
10. S.M. Oh, J.-Y. Hwang, C.S. Yoon, J. Lu, K. Amine, I. Belharouak, Y.-K. Sun, *ACS Appl. Mater. Interfaces* 6 (2014) 11295–11301.
11. F. Yang, Z. Zhang, Y. Han, K. Du, Y. Lai, J. Li, *Electrochim. Acta* 178 (2015) 871–876.
12. Y. Xiong, J. Qian, Y. Cao, X. Ai, H. Yang, *ACS Appl. Mater. Interfaces* 8 (2016) 16684–16689.
13. F. Zhao, Y. Tang, J. Wang, J. Tian, H. Ge, B. Wang, *Electrochim. Acta* 174 (2015) 384–390.
14. J. Cho, Y.J. Kim, B. Park, *Chem. Mater.* 12 (2000) 3788–3791.
15. Y.S. Jung, A.S. Cavanagh, A.C. Dillon, M.D. Groner, S.M. George, S.-H. Lee, *J. Electrochem. Soc.* 157 (2010) A75–A81.
16. Y. Kim, H.S. Kim, S.W. Martin, *Electrochim. Acta* 52 (2006) 1316–1322.
17. E. Zhao, X. Liu, H. Zhao, X. Xiao, Z. Hu, *Chem. Commun.* 51 (2015) 9093–9096.
18. Y.-K. Sun, M.-J. Lee, C.S. Yoon, J. Hassoun, K. Amine, B. Scrosati, *Adv.*

Mater. 24 (2012) 1192–1196.

19. D. Ahn, X. Xiao, *Electrochem. Commun.* 13 (2011) 796–799.
20. Y. Wang, W. Zou, Z. Huang, J. Li, *ECS Trans.* 59 (2014) 35–43.
21. H.T. Nguyen, M.R. Zamfir, L.D. Duong, Y.H. Lee, P. Bondavalli, D. Pribat, *J. Mater. Chem.* 22 (2012) 24618–24626.
22. S.-Y. Kim, Y. Qi, *J. Electrochem. Soc.* 161 (2014) F3137–F3143.
23. X. Han, Y. Liu, Z. Jia, Y. Chen, J. Wan, N. Weadock, K.J. Gaskell, T. Li, L. Hu, *Nano Lett.* 14 (2014) 139–147.
24. S.C. Jung, H.-J. Kim, J.W. Choi, Y.-K. Han, *Nano Lett.* 14 (2014) 6559–6563.
25. Y. Ma, H.D. Asfaw, C. Liu, B. Wei, K. Edström, *Nano Energy* 30 (2016) 745–755.
26. J.-Y. Hwang, S.-T. Myung, J.-H. Lee, A. Abouimrane, I. Belharouak, Y.-K. Sun, *Nano Energy* 16 (2015) 218–226.
27. J. Ni, S. Fu, C. Wu, J. Maier, Y. Yu, L. Li, *Adv. Mater.* 28 (2016) 2259–2265.
28. S.-O. Kim, A. Manthiram, *J. Power Sources* 332 (2016) 222–229.
29. E. Allcorn, A. Manthiram, *ACS Appl. Mater. Interfaces* 6 (2014) 10886–10891.
30. L. Wu, D. Bresser, D. Buchholz, G.A. Giffin, C.R. Castro, A. Ochel, S. Passerini, *Adv. Energy Mater.* 5 (2015) 1401142.
31. H. Kou, X. Li, H. Shan, L. Fan, B. Yan, D. Li, *J. Mater. Chem. A* 5 (2017) 17881–17888.
32. J. Liu, X. Sun, *Nanotechnology* 26 (2015) 024001.
33. L. Wu, D. Buchholz, D. Bresser, L.G. Chagas, S. Passerini, *J. Power Sources* 251 (2014) 379–385.
34. A. Ponrouch, E. Marchante, M. Courty, J.-M. Tarascon, M.R. Palacín, *Energy Environ. Sci.* 5 (2012) 8572–8583.
35. H. Lu, L. Wu, L. Xiao, X. Ai, H. Yang, Y. Cao, *Electrochim. Acta* 190 (2016) 402–408.
36. W. Luo, P. Zhang, X. Wang, Q. Li, Y. Dong, J. Hua, L. Zhou, L. Mai, *J. Power Sources* 304 (2016) 340–345.
37. S. Komaba, T. Ishikawa, N. Yabuuchi, W. Murata, A. Ito, Y. Ohsawa, *ACS Appl. Mater. Interfaces* 3 (2011) 4165–4168.
38. K. Eom, J. Jung, J.T. Lee, V. Lair, T. Joshi, S.W. Lee, Z. Lin, T.F. Fuller, *Nano Energy* 12 (2015) 314–321.
39. K. Schroder, J. Alvarado, T.A. Yersak, J. Li, N. Dudney, L.J. Webb, Y. Meng, K.J. Stevenson, *Chem. Mater.* 27 (2015) 5531–5542.
40. A. Ponrouch, A.R. Goñi, M.R. Palacín, *Electrochem. Commun.* 27 (2013) 85–88.
41. S. Guo, J. Liu, S. Qiu, W. Liu, Y. Wang, N. Wu, J. Guo, Z. Guo, *J. Mater. Chem. A* 3 (2015) 23895–23904.

42. T. Li, N. Lun, Y. Qi, C. Wei, Y. Sun, H. Zhu, J. Liu, Y. Bai, *J. Power Sources* 273 (2015) 472–478.
43. Y. Zhu, Y. Wen, X. Fan, T. Gao, F. Han, C. Luo, S.-C. Liou, C. Wang, *ACS Nano* 9 (2015) 3254–3264.
44. H. Liao, L. Xie, Y. Zhang, X. Qiu, S. Li, Z. Huang, H. Hou, X. Ji, *Electrochim. Acta* 219 (2016) 227–234.

Chapter 4 Towards enhanced sodium storage of anatase TiO_2 via a dual-modification approach of Mo doping combined with AlF_3 coating

4.1 Introduction

Downsizing TiO_2 to nanoscale, one typical solution, has been shown to be an effective strategy to prompt the capability for sodium storage thanks to the facilitated sodium diffusion resulting from the shortened transport pathways. It has also been demonstrated that the electrochemical performance of nanostructured TiO_2 materials could be remarkably enhanced especially at high charge/discharge current densities after doping with heteroatoms (e.g. Nb, Co, Mo, Fe, Sn, N, S, B, and F)[1–9] and/or compositing with high conductive materials (e.g. amorphous carbon, carbon nanotubes, carbon dots, graphene, and TiN).[10–17] Among the latter two approaches aiming at the amelioration of electron transfer, the doping method is more direct and appealing as it improves the low electronic conductivity and sodium diffusion kinetics of TiO_2, owing to the introduced structural defects. Nevertheless, it should be noted that the thermal stability of heteroatom doped TiO_2 might be declined by introducing heterogeneous defects of impurity.[18] The coating on the surface of cathode materials to improve the electrochemical performance as well as the thermal stability with metal fluoride (AlF_3) has been reported in LIBs.[19,20] It was suggested that AlF_3 coating could protect the cathode particles from direct contact with the electrolyte solution and reduce solid electrolyte interfacial side reactions. In light of the role of AlF_3 coating in LIBs and the fact that the study on dual modification of TiO_2 anode for NIBs is seldom reported to date, it is meaningful to explore the effects of AlF_3 coating on the sodium storage performance of TiO_2 doped with heteroatom.

In this chapter, we have investigated the effect of (i) Mo doping and (ii) dual modification of Mo doping combined with AlF_3 coating on the sodium storage

performance of anatase TiO_2. The Mo-doped anatase TiO_2 nanoparticles with uniform particle size were synthesized by a simple co-precipitation method firstly and then uniform AlF_3 layers were coated onto the Mo-doped anatase TiO_2 surface using a modified solid-state method. The electrochemical test results showed that the dually-modified TiO_2 sample could display significantly enhanced sodium storage performance compared with the pristine and single Mo-doped TiO_2, which can be attributed to the integrated beneficial effects of Mo doping and AlF_3 coating.

4.2 Experimental

Materials preparation

Mo-doped TiO_2 was synthesized by a simple co-precipitation method. In a typical procedure, 0.1366 g of $MoCl_5$ was dissolved in 15 mL of deionized water under magnetic stirring at room temperature. Later, a mixed solution containing 50 mL of ethanol and 3.4 mL of tetrabutyl titanate (TBT) was dropwise added into the $MoCl_5$ water solution under magnetic stirring followed by the addition of 2 mL ammonia solution (25wt%). The resulting precipitate mixture (with Mo/Ti molar percentage of 5%) was stirred vigorously for another 2 h before thoroughly drying at 110 ^oC for 12 h. Finally, the dried mixture was calcined in a furnace at 500 ^oC for 5 h in air to produce Mo-doped anatase TiO_2 nanoparticles (named as MTO hereafter). Bare TiO_2 was also prepared for comparison though the same process without adding $MoCl_5$ and denoted as TO.

To achieve AlF_3 coating on the surfaces of the as-prepared MTO particles, a modified solid-state method was used. Briefly, MTO powders and a certain amount of $Al(NO_3)_3 \cdot 9H_2O$ were mixed in deionized water by stirring, and then NH_4F aqueous solution was slowly added into the turbid liquid. The suspended mixture was constantly stirred at 80 ^oC until the solvent was completely evaporated. The obtained powders were then heated at 400 ^oC for 5 h to obtain AlF_3-coated MTO, which was assigned to MTO@AlF_3 (1wt% AlF_3 was adopted here).

Materials characterization

The prepared powder samples were characterized by XRD, Raman, TEM, EDS, and XPS. Details were introduced in Section 2.2.

Electrochemical tests

1.0 M of $NaClO_4$ in EC:PC=1:1 was used as electrolyte. Galvanostatic charge-discharge test, CV test, and EIS test were performed. Details were introduced in Section 2.3.

4.3 Results and discussion

4.3.1 Structure, morphology, and composition characterization

The crystal structures of the as-prepared TO and MTO were characterized by XRD, and patterns are shown in Figure 4.1a. For both samples, all the diffraction peaks can be indexed to the planes of anatase phase TiO_2 (JCPDS: 21-1272). Especially, for MTO, no additional peaks related to MoO_3 are detected. The diffusion of Mo into the TiO_2 lattice can be confirmed by the slight peak shift of the (101) and (200) reflections toward lower angles, as depicted in the insets of Figure 4.1a. From the calculated lattice constants shown in Table 4.1, it is noticed that the lattice parameters of MTO are slightly increased compared with those of TO. The minor increase in the lattice parameters along the *a*- and *c*- axes of MTO is in accordance with the above mentioned peak shift and can be ascribed to the fact that Mo^{6+} has successfully incorporated into the TiO_2 framework as the ionic radius of Mo^{6+} (0.062 nm) is slightly larger than that of Ti^{4+} (0.0605 nm).[4,21] In addition, by applying the Scherrer formula to the (101) peaks the average crystallite sizes of TO and MTO are estimated to be 18.3 and 15.9 nm, respectively. The XRD results show that Mo-doping could trigger lattice expansion and inhibit the crystal growth of TiO_2, in agreement with the previous reports on Mo^{6+}-doped TiO_2 synthesized by other methods including sol-gel method,[4] hydrothermal process,[21] and solvothermal method.[22] It has also been demonstrated,[4,21,22] that these doping effects of Mo may have improved the

electrochemical performance of TiO_2 thanks to enlarged diffusion pathways and enhanced conductivity.

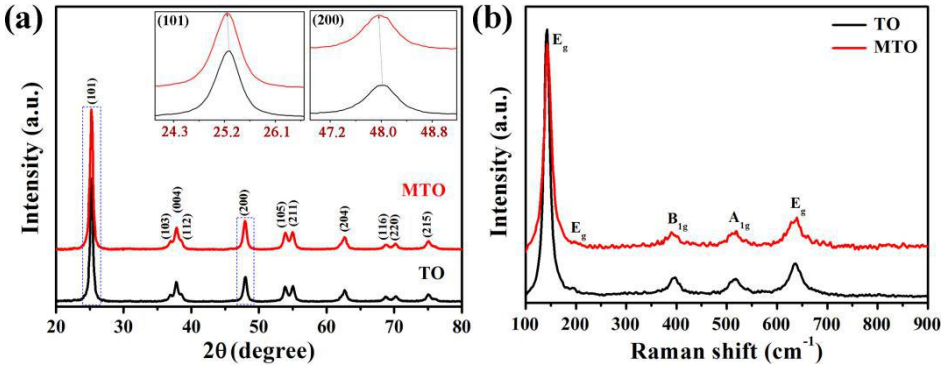

Figure 4.1 (a) XRD patterns of the as-prepared TO and MTO. The insets are the magnified view of peak (101) and (200). (b) Raman spectra for the TO and MTO samples.

Table 4.1 Calculated lattice parameters a, c and the cell volume (V) of the as-prepared TO and MTO samples.

Sample	TO	MTO
a (Å)	3.7844	3.7916
c (Å)	9.5494	9.5617
V (Å^3)	136.76	137.46

Raman spectra of TO and MTO are displayed in Figure 4.1b, from which five vibrational peaks at 143, 195, 395, 518, and 637 cm^{-1} for both samples can be identified, which are in good agreement with the typical bands of anatase TiO_2.[23] Moreover, no shift near 143 cm^{-1} (E_g) can be observed before and after Mo doping within the detect resolution of the apparatus. This implies that the crystal structure of anatase TiO_2 remains unchanged after the doping process,[4] consisting well with the above XRD results.

To investigate the chemical composition and state of TO and MTO, XPS analysis was performed and the spectra calibrated using the C 1s peak at 284.8 eV are exhibited in Figure 4.2. From the survey scan of XPS (Figure 4.2a), the peaks of Ti, O, and C can be seen for TO, while for MTO signal of Mo can also be detected with

obvious peaks located at around 230 and 400 eV, confirming the presence of Mo in MTO sample. The detailed information on the chemical state of Mo ion of MTO is clarified by the Mo 3d core level XPS spectrum (Figure 4.2b) showing two major peaks at 232.6 and 235.7 eV, which are attributed to Mo $3d_{5/2}$ and Mo $3d_{3/2}$, respectively. The Mo 3d core level spectrum of MTO confirms the Mo^{6+} oxidation state and thus the successful Mo doping in MTO.[4,21] From the Ti 2p core level XPS spectra (Figure 4.2c), it is seen that Mo-doping brings very limited change to the Ti 2p component, where for both TO and MTO the Ti $2p_{3/2}$ and Ti $2p_{1/2}$ peaks are located at 458.7 and 464.4 eV, respectively, with a gap of 5.7 eV, suggesting that Ti atoms exist mainly in the form of Ti^{4+} oxidation state in both TO and MTO samples.

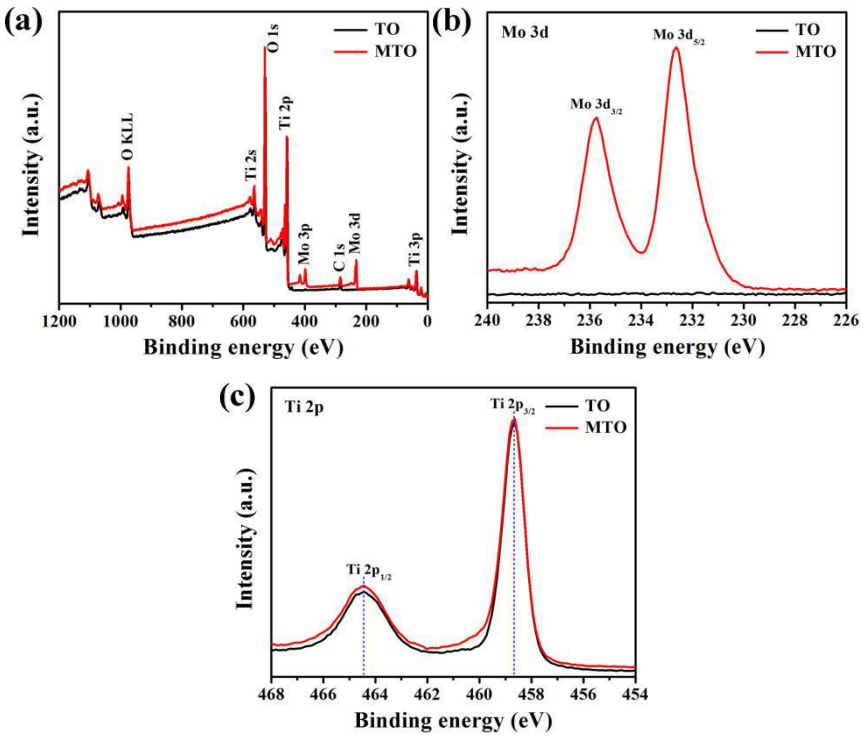

Figure 4.2 XPS spectra of TO and MTO: (a) wide survey, (b) Mo 3d, and (c) Ti 2p.

TEM was employed to analyze the morphologies of TO and MTO, as shown in Figure 4.3a and b, respectively. Both samples are composed of nanoparticles with visible agglomeration, however, TO reveals a non-uniform particle size distribution with individual size ranging from about 15 to 60 nm while MTO exhibits better homogeneousness in individual particle size of around 10−20 nm. Clearly, the Mo

doping could suppress TiO_2 grain aggregation and growth, which is beneficial to the sodiation. As mentioned before, we further coated AlF_3 onto the MTO surface by a modified solid-state method. The TEM image of the obtained MTO@AlF_3 sample is displayed in Figure 4.3c. It is observed that after AlF_3 coating, the morphology of MTO@AlF_3 retains the same as MTO but shows even less agglomeration. From the high resolution TEM (HRTEM) image of MTO@AlF_3 (Figure 4.3d), the TiO_2 grain is well crystallized with visible lattice fringes and its surface is coated with a very thin layer of AlF_3 (less than 1 nm, as denoted by arrows). The plane spacing of the TiO_2 nanoparticle (HRTEM image depicted in Figure 4.3e) is measured to be 0.36 nm, which corresponds to the (101) planes of anatase TiO_2. However, it is slightly increased relative to the standard *d*-spacing of (101) planes (0.35 nm) of anatase TiO_2, owing to the Mo doping into the lattice of anatase TiO_2. The corresponding fast Fourier transformation (FFT) displayed in Figure 4.3f shows that the reflection spots corresponding to the (011) planes are elongated (as marked by yellow circle). The reason causing this may be related to the existence of thin AlF_3 layer on the surface of TiO_2 crystal (as shown by the yellow dashed line surrounded area in Figure 4.3e). Therefore, the FFT result from another point of view implies that the TiO_2 surface indeed involves the ultrathin AlF_3 layer.

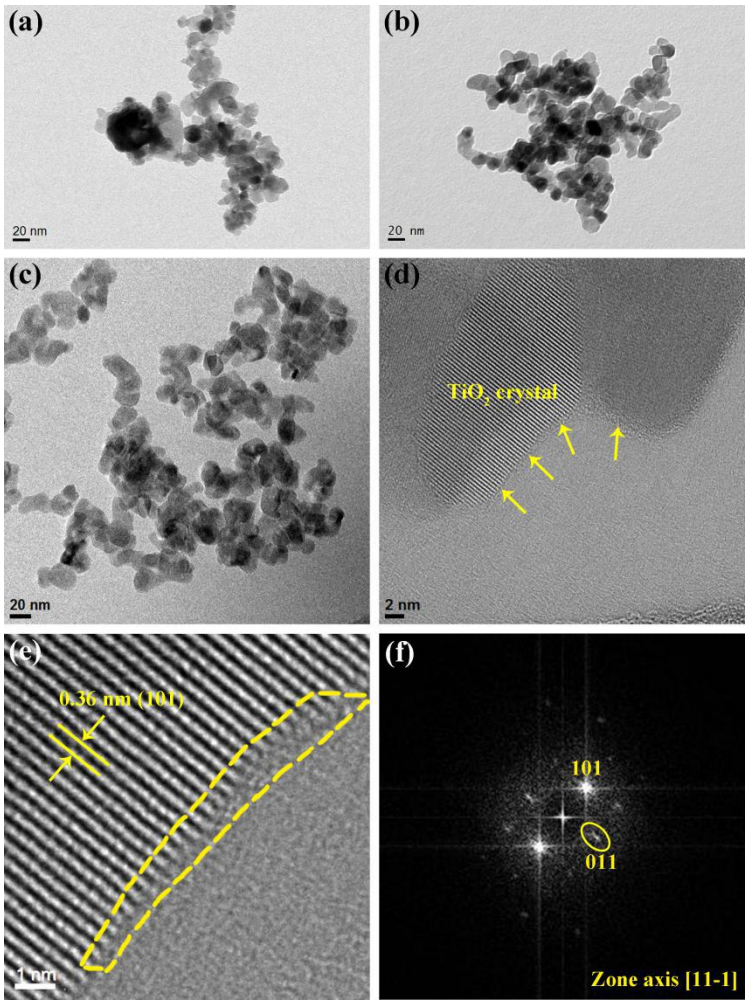

Figure 4.3 TEM images of (a) TO, (b) MTO, and (c) MTO@AlF_3. (d, e) HRTEM images and (f) FFT image of image (e) of MTO@AlF_3.

EDS mapping was also performed to characterize the dually-modified sample of MTO@AlF_3, as shown in Figure 4.4. The elemental maps highlight the uniform dispersion of Ti, O, Mo elements in the materials, indicative of the Mo doping in TiO_2. The elemental maps also reveal the existence and uniformity of AlF_3 coating on the TiO_2 particle surfaces which have been achieved by the facile two-step route. Based on the EDS analysis, the molar ratio of Mo:Ti is found to be approximately 1.97:32.56, giving a Mo/Ti molar percentage of about 6%, which is close to the designed value of 5%. It is also noted that the signal of F element (Figure 4.4f) is relatively weak compared to that of Al element (Figure 4.4e) when considering the stoichiometric ratio of F:Al is 3:1 for AlF_3. This is due to loss of fluorine species induced by a well-documented electron stimulated desorption process occurring under high-energy

electron irradiation in TEM.[24,25] The TEM and EDS results confirm the existence of AlF_3 coating layer on the surface of Mo-doped TiO_2 particles. In addition, from the XRD pattern of MTO@AlF_3 (Figure 4.5) it is seen that surface modification by AlF_3 does not change the crystal structure of the pristine material (MTO, Figure 4.1a).

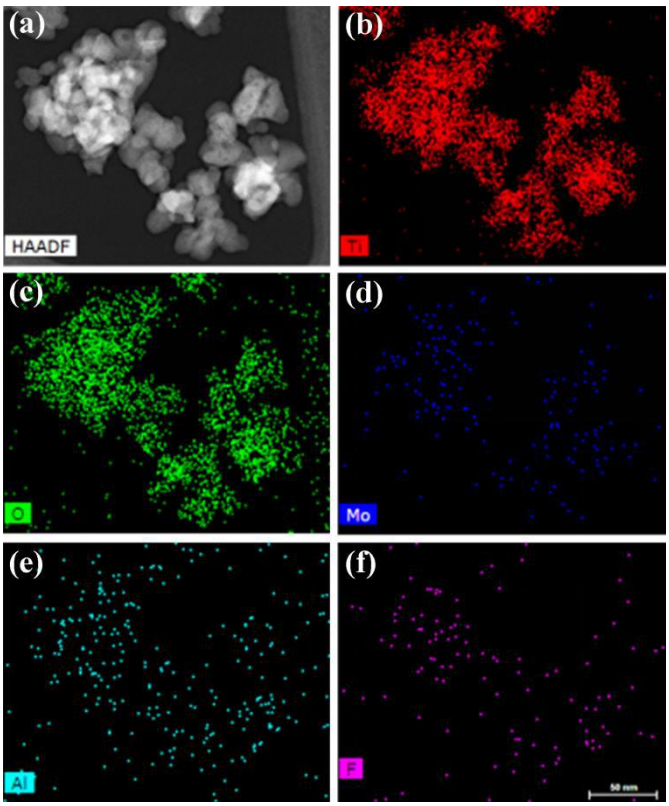

Figure 4.4 (a) HAADF-STEM image of MTO@AlF_3 and the corresponding EDS elemental mappings of (b) Ti, (c) O, (d) Mo, (e) Al, and (f) F.

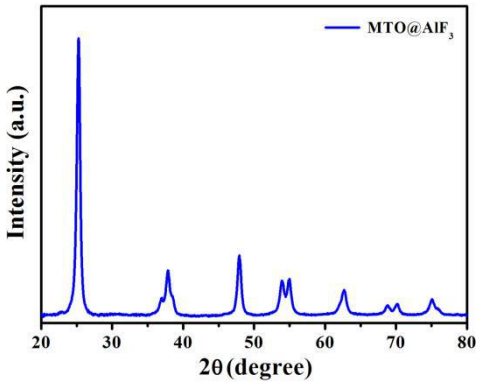

Figure 4.5 XRD pattern of the MTO@AlF_3 sample (with AlF_3 content of 1wt%).

4.3.2 Electrochemical properties for sodium storage

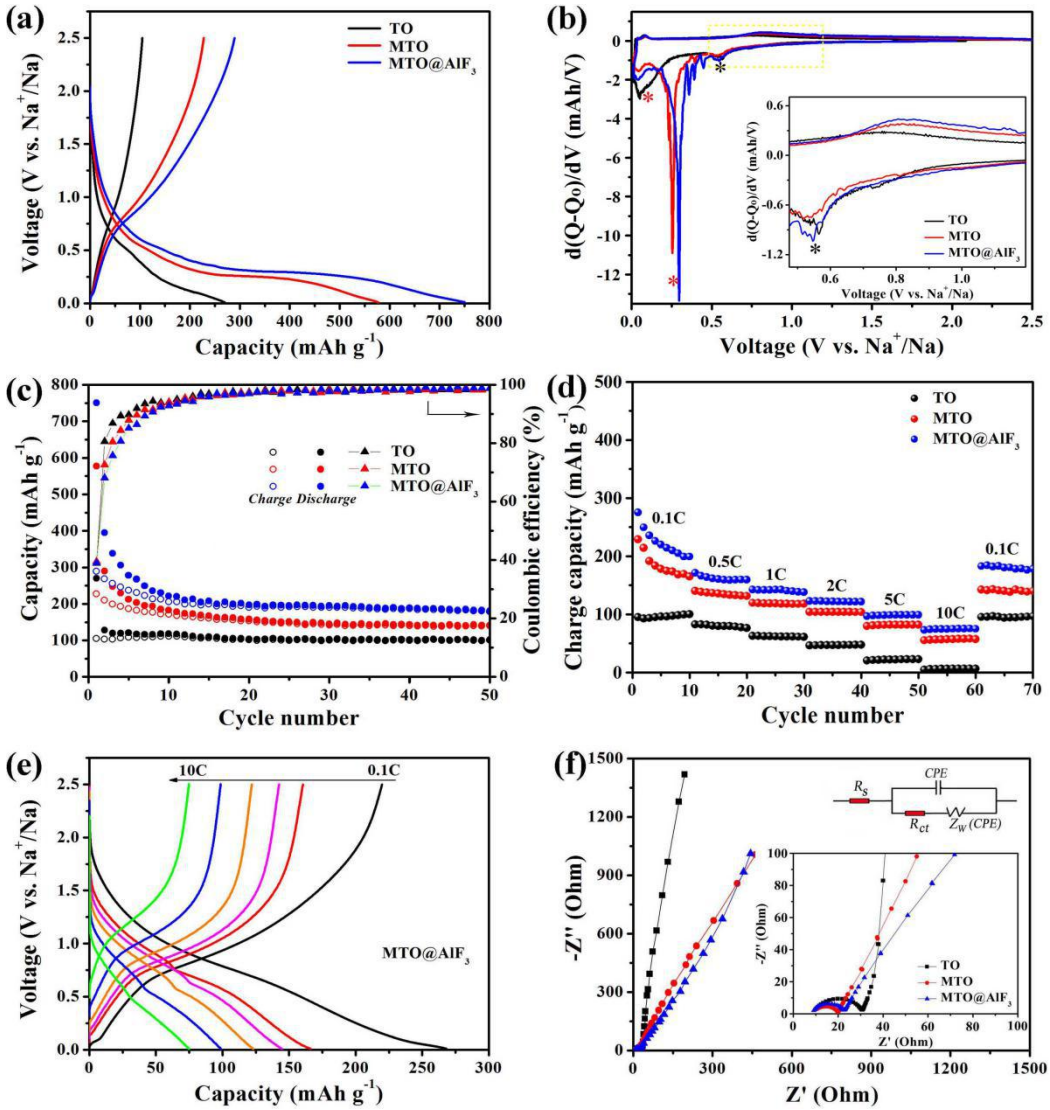

Figure 4.6 (a) First galvanostatic charge-discharge voltage curves at 0.1C between 0.01 and 2.5 V, (b) differential capacity (dQ/dV) vs. voltage plots reproduced from the first cycle charge-discharge curves at 0.1C (inset is the partial enlarged view), (c) cycling performance and Coulombic efficiency at 0.1C, and (d) rate capability at different current rates from 0.1C to 10C of TO, MTO, and MTO@AlF₃. (e) Charge-discharge profiles (of the fifth cycle) at various rates up to 10C of MTO@AlF₃. (f) EIS of TO, MTO, and MTO@AlF₃ before cycling. The insets in (f) are the enlarged view and the corresponding equivalent circuit.

Figure 4.6a depicts the first galvanostatic charge-discharge voltage curves of the pristine and modified TiO_2 samples at 0.1 C (1C= 335 mA g^{-1}) between 0.01 and 2.5 V. TO delivers a discharge capacity of 270 mAh g^{-1} and charge capacity of 105 mAh g^{-1}

at the first cycle with a Coulombic efficiency of 38.9%. In contrast, the first discharge/charge capacities are much higher of 577.4/227.7 mAh g^{-1} for MTO and 750.8/292.5 mAh g^{-1} for MTO@AlF_3, though both samples show a similar initial Coulombic efficiency (39.4% and 39.0%, respectively). Generally speaking, the irreversible capacity at the first cycle could be mainly ascribed to the irreversible insertion of Na^+ into TiO_2, to the decomposition of electrolyte, and to the formation of solid electrolyte interface (SEI) as well as to some other side reactions occur at the interfaces according to the previous reports.[4,8,11] Obviously, the TiO_2 sample of MTO which is modified by Mo doping displays much higher reversible capacity than that of bare TiO_2, and after coating MTO by AlF_3, the reversible capacity is further enhanced. Furthermore, it is noted that both MTO and MTO@AlF_3 display an obvious discharge plateau at about 0.25 V while is invisible for TO. The difference might be related to the easier and more Na^+ insertion into TiO_2 resulted from Mo doping, thus contributing to the larger first cycle discharge and charge capacities for MTO and MTO@AlF_3. The subsequent charge/discharge curves (2nd cycle, Figure 4.7a) feature a sloping profile and an average working voltage of about 0.8 V, which differs from the first discharge, indicating that an irreversible structural change occurs during the plateau region.

The differential capacity (dQ/dV) *vs.* voltage plots for the first cycle of the three samples were reproduced from the discharge/charge profiles, as provided in Figure 4.6b. During the discharge (sodiation) process, all the samples present a small cathodic peak around 0.55 V (indicated by black asterisk, it is more clear from the inset), which might be associated with the initial reaction of Na^+ insertion into anatase TiO_2 lattice and the resulting structural rearrangement and also with the formation of SEI layer,[26,27] though it is still not completely clarified. Upon further sodiation, for MTO and MTO@AlF_3, a stronger and evident cathodic peak at about 0.25 V (indicated by red asterisk) is observed and can be basically assigned to the irreversible phase transition,[26–28] in consistent with the obvious voltage plateau around 0.25 V in the first discharge process. However, for TO, the cathodic peak corresponding to the

irreversible phase transition occurs mainly at the voltage below 0.2 V and the peak intensity is relatively lower than those for MTO and MTO@AlF_3. During the charge (desodiation) process, a broad anodic peak at about 0.8 V which corresponds to the typical Na^+ de-insertion from the sodiated Na_xTiO_2 phase can be seen for all the three samples. Upon cycling, the intense cathodic peak below 0.3 V caused by the irreversible phase transition disappears and a pair of cathodic/anodic peaks at 0.75/0.8 V based on the reversible Ti^{4+}/Ti^{3+} redox couple can be detected (Figure 4.7b). Moreover, it appears noteworthy that the intensity of the cathodic/anodic peaks for MTO and especially MTO@AlF_3 are higher than that for TO, which suggests the high electrochemical reaction activity of TiO_2 due to the improved kinetics after Mo doping and AlF_3 coating.

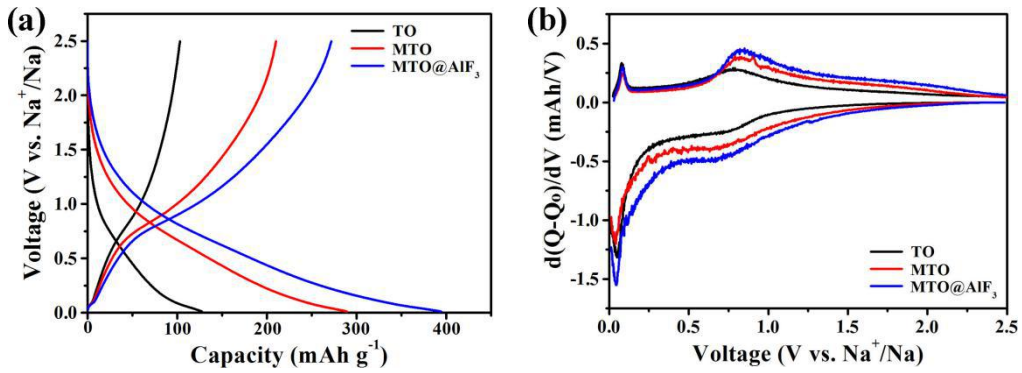

Figure 4.7 (a) Galvanostatic charge-discharge voltage curves for the 2nd cycle at 0.1C between 0.01 and 2.5 V, (b) the corresponding differential capacity (dQ/dV) vs. voltage plots of TO, MTO, and MTO@AlF_3.

Cycling performance of TO, MTO, and MTO@AlF_3 at 0.1 C are obtained and compared, as shown in Figure 4.6c. Obviously, the modified samples display higher capacity upon cycling thought it decays in the initial few cycles. The Coulombic efficiency of the three samples for the first cycle is lower than 40% but it rises significantly to value about 90% in the 7th cycle, and reaches a high value above 98% from the 25th cycle and maintains an overall stability thereafter. After 50 cycles, MTO could deliver a charge (reversible) capacity of 139.8 mAh g^{-1}, which is higher than that of TO (100.7 mAh g^{-1}). A much higher reversible capacity of 178.9 mAh g^{-1} can be achieved after 50 cycles for MTO@AlF_3 after dual modification. Besides,

MTO@AlF_3 also exhibits superior rate capabilities (Figure 4.6d) with the reversible capacity of 141 mAh g^{-1} at 1 C and 98.4 mAh g^{-1} at a high rate of 5 C. MTO exhibits reversible capacities of 118.5 mAh g^{-1} and 81.6 mAh g^{-1} at 1 C and 5 C, respectively. In contrast, TO delivers a much lower reversible capacity of 61.9 mAh g^{-1} at 1 C and only 22 mAh g^{-1} at 5 C. These results indicate that the sodium storage performance of TO could be improved by Mo doping and further enhanced via dual modification of Mo doping combined with AlF_3 coating. Figure 4.6e displays the charge/discharge profiles of MTO@AlF_3 at various rates, from which it can be seen that increasing the current density results in a decrease in the capacity due to the increased polarization, however, even at a very high rate of 10 C charge/discharge plateaus can be observed and it could still deliver a reversible capacity of 74.7 mAh g^{-1}, revealing an excellent rate capability of MTO@AlF_3.

It has been reported that Mo doping could improve the electronic and ionic conductivities of TiO_2,[4,21,22] hence the enhanced sodium storage performance shown above. To understand the role of Mo doping, EIS of TO, MTO, and MTO@AlF_3 before cycling were collected (Figure 4.6f). All the Nyquist plots display similar shapes (clear from the enlarged view) showing an intercept at the Z′ axis at high frequency which indicates the ohmic resistance (R_s), a depressed semicircle in the high-to-medium frequency region which corresponds to the charge transfer resistance (R_{ct}), and an inclined line in the low-frequency region which stands for the Warburg impedance (Z_w) related to the solid-state Na^+ diffusion in the bulk of the electrode.[4,26] The impedance spectra could be fitted well based on a proposed equivalent circuit model (inset in Figure 4.6f), where constant phase elements (CPE) replace the pure capacitance and the Warburg component for a better fitting of the impedance data. All the samples show similar R_s, but the Mo-doped samples show much lower R_{ct} (10.5 Ω for MTO, 13.4 Ω for MTO@AlF_3) than that of TO (21 Ω), indicating the effectively improved electronic conductivity of TiO_2 due to Mo doping. Noted that the R_{ct} value for MTO@AlF_3 is slightly increased compared to MTO because of the insulating characteristic of AlF_3 coating,[25] nevertheless, it is still obvious lower than that of TO.

The Na^+ diffusion coefficient D ($cm^2\ s^{-1}$) can be calculated from the inclined lines in the Warburg region by using the following equation:

$$D = R^2T^2/2A^2n^4F^4C^2\sigma^2$$

where R, T, A, n, F, C, and σ is the gas constant, the absolute temperature, the surface area of the electrode (1.76 cm^2), the number of electrons transferred per molecule during the reaction, the Faraday constant (96485 C mol^{-1}), the concentration of Na^+ (10^{-3} mol cm^{-3}), and the Warburg factor, respectively. The value of σ (154.9 for TO, 109.2 for MTO, 111.7 for MTO@AlF_3) can be obtained from the slop of the line Z'–$\omega^{-1/2}$ (not shown here). The Na^+ diffusion coefficient D is calculated to be 1.54 × 10^{-11} $cm^2\ s^{-1}$ for MTO, 1.47 × 10^{-11} $cm^2\ s^{-1}$ for MTO@AlF_3, which are both about two times higher than that for TO (7.63 × 10^{-12} $cm^2\ s^{-1}$), indicating that the Mo doping could also facilitate Na^+ diffusion in TiO_2. In addition, it is found that the potentially resistive thin AlF_3 coating only brings imperceptible effect on the Na^+ diffusion which can be neglected.

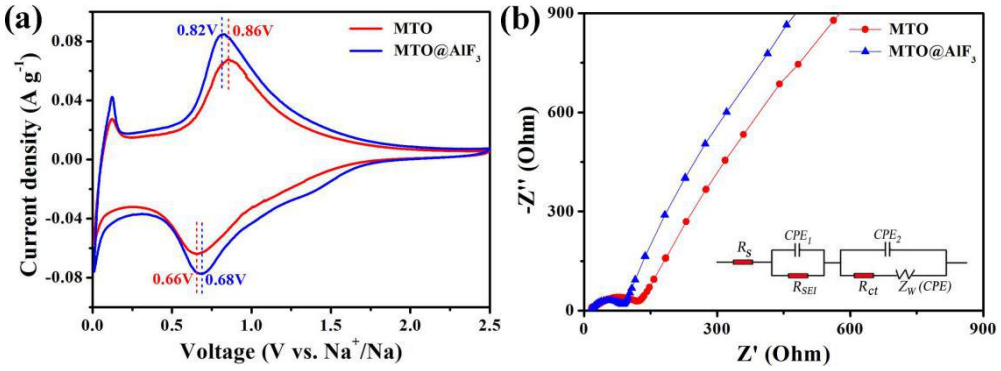

Figure 4.8 (a) CV curves at a scan rate of 0.1 mV s^{-1} in the voltage range of 0.01−2.5 V (vs. Na^+/Na) and (b) EIS of MTO and MTO@AlF_3 after 50 cycles at the rate of 0.1C. The inset in (b) is the corresponding equivalent circuit.

To better reveal the role of AlF_3 coating in enhancing the sodium storage performance of MTO, CV tests at a scan rate of 0.1 mV s^{-1} in the voltage range of 0.01−2.5 V (*vs.* Na^+/Na) for MTO and MTO@AlF_3 after 50 cycles at the rate of 0.1 C were performed. From the CV curves shown in Figure 4.8a, it is seen that both samples display a pair of vigorous and broad redox peaks centered at about 0.7/0.8 V corresponding to the sodium insertion/de-insertion of TiO_2, which is in line with the

discharge/charge curves and dQ/dV plots after the first cycle (Figure 4.7), demonstrating the high electrochemical reaction activity and reversibility of TiO_2 after the irreversible phase transition occurs in the first discharge process. However, some differences between MTO and MTO@AlF_3 are still noted: (i) the voltage difference between the redox peaks (ΔV) is 0.2 V for MTO while 0.14 for MTO@AlF_3; (ii) the peak current of MTO@AlF_3 is much higher than that of MTO. These obvious differences reveal the positive effects of AlF_3 coating to improve the electrochemical reactivity, to lower polarization, and to ensure good reversibility of TiO_2 in cycling. Furthermore, the EIS of the two samples after 50 cycles was also conducted, as displayed in Figure 4.8b**.** The so-called depressed semicircles are composed of a blurry arc related to the impedance from the formed SEI (R_{SEI}) and a second arc associated with the impedance of the charge transfer (R_{ct}). Obviously, the diameter of the semicircle of MTO@AlF_3 is smaller than that of MTO, which indicates a smaller interface resistance ($R_{int} = R_{SEI} + R_{ct}$) of MTO@$AlF_3$, confirming that AlF_3 surface coating could effectively reduce the solid electrolyte interfacial resistance and enhance the electrochemical reactivity at the surface/interface region. According to the proposed equivalent circuit model (inset in Figure 4.8b), the fitted R_{int} value is 102.8 Ω for MTO and 70.6 Ω for MTO@AlF_3. Based on the above CV and EIS results the AlF_3 coating indeed plays an important role in enhancing the sodium storage performance of MTO. Thus, combined with the beneficial effects of Mo doping, the dually modified TiO_2 sample could exhibit significantly enhanced sodium storage performance comparing with the pristine and single Mo-doped TiO_2. The content of AlF_3 in the AlF_3-coated MTO sample should be taken into consideration: in this work a moderate content like 1wt% was adopted, when 3wt% was used the dually modified TiO_2 sample displays much inferior performance with a reversible capacity of only 99 mAh g^{-1} after 50 cycles at 0.1 C (Figure 4.9).

The capacity fading in the first few cycles and low initial Coulombic efficiency (Figure 4.6c) are issues need to be improved in future studies. The possible solutions might be from the optimization in electrolytes and binder which are also important

factors that could have impacts on the electrochemical performance of the TiO_2 electrode in Na-ion cells.

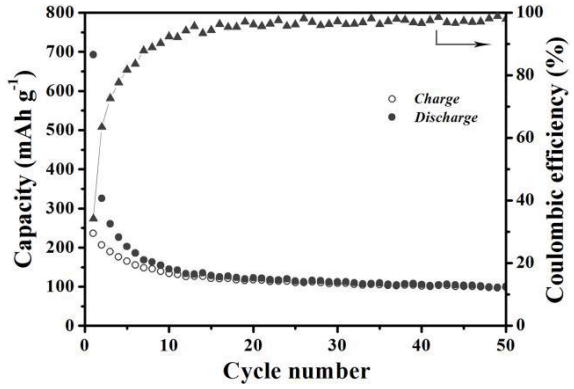

Figure 4.9 Cycling performance of 3wt%-AlF_3 coated MTO sample at 0.1C.

4.4 Conclusions

Mo-doped anatase TiO_2 was successfully synthesized via a simple co-precipitation method. Further modification by AlF_3 coating was achieved by solid-state method. When utilized as anode materials for NIBs, the single Mo-doped TiO_2 exhibits better sodium storage performance than the pristine one, which can be mainly attributed to the improved electronic/ionic conductivity resulted from Mo doping. Especially, through a dual-modification strategy of Mo doping combined with AlF_3 coating, the electrochemical performance of TiO_2 can be further enhanced owing to the positive impacts of AlF_3 surface coating of effectively reduced solid electrolyte interfacial resistance, enhanced electrochemical reactivity at the surface/interface region, and lower polarization during cycling. The remarkable performance achieved (a high reversible capacity of 178.9 mAh g^{-1} at 0.1 C after 50 cycles and excellent rate capabilities up to 10 C) using a cost-effective fabrication approach render the dually-modified anatase TiO_2 a promising anode material for high-performance NIBs. Moreover, the study in this work suggests that AlF_3 coating is effective to enhance the sodium storage capability and the dual-modification approach is indeed more desirable compared to the single one to design advanced NIBs electrode materials.

4.5 References

1. F. Zhao, B. Wang, Y. Tang, H. Ge, Z. Huang, H.K. Liu, *J. Mater. Chem. A* 3 (2015) 22969–22974.
2. D. Yan, C. Yu, Y. Bai, W. Zhang, T. Chen, B. Hu, Z. Sun, L. Pan, *Chem. Commun.* 51 (2015) 8261–8264.
3. Y. Lai, W. Liu, J. Li, K. Zhang, F. Qin, M. Wang, J. Fang, *J. Alloys Compd.* 666 (2016) 254–261.
4. H. Liao, L. Xie, Y. Zhang, X. Qiu, S. Li, Z. Huang, H. Hou, X. Ji, *Electrochim. Acta* 219 (2016) 227–234.
5. Z. Hong, M. Kang, X. Chen, K. Zhou, Z. Huang, M. Wei, *ACS Appl. Mater. Interfaces* 9 (2017) 32071–32079.
6. Y. Yang, X. Ji, M. Jing, H. Hou, Y. Zhu, L. Fang, X. Yang, Q. Chen, C.E. Banks, *J. Mater. Chem. A* 3 (2015) 5648–5655.
7. H. Zhang, Y. Jiang, Z. Qi, X. Zhong, Y. Yu, *Energy Storage Mater.* 12 (2018) 37–43.
8. J. Ni, S. Fu, C. Wu, J. Maier, Y. Yu, L. Li, *Adv. Mater.* 28 (2016) 2259–2265.
9. B. Wang, F. Zhao, G. Du, S. Porter, Y. Liu, P. Zhang, Z. Cheng, H.K. Liu, Z. Huang, *ACS Appl. Mater. Interfaces* 8 (2016) 16009–16015.
10. J.-Y. Hwang, S.-T. Myung, J.-H. Lee, A. Abouimrane, I. Belharouak, Y.-K. Sun, *Nano Energy* 16 (2015) 218–226.
11. M.N. Tahir, B. Oschmann, D. Buchholz, X. Dou, I. Lieberwirth, M. Panthöfer, W. Tremel, R. Zentel, S. Passerini, *Adv. Energy Mater.* 6 (2016), 1501489.
12. S. Qiu, L. Xiao, X. Ai, H. Yang, Y. Cao, *ACS Appl. Mater. Interfaces* 9 (2016) 345–353.
13. N. Wang, Y. Gao, Y.X. Wang, K. Liu, W. Lai, Y. Hu, Y. Zhao, S.L. Chou, L. Jiang, *Adv. Sci.* 3 (2016) 1600013.
14. Y.-N. Li, J. Su, X.-Y. Lv, Y.-F. Long, Y.-X. Wen, *Electrochim.Acta* 182 (2015) 596–603.
15. X. Zhu, Q. Li, Y. Fang, X. Liu, L. Xiao, X. Ai, H. Yang, Y. Cao, *Part. Part. Syst. Charact.* 33 (2016) 545–552.
16. A. Shoaib, Y. Huang, J. Liu, J. Liu, M. Xu, Z. Wang, R. Chen, J. Zhang, F. Wu, *J. Power Sources* 342 (2017) 405–413.
17. X. Ma, J.-L. Tian, F. Zhao, J. Yang, B.-F. Wang, *Ionics* 24 (2018) 3771–3779.
18. J. Chen, Z. Ding, C. Wang, H. Hou, Y. Zhang, C. Wang, G. Zou, X. Ji, *ACS Appl. Mater. Interfaces* 8 (2016) 9142–9151.
19. Y.K. Sun, M.J. Lee, C.S. Yoon, J. Hassoun, K. Amine, B. Scrosati, *Adv. Mater.* 24 (2012) 1192–1196.
20. X. Ke, Z. Zhao, J. Liu, Z. Shi, Y. Li, L. Zhang, H. Zhang, Y. Chen, Z. Guo, Q. Wu,

Appl. Energy 194 (2017) 540–548.

21. J. Zhang, T. Huang, L. Zhang, A. Yu, *J. Phys. Chem. C* 118 (2014) 25300–25309.
22. T.V. Thi, A.K. Rai, J. Gim, S. Kim, J. Kim, *J. Alloys Compd.* 598 (2014) 16–22.
23. R. Baddour-Hadjean, J.-P. Pereira-Ramos, *Chem. Rev.* 110 (2009) 1278–1319.
24. L. Vergara, R. Vidal, J. Ferron, *Appl. Surf. Sci.* 229 (2004) 301–310.
25. G. Ruano, J. Moreno-López, M. Passeggi Jr, R. Vidal, J. Ferrón, M. Niño, R. Miranda, J. De Miguel, *Surf. Sci.* 606 (2012) 573–579.
26. L. Ling, Y. Bai, Z. Wang, Q. Ni, G. Chen, Z. Zhou, C. Wu, *ACS Appl. Mater. Interfaces* 10 (2018) 5560–5568.
27. L. Wu, D. Bresser, D. Buchholz, G.A. Giffin, C.R. Castro, A. Ochel, S. Passerini, *Adv. Energy Mater.* 5 (2015) 1401142.
28. W. Li, M. Fukunishi, B.J. Morgan, O.J. Borkiewicz, K.W. Chapman, V. Pralong, A. Maignan, O.I. Lebedev, J. Ma, H. Groult, *Chem. Mater.* 29 (2017) 1836–1844.

Chapter 5 Na-ion diffusivity and mechanical instability in Sn anodes

5.1 Introduction

NIBs are being considered as replacements for LIBs especially for stationary applications, where the high volumetric and gravimetric energy density of the energy source is not as important as in the automotive and electronic sectors. Stable anodes, however, have not been developed to date, and there exist few candidates, namely Sn, Sb, P, and treated forms of carbon. Among these materials, Sn provides a very promising theoretical capacity of 847 mAh g^{-1} upon the formation of $Na_{15}Sn_4$.[1] This capacity, however, cannot be retained during continuous cycling. For example, in the case of microscale Sn particles, a 67% irreversible capacity loss occurs during the first discharge cycle,[2] which has been associated with the 420% volume expansion that occurs upon the formation of Na-Sn alloys. Aiming at mitigating this phenomenon, focus has been given on the fabrication of nanoscale Sn as deformation and fracture are less severe at this scale. In this regard, different kinds of nanostructures, including Sn/C nanocomposites[2–11] and M−Sn intermetallics (M = Cu, Ni, Fe),[12–15] have been investigated, however, a capacity over 500 mAh g^{-1} for at least 100 cycles was rarely reported. The few exceptions are Sn nanofiber anodes, which gave a charge capacity of 776 mAh g^{-1} at a rate of 0.1 C after 100 cycles,[8] and Sn nanodots encapsulated in porous nitrogen-doped carbon nanofibers (Sn NDs@PNC) which allowed for a reversible capacity of 511 mAh g^{-1} at 2000 mA g^{-1} for over 500 cycles.[11]

Of particular interest is the case of Sn/C "pomegranate-like" nanostructured anodes,[4] which gave an initial charge capacity of 503.6 mAh g^{-1}, with a capacity decay over 50% after 100 cycles, when cycled against Na. The same anodes allowed for a 88.5% capacity retention (627.9 mAh g^{-1}) for 1500 cycles when cycled against Li. This comparison suggests that, although Sn also experiences a volume expansion upon lithiation (~ 300%), there exist significant differences in the response of Sn

between the insertion of Li-ions *vs.* Na-ions. This is further supported by studies which examine the effects of Li-ion and Na-ion insertion into microstructures. For example, in the case of Li-insertion, the Sn particle size in porous electrodes must be below 50 nm to avoid fracture during electrochemical cycling,[16] however, *in situ* TEM indicated that for the case of Na-ion insertion, Sn particles that were even ~ 100 nm in diameter did not show any kind of fracture.[1] An *ex situ* study performed for porous electrodes, which employed Sn/C nanocomposites as the active material, also concluded that after twenty cycles against Na-metal, the Sn particles did not experience fracture.[2] The authors attributed this to the small Sn crystal size, which was measured with XRD to be ~ 90 nm.[2] More recent experiments using *in situ* hard X-ray nanotomography on Sn porous anodes illustrated fractures in micron-sized Sn particles but could not detect cracks in Sn particles that were below 500 nm.[17]

The aforementioned differences between sodiation and lithiation of Sn can be interpreted by considering the mechanical behaviour of Na-Sn *vs.* Li-Sn. First principle calculations have shown that the moduli of Sn decrease upon the formation of both Na- and Li- rich alloys.[18,19] Despite this consistent softening in elastic constants the type of fracture (brittle *vs.* ductile) is approximated by examining the ratio of the bulk modulus with the shear modulus (B/G). Larger values of B/G indicate a more brittle-like behaviour, and based on the density functional calculations it was reported that Li-Sn alloys are more brittle than Na-Sn alloys.[18,19] Furthermore, examination of the phase diagrams for Li−Sn[20] and Na−Sn[21] reveals that the melting points of Na−Sn compounds are substantially lower than the Li−Sn analogues. Therefore, based on the above considerations, a ductile response may be more active upon sodiation of Sn than during its lithiation.

The purpose of the present work is hence to reveal the damage mechanisms that occur during sodiation/desodiation of Sn anodes. To do so a 0.5 mm thick planar Sn sheet is employed as the anode, since theoretical models and experiments have shown that planar geometries are more prone to mechanical instabilities during ion-insertion.

[22–25] In addition, this configuration allows to dispense with binder and carbon additives required in the fabrication of porous electrodes, and captures directly the response of Sn to sodiation. Furthermore, the planar geometry will experience a relatively simple state of stress produced by the one-dimensional gradient in concentration, which allows for a relatively simple estimation of the diffusion coefficient of Na-ions in Sn. Finally, it should be emphasized that the resulting capacities for the examined anodes are significantly low because of the planar geometry of the electrode which is a non-issue in the present work given the objective was to unveil the mechanical damage in Sn and not present a competitive anode for NIBs.

5.2 Experimental

Materials and Electrochemical tests

Sn foil (0.5 mm thick) with a purity of 99.998% was purchased from Sigma-Aldrich. The Sn foil was placed in the MBraun glovebox filled with Ar and was sectioned into 10×10 mm squares, which were used as the active electrodes directly without using Al or Cu foil as the current collector. CR2032 coin-type Na−Sn half cells were assembled in the glovebox. The electrolyte solution used was 1.0 M $NaClO_4$ in PC. Galvanostatic charge-discharge test and CV test were conducted over the voltage range of 0.05−2.0 V (*vs.* Na^+/Na). EIS was also performed.

Materials characterization

SEM images of the Sn electrode were obtained before and after 5 cycles. The Na−Sn half-cell was disassembled in the Ar-filled glovebox and the Sn electrode was washed with PC and then dried at 70 ^oC for 3 h to perform SEM after cycling. It was then placed in a vial and transferred to the SEM chamber.

5.3 Results and discussion

5.3.1 Electrochemical properties for sodium storage

Figure 5.1a shows the initial galvanostatic discharge curve at current of 200 μA and 800 μA. For both currents, the Sn electrode exhibits a long sloping plateau below 0.2 V, which can be ascribed to a series of Na-Sn alloying reactions and finally to the formation of $Na_{15}Sn_4$ upon complete sodiation. It should be noted that the capacity measurements are not per gram as the aim of this study is to probe the deformation mechanisms that occur during the sodiation/desodiation, not the anode performance. The discharge capacity at the current of 200 μA is much larger than that of 800 μA, demonstrating that a deeper sodiation process occurred in the Sn electrode at a relatively low current. Figure 5.1b depicts the galvanostatic charge-disharge curves at the current of 800 μA for five cycles. In the charge profiles, the Sn electrode exhibits two distinct potential plateaus at around 0.32 and 0.57 V, which are characteristic of stepwise dealloying of $Na_{15}Sn_4$. The large irreversible capacity loss occurring during the first cycle, is associated with the formation of the solid electrolyte interface (SEI) layer as well as to the degradation that Sn experiences due to Na-insertion; this will be further elaborated with SEM images in the next section. The Na−Sn half-cell was also tested under different currents from 800 to 2400 μA, as shown in Figure 5.1c. It can be seen that increasing the current resulted in a decrease in the capacity of the Sn electrode, due to the increased polarization. The long sloping discharge plateau below 0.2 V is observed even at a high current of 2000 μA, however, only a short slope without an obvious plateau is seen when the cell was discharged−charged at a higher current of 2400 μA.

Previous studies suggest that during the sodiation process of Sn, four distinguishable plateaus form in a galvanostatic electrochemical profile, corresponding to four different phases.[26–31] However, for each plateau, with the exception of $Na_{15}Sn_4$, there are significant debates about the mechanisms giving rise to the alloy formation and their composition and no conclusive results have been

reached yet. In this respect, it is very meaningful to investigate Sn anode foil for sodium batteries.

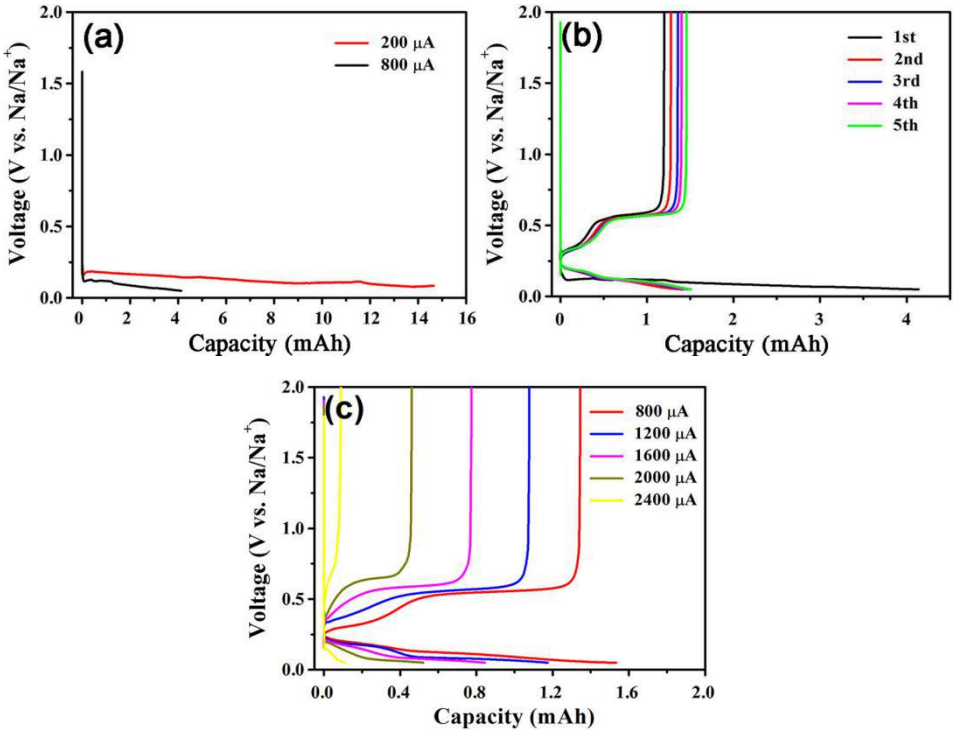

Figure 5.1 Electrochemical tests of the Na−Sn half cells. (a) Initial galvanostatic discharge curves at the current of 200 μA and 800 μA; (b) Galvanostatic charge-discharge curves at the current of 800 μA for 5 cycles; (c) Galvanostatic charge-discharge curves at different currents from 800 to 2400 μA.

The electrochemical reactivity of pure Sn was also evaluated by CV, as depicted in Figure 5.2a. During the first cathodic sweep, there is a small reduction peak at 0.2 V and then an intense cathodic current appears at potentials below 0.18 V, corresponding to the Na−Sn alloying process and the formation of highly sodiated phases, *i.e.* Na_9Sn_4 and $Na_{15}Sn_4$. Furthermore, a cathodic peak at a high potential of 1.1 V during subsequent cathodic scans with increasing intensity and potential shifts can be ascribed to the electrolyte decomposition or SEI layer formation. Similar observations have been reported for Sn thick foil and electrodeposited Sn thin-film electrodes for LIBs[32–34] and indicate that the electrolyte reduction processes were not suppressed by the surface film formed on the Sn-foil electrode. The above characteristics of the CV curves can be interpreted by the volume changes that occur

during the Na^+ insertion and de-insertion in the Sn, and will be discussed in the next section where SEM images illustrate the surface morphology throughout cycling. In the anodic scans, three well-defined anodic peaks can be identified at about 0.27, 0.62 and 0.69 V, corresponding to desodiation from $Na_{15}Sn_4$, NaSn and $NaSn_5$, respectively. These desodiation potentials are in good agreement with the calculated and experimental results of Sn anodes reported previously.[6,35,36] However, it should be noted that precise comparison with data in the literature cannot be performed as Sn thick sheets electrodes have not been cycled before.

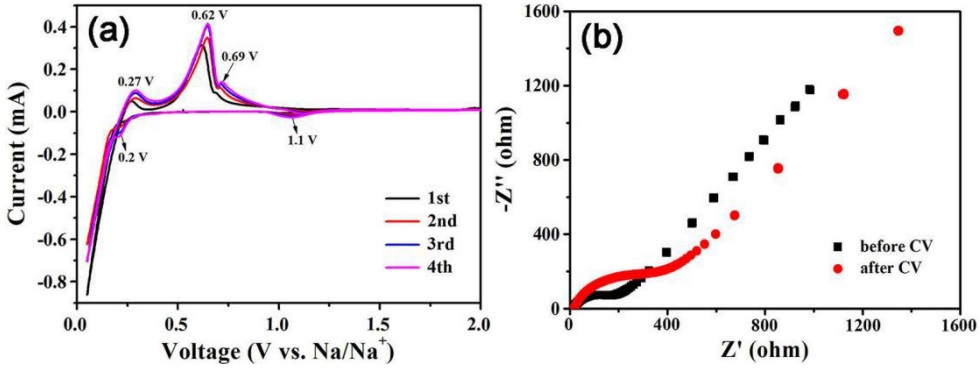

Figure 5.2 (a) CV profiles of the first four cycles at the scan rate of 0.1 mV s^{-1} in the range of 0.05−2.0 V vs. Na^+/Na; (b) EIS of the Na−Sn half-cell before and after the CV test for four cycles.

Finally, EIS of the Na-Sn half-cell before and after the CV test was also performed to study the detailed reaction kinetics. As shown in Figure 5.2b, the Nyquist plots exhibit one depressed semicircle in the high−medium frequency region followed by a sloping line in the low frequency region. The depressed semicircle at high frequencies is associated with two overlapped interface impedances *i.e.*, SEI film and charge transfer impedance (R_{SEI} and R_{ct}, respectively), while the inclined line corresponds to the sodium diffusion within the bulk of the electrode material.[9] The Sn electrode shows a much larger semicircle after four CV cycles, indicating an increase in the interface resistance. The SEI formation observed was more pronounced (and thick) in this anode than in "porous" anodes studied previously.

5.3.2 Morphological degradation of Sn during sodiation

Ex situ SEM images were taken before and after cycling of the Sn to interpret the capacity fade observed in the galvanostatic charge-discharge cycling of Sn foil. From Figure 5.3a and b, it can be seen that fresh Sn foil is composed of many coarse grains and the surface is relatively flat with some tiny grooves. In Figure 5.3c and d the Sn surface that was in contact with the electrolyte is shown after 5 cycles. A severe mechanical deformation is exhibited, which can be distinguished into two types: (i) Dry lake-bed fracture, close to Si and SiSn films during lithiation/delithiation,[24,25] which took place throughout the anode; (ii) Sn whiskers (as indicated by representative red arrows) and fine particles formed on the Sn electrode (Figure 5.3d).

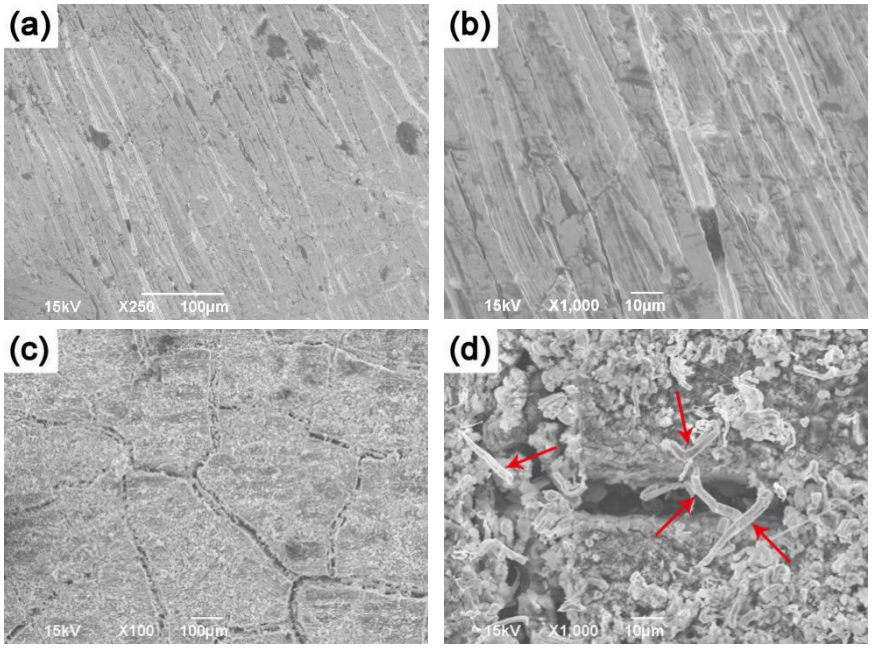

Figure 5.3 SEM images of surface morphology of the Sn electrode. (a, b) Sn surface before cycling. (c, d) Sn surface in contact with the electrolyte after 5 cycles, indicating crack formation. The red arrows in (d) indicate the whisker formation on the fractured particles.

To verify that the whiskers were composed of Sn, electron dispersive spectroscopy (EDS) was performed on numerous whiskers as those depicted in Figure 5.3d. A representative EDS spectrum on a whisker is shown in Figure 5.4 illustrating that Sn was the dominant element present, while Na, C and O were also present at a

low concentration, since electrochemical cycling had taken place.

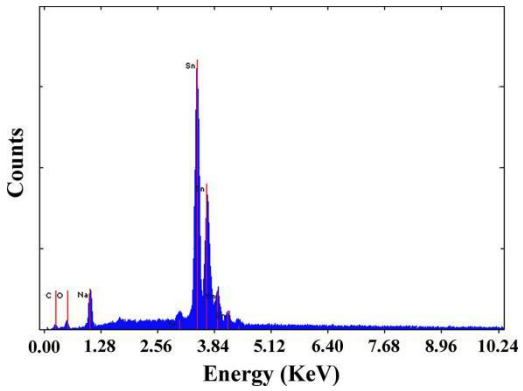

Figure 5.4 EDS spectrum on a whisker that is depicted in Figure 5.3d.

Whisker formation has not been observed for micro and nanoscale Sn particles in porous electrodes,[1,2,16,17] however, it most likely occurred here since the mechanically-induced stresses caused by Na^+ insertion/de-insertion, were accentuated due to the small surface area and large thickness of the Sn anode foil. Although whisker formation has not been observed for Sn films during sodiation, there has been one example reporting it for 500 nm Sn films cycled against Li-metal.[37] However, the authors of that study[37] did not performed EDS measurements to verify that those were Sn whiskers and not fibers from the separator. Whisker formation as a damage mechanism in Sn induces the concern that they could penetrate through the separator and short-circuit the electrochemical cell. Further studies must therefore be performed, examining whisker formation, for porous Sn-based anodes for NIBs.

To better capture the damage evolution within the Sn foil due to Na-insertion/extraction, focused ion beam (FIB) was employed to cut a cross section of the surface shown in Figure 5.3d so as to take a side view, depicted in Figure 5.5. The darker region on the top of Figure 5.5a is the SEI layer, while the lighter shaded area is the Sn. Figure 5.5a and b reveal that a characteristic effect of Na-insertion is pore formation as both large and small pores were observed throughout the cross section. The larger pores were closer to the SEI layer – up to a depth of 3 μm, whereas the smaller pores formed deeper into the Sn. This can be due to the fact that sodiation,

and hence volume expansions, were more pronounced on the upper surface of the Sn where Na^+ insertion occurred. No pores were observed after a critical depth of approximately ~ 8–10 µm. Figure 5.5c depicts an EDS spectrum taken from the darker grey region of Figure 5.5a verifying it is SEI as it is comprised by Na, C, and O, in addition to a small amount of Sn. Figure 5.5d is a representative EDS spectrum from inside the pores within the Sn, suggesting that Na is present, as well as traces of O and C. Not all Na-ions could not be fully deinserted.

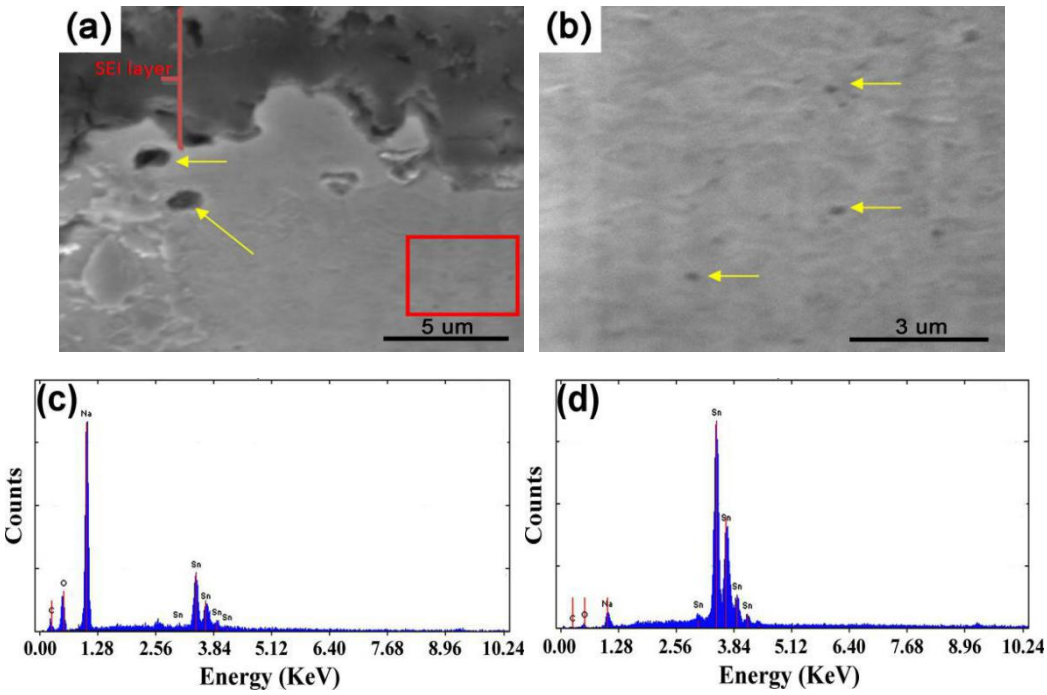

Figure 5.5 Cross section view obtained with FIB of the Sn surface in contact with the electrolyte. (a) SEI layer appears as dark grey. Micropores are present in the Sn, some of which are indicated by arrows. (b) Magnification of red square from (a). Multiple nanopores are present some of which are indicated with arrows. The maximum distance at which these pores were observed was ~ 8–10 µm beneath the interface with the SEI. (c) Representative EDS spectrum from SEI layer of (a). (d) Representative EDS spectrum from within the pores in the Sn.

The severe damage mechanisms and thick SEI layer observed in the Sn foil anode are responsible for the high capacity loss observed in the first cycle shown in Figure 5.1b, as well as the increase in resistance in the impedance measurements of Figure 5.2b. Furthermore, the SEI layer was not stable enough to buffer the ~ 420% volume changes of Sn upon further cycling. Therefore, continuous cycling resulted in

fracture of the SEI, exposing fresh Sn surface to the electrolyte, which resulted in additional SEI to form. Hence, a thick SEI layer developed.[32–34]

The pore formation observed here has not been referenced before in respect to sodiation of Sn. However, a closer examination (through magnification) of the SEM images presented in a previous study of Sn microparticles after cycling with respect to Na,[2] does indeed reveal the formation of nanopores on the surface of Sn particles which was not noted by the authors. Hence, pore formation does exist at the nanoscale level, but it is less pronounced and has not been highlighted prior to this study.

5.3.3 Na^+ diffusion coefficient calculation

As no experimental values exist for the diffusion coefficient D of Na^+ in Sn (D_{Na}), an estimate of D_{Na} is given herein by analysing the CV response run at different scan rates. The CV curves at varied scan rates are presented in Figure 5.6, from which it is interestingly found that with increasing the scan rate from 0.05 to 0.25 mV s^{-1} the intensity of the anodic peak at 0.62 (Peak 1) decreases slowly while the intensity of the peak at 0.69 V (Peak 2) increases slowly. Both of these two peaks exhibit a gradual shift of the peak position toward a higher potential due to the increased polarization as the scan rate increased. It is also noted that the cathodic peak at 1.1 V, corresponding to electrolyte decomposition or SEI formation, became more pronounced with a shift to a potential close to 1 V when increasing the scan rate to values larger than 0.15 mV s^{-1}, confirming again the changes in the electrode surface morphology as well as the instability of the SEI. The above changes in the peaks observed in CV can be attributed to the severe damage mechanisms discussed before. Moreover, the decrease in intensity of Peak 1 and the increase in intensity of Peak 2 upon increasing the scan rate may be related to different properties of various $NaSn_x$ phases, although the exact reason is presently unknown. From the above CV results it is also evident that the sodiation and desodiation reactions in the present Sn foil anode are diffusion controlled.

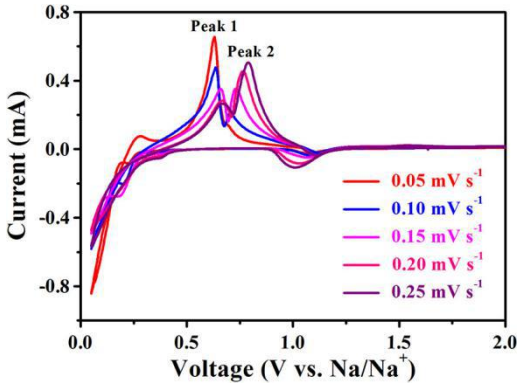

Figure 5.6 CV profiles at different scan rates in the range of 0.05−2.0 V vs. Na^+/Na.

An estimate of D_{Na} was obtained from the CV response run at 0.1 mV s^{-1} of the anodic peak at 0.62 V (as shown in Fiure 5.2a) using the Randles-Sevick equation[38]:

$$i_p = 0.4463\ nFAC(nFvD/RT)^{1/2} = (2.69\times10^5)n^{3/2}AD^{1/2}Cv^{1/2}$$

where i_p is the peak current (A), n is the number of electrons transferred (which is one for Na), F is Faraday constant (96485 C mol^{-1}), A is the electrode surface area (here the geometric area of the electrode is 1.0 cm^2), C is the bulk concentration of Na in the Sn electrode (0.06 mol cm^{-3}), v is the potential scan rate (V s^{-1}), D is the diffusion coefficient of Na^+ (cm^2 s^{-1}), R is the gas constant (8.314 J mol^{-1} K^{-1}), and T is the absolute temperature (298.15 K). The D_{Na} was calculated as 6.45×10^{-12} cm^2 s^{-1}.

The time it takes for the Na-ions to diffuse out of the Sn was calculated by measuring the time required to desodiate the Sn foil during the charge process at the fourth cycle in the CV. This time was t = 6566.4 s. By using this time and the diffusion coefficient (6.45×10^{-12} cm^2 s^{-1}) in the Einstein approximation equation: $t = X^2/(2D)$, it was found the distance X was 2.97 μm. This means that assuming the sodiation process is completely reversible the maximum depth of the Na-ions penetration into the Sn foil anode is ~ 3 μm. This is consistent with the maximum depth in the Sn sheet that we observe the large pore formation induced by Na-insertion/extraction in Figure 5.5a.

However, Na-ion insertion was not fully reversible, and some Na-ions remained in the Sn after each cycle, as the EDS spectra revealed. Hence during each

charge-discharge process the Na-ions that remained in the Sn penetrated further into the Sn, beyond the 3 μm limit. As fewer Na-ions take part into the irreversible reaction they induced less damage, indicated by nanopores, up to depths of ~ 8–10 μm into the Sn surface, as seen in Figure 5.5a. It can therefore be said that the calculated value of the diffusion coefficient correctly predicts the Na-ion penetration into the Sn.

Even though an experimental value of D_{Na} in Sn has not been reported in literature previously, experimental studies have measured the diffusion coefficient of Li^+ (D_{Li}) in Sn thin films to be in the range between 10^{-16} and 10^{-14} cm^2 s^{-1}.[39] Furthermore, a more recent atomistic study concluded that $D_{Li} < D_{Na}$,[30] hence the value obtained herein of $D_{Na} = 6.45\times10^{-12}$ cm^2 s^{-1} is consistent with existing aforementioned results reported in literature.

5.4 Conclusions

This study revealed three main damage mechanisms resulting from the sodiation of Sn foil: dry lake-bed fracture, pore formation and whisker nucleation. This is a unique result, as no other studies have reported the formation of pores and whiskers during sodiation. As the geometry of the present anodes was planar, and the thickness of the Sn film in the mm scale, the damaging effects of sodiation were significantly pronounced. The Sn whiskers can penetrate the separator and short-circuit the electrochemical cell, thus may be a safety concern for NIBs and should be further examined in porous electrodes that use Sn as the active material. Nanopore formation has not been highlighted before as a damage mechanism during sodiation and may explain the capacity fade observed in nanostructured Sn particles in porous electrodes that do not display fracture. Furthermore, the planar geometry of the present Sn anodes allowed a first estimate to be obtained for the diffusion coefficient of Na^+ in Sn as 6.45×10^{-12} cm^2 s^{-1}.

5.5 References

1. J.W. Wang, X.H. Liu, S.X. Mao, J.Y. Huang, *Nano Lett.* 12 (2012) 5897–5902.
2. M.K. Datta, R. Epur, P. Saha, K. Kadakia, S.K. Park, P.N. Kumta, *J. Power Sources* 225 (2013) 316–322.
3. W. Chen, D. Deng*, Carbon* 87 (2015) 70–77.
4. Y. Liang, H. Tian, J. Repac, S.-C. Liou, J. Chen, W. Han, C. Wang, S. Ehrman, *Energy Storage Mater.* 13 (2018) 8–18.
5. H. Ying, S. Zhang, Z. Meng, Z. Sun, W.-Q. Han, *J. Mater. Chem. A* 5 (2017) 8334–8342.
6. Y. Liu, N. Zhang, L. Jiao, Z. Tao, J. Chen, *Adv. Funct. Mater.* 25 (2015) 214–220.
7. Y. Liu, Y. Xu, Y. Zhu, J.N. Culver, C.A. Lundgren, K. Xu, C. Wang, *ACS Nano* 7 (2013) 3627–3634.
8. D.-H. Nam, T.-H. Kim, K.-S. Hong, H.-S. Kwon, *ACS Nano* 8 (2014) 11824–11835.
9. X. Xie, K. Kretschmer, J. Zhang, B. Sun, D. Su, G. Wang, *Nano Energy* 13 (2015) 208–217.
10. B. Ruan, H.-P. Guo, Y. Hou, Q. Liu, Y. Deng, G. Chen, S.-L. Chou, H.-K. Liu, J.-Z. Wang, *ACS Appl. Mater. Interfaces* 9 (2017) 37682–37693.
11. Y. Liu, N. Zhang, L. Jiao, J. Chen, *Adv. Mater.* 27 (2015) 6702-6707.
12. Y.-M. Lin, P.R. Abel, A. Gupta, J.B. Goodenough, A. Heller, C.B. Mullins, *ACS Appl. Mater. Interfaces* 5 (2013) 8273–8277.
13. I.T. Kim, E. Allcorn, A. Manthiram, *J. Power Sources* 281 (2015) 11–17.
14. J. Liu, Y. Wen, P.A. van Aken, J. Maier, Y. Yu, *Nano Lett.* 14 (2014) 6387–6392.
15. E. Edison, R. Satish, W.C. Ling, N. Bucher, V. Aravindan, S. Madhavi, *J. Power Sources* 343 (2017) 296–302.
16. K.E. Aifantis, T. Huang, S.A. Hackney, T. Sarakonsri, A. Yu, *J. Power Sources* 197 (2012) 246–252.
17. J. Wang, C. Eng, Y.K. Chen-Wiegart, J. Wang, *Nat. Commun.* 6 (2015) 7496.
18. M. Mortazavi, J. Deng, V.B. Shenoy, N.V. Medhekar, *J. Power Sources* 225 (2013) 207–214.
19. Y. Qi, L.G. Hector, C. James, K.J. Kim, *J. Electrochem. Soc.* 161 (2014) F3010–F3018.
20. J. Sangster, C. Bale, *J. Phase Equilib.* 19 (1998) 70–75.
21. B. Predel, Na-Sn (Sodium-Tin), in: Li-Mg–Nd-Zr, Springer, 1997, pp. 1–4.
22. K. Aifantis, S. Hackney, *J. Power Sources* 196 (2011) 2122–2127.
23. K. Aifantis, J. Dempsey, *J. Power Sources* 143 (2005) 203–211.
24. L. Beaulieu, K. Eberman, R. Turner, L. Krause, J. Dahn, *Electrochem. Solid-State*

Lett. 4 (2001) A137–A140.

25. Y. Wang, Y. He, R. Xiao, H. Li, K. Aifantis, X. Huang, *J. Power Sources* 202 (2012) 236–245.
26. L.D. Ellis, T.D. Hatchard, M.N. Obrovac, *J. Electrochem. Soc.* 159 (2012) A1801–A1805.
27. L. Baggetto, P. Ganesh, R.P. Meisner, R.R. Unocic, J.-C. Jumas, C.A. Bridges, G.M. Veith, *J. Power Sources* 234 (2013) 48–59.
28. D.-H. Nam, K.-S. Hong, S.-J. Lim, T.-H. Kim, H.-S. Kwon, *J. Phys. Chem. C* 118 (2014) 20086–20093.
29. L. Baggetto, C.A. Bridges, J.-C. Jumas, D.R. Mullins, K.J. Carroll, R.A. Meisner, E.J. Crumlin, X. Liu, W. Yang, G.M. Veith, *J. Mater. Chem. A* 2 (2014) 18959–18973.
30. C.-Y. Chou, M. Lee, G.S. Hwang, *J. Phys. Chem. C* 119 (2015) 14843–14850.
31. J.M. Stratford, M. Mayo, P.K. Allan, O. Pecher, O.J. Borkiewicz, K.M. Wiaderek, K.W. Chapman, C.J. Pickard, A.J. Morris, C.P. Grey, *J. Am. Chem. Soc.* 139 (2017) 7273–7286.
32. J.-T. Li, S.-R. Chen, X.-Y. Fan, L. Huang, S.-G. Sun, *Langmuir* 23 (2007) 13174–13180.
33. I.T. Lucas, E. Pollak, R. Kostecki, *Electrochem. Commun.* 11 (2009) 2157–2160.
34. M. Inaba, T. Uno, A. Tasaka, *J.Power Sources* 146 (2005) 473–477.
35. V. Chevrier, G. Ceder, *J. Electrochem. Soc.* 158 (2011) A1011–A1014.
36. Y. Xu, Y. Zhu, Y. Liu, C. Wang, *Adv. Energy Mater*. 3 (2013) 128–133.
37. J. Li, F. Yang, J. Ye, Y.-T. Cheng, *J. Power Sources* 196 (2011) 1474–1477.
38. H.-G. Jung, J. Hassoun, J.-B. Park, Y.-K. Sun, B. Scrosati, *Nat. Chem*. 4 (2012) 579.
39. J. Xie, N. Imanishi, A. Hirano, Y. Takeda, O. Yamamoto, X. Zhao, G. Cao, *Solid State Ionics* 181 (2010) 1611–1615.

Chapter 6 Facile synthesis of highly graphitized carbon via reaction of CaC_2 with sulfur and its application for lithium and sodium ion batteries

6.1 Introduction

Designing and preparing new carbon materials has long been of interest in the field of materials science and engineering. Various carbon materials with unique structures and morphology have been found to be useful for a variety of applications owing to their outstanding chemical and physical properties.[1–3] Extracting metals or metalloids from carbides using halogens, supercritical water, selective oxidation or vacuum decomposition has been demonstrated to be effective for synthesizing large family of carbon materials ranging from amorphous carbon to graphite, carbon nanotubes and graphene, and thus-obtained carbon is termed as carbide-derived carbon (CDC).[2,4] The CDC structures have found numerous applications especially in lithium-ion batteries (LIBs), supercapacitors (SCs), gas storage, catalysis, biomedical engineering, tribology and as membranes.[2] Particularly, porous CDC obtained by chlorination has been widely studied for SCs application because of the high specific surface area and tunable pore size with a narrow size distribution.[5–10] For example, Kou *et al.*[5] prepared Mo_2C-derived chlorine-doped ordered mesoporous carbon with few-layered graphene walls and investigated its performance as electrode material for SCs and LIBs. The Cl-doped porous CDC showed promising potential for electrochemical energy storage with a high charge capacity of 733 mAh g^{-1} at the current rate of 0.5 A g^{-1} after 100 cycles and a high specific capacitance of 250 F g^{-1} at 0.5 A g^{-1} in 1 M H_2SO_4 solution. However, most of the available reports on CDC exploit their potential in SCs owing to the high specific surface area while few studies are related to the use of CDC in LIBs.[2–4]

Among various metal carbides, calcium carbide (CaC_2) is a commercially

available alkaline earth metal carbide with low cost and serves as an ideal alkynyl source for synthesizing carbon materials. Besides chlorine treatment of CaC_2 to produce CDC,[11–13] various other methods have been proposed including thermo-reaction of CaC_2 using reactants like halogenated hydrocarbon,[14,15] oxalic acid,[16] $AlCl_3 \cdot 6H_2O$,[17] $CuCl_2 \cdot 2H_2O$,[18] $MgCl_2$,[19] NaCl,[20] and CO_2[21] and electrochemistry technique through anodic oxidation of CaC_2 dissolved in a LiCl–KCl–$CaCl_2$ melt.[22] The CaC_2-derived carbon nano-onions[18] and carbon nanosheets[21] have also been studied for LIBs application, which displayed a good cyclic performance with a reversible capacity of 391 mAh g^{-1} after 60 cycles at 37.2 mA g^{-1} and a high capacity of 494 mAh g^{-1} after 200 cycles at 100 mA g^{-1} as well as a good rate performance. These investigations demonstrate the potential of CaC_2-derived graphitized carbon (GC) as anode candidates for rechargeable LIBs. In this respect, we consider of significant importance to develop new, efficient and low cost techniques to fabricate carbon materials starting from CaC_2 as carbon source.

In this work we report, for the first time, a new one-step approach to prepare highly graphitized carbon (HGC) from CaC_2 by the thermo-reaction with sulfur at 550 °C. The structure and morphology of the CaC_2-derived HGC were characterized in detail by various techniques, and the electrochemical performance was investigated for application in rechargeable LIBs and further for sodium-ion batteries (NIBs).

6.2 Experimental

Materials preparation

In a typical procedure, the raw materials of 3.2 g chemically pure sublimated sulfur and 6.4 g industrial CaC_2 powder (corresponding to a molar ratio of 1:1) were mixed and put into a stainless steel autoclave of 30 mL in capacity. As a reactor, the tightly sealed autoclave was heated in an electric oven to 550 °C and maintained for 5 h. When the autoclave was naturally cooled to ambient temperature, the solid product in the autoclave was collected and washed consecutively with dilute hydrochloric acid

and deionized water until all soluble materials were removed. After drying at 100 °C for 12 h in an oven, black powder was ultimately obtained.

Materials characterization

The prepared powder sample was characterized by XRD, SEM, EDS, Raman, TEM, XPS, and Nitrogen adsorption−desorption isotherms. Details were introduced in Section 2.2.

Electrochemical tests

In the Li half-cells used for tests, the electrolyte was 1.0 M $LiPF_6$ in EC:DMC=1:1. In the Na half-cells used for tests, the electrolyte was 1.0 M of $NaClO_4$ in EC:PC=1:1. Galvanostatic charge-discharge tests at varied current densities in the voltage range from 0.01 to 1.5 V (*vs.* Li^+/Li or Na^+/Na) were performed. Details were introduced in Section 2.3.

6.3 Results and discussion

6.3.1 Structure, morphology, and composition characterization

The carbon formation achieved by selectively etching calcium from CaC_2 using sulfur can be expressed as: $CaC_2 + S = CaS + 2C$. The Gibbs free energy of the reaction at 550 °C is $\Delta_r G_m^\Theta = -374.5$ kJ mol^{-1}, suggesting the occurring of a spontaneous reaction. Furthermore, the enthalpy evaluation returns a strong negative value of $\Delta_r H_m^\Theta = -433.2$ kJ mol^{-1}, implying that the reaction of CaC_2 with sulfur is thermodynamically advantageous. Indeed, owing to this negative enthalpy value, the reaction will tend to release heat which will facilitate the proper completion of the reaction itself. At the end of the reaction the final carbon product can be easily retrieved by removing the CaS byproduct through washing with dilute hydrochloric acid and deionized water. The XRD pattern of the resulting product is shown in Figure 6.1a. The sharp diffraction peak around $2\theta = 26.4°$ is attributable to the (002) reflection of hexagonal graphite (JCPDS no. 41-1487), confirming the formation of carbon with high

graphitization degree. Calculated by the Bragg's law, the interplanar spacing of (002) reflection is 0.337 nm, which is similar to graphite. The weak reflections at 42.3, 44.4 and 54.5° result from the (100), (101) and (004) planes of hexagonal graphite, respectively, whereas the two remaining diffraction peaks around 35° and 60° are ascribed to SiC (JCPDS no. 49-1428) which cannot be removed by acid washing.

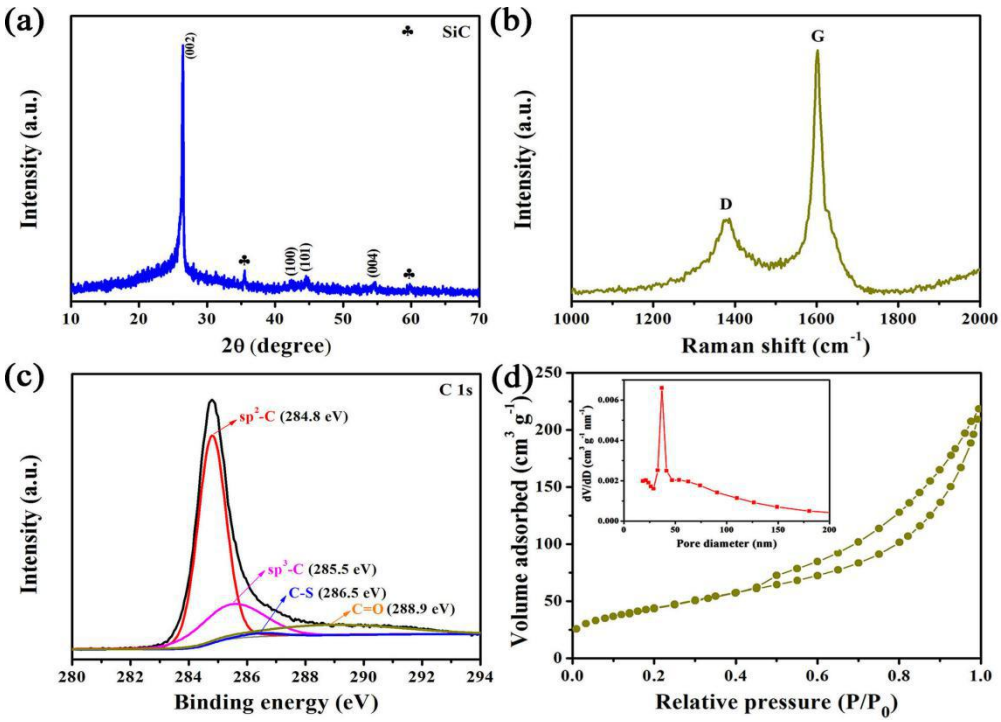

Figure 6.1 (a) XRD pattern, (b) Raman spectrum, (c) high-resolution XPS spectrum of C 1s, and (d) N_2 adsorption−desorption isotherms of the resulting product obtained by the reaction of CaC_2 and sulfur at 550 °C for 5 h. The inset in (d) is the pore-size distribution.

The structure of the as-prepared carbon was identified by Raman spectroscopy (Figure 6.1b). The peak at about 1380 cm^{-1} (*D*-band) is associated with the defects and disordered structures of carbonaceous solids, while the peak around 1600 cm^{-1} (*G*-band) is ascribed to the stretching modes of C–C bond of typical graphite.[14–16] The intensity of the *G*-band (I_G) is much higher than *D*-band (I_D) with an I_G/I_D value of 3.2, suggesting that the as-prepared carbon is of high graphitization degree,[14,21] consistent with the XRD result.

The structure of the highly graphitized carbon (HGC) was further investigated by XPS (Figure 6.1c). High-resolution XPS spectrum of C 1s is deconvoluted into four peaks centered at 284.8, 285.5, 286.5 and 288.9 eV, attributed to sp^2-C, sp^3-C, C–S and C=O, respectively.[5,15,21–23] The predominant sp^2-C peak is indicative of the high graphitization degree of the carbon product. The presence of the C−S peak demonstrates slight S-doping in the carbon. The bonding information between carbon and sulfur is further revealed in the high-resolution S 2p spectrum (Figure 6.2), where the two peaks centered at 164.2 (S $2p_{3/2}$) and 165.4 eV (S $2p_{1/2}$) with an intensity ratio of 2:1 and binding energy difference of 1.2 eV correspond to spin-orbital splitting of thiophene-like sulfur incorporated into graphite.[24] The sulfur doping is preferential in polarizing electron pairs, improving the graphitization degree of carbon and introducing redox reactions due to the large size and high chemical activity.[24] As evidenced both theoretically and experimentally,[24–26] heteroatom doping could improve the electrical properties and chemical activity of carbon, thus is favorable for energy storage capability.

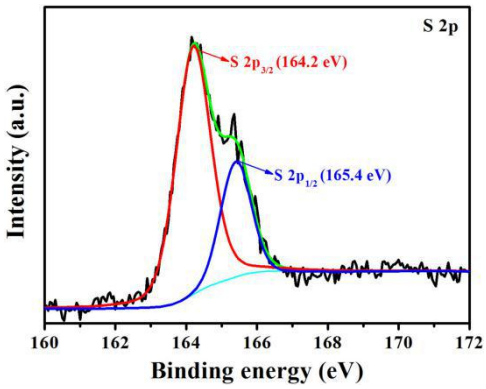

Figure 6.2 High-resolution S 2p XPS spectrum of the as-prepared HGC product.

In addition, the specific surface area of HGC was evaluated by N_2 adsorption−desorption isotherms (Figure 6.1d). The product exhibits typical IVa isotherms with an H3 type hysteresis loop at a relative pressure of 0.4−1.0, indicative of the presence of meso- and macro-pores in the carbon framework.[27,28] The specific surface area and pore volume are 159.5 $m^2\ g^{-1}$ and 0.34 $cm^3\ g^{-1}$, respectively. From

the pore-size distribution curve (the inset in Figure 6.1d), the mesopores are primarily 21 and 39 nm in size and the macropores are larger than 50 nm. These pores, formed during the removal of CaS from the reaction product, are conducive to improving the electrolyte permeability, increasing the electrode/electrolyte contact interface and facilitating Li-ion transportation.[29,30]

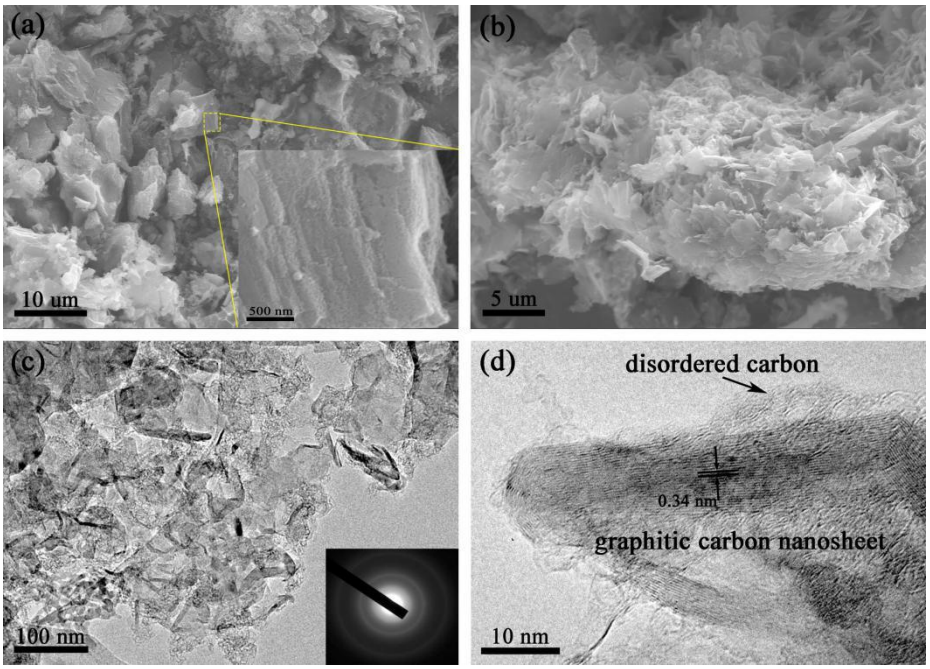

Figure 6.3 (a, b) SEM images, (c) Low-magnification TEM and (d) HRTEM images of the HGC. The inset in (a) is the high-magnification SEM image of carbon framework, and that in inset in (c) is the corresponding SAED pattern.

SEM and TEM were employed to examine the morphology and microstructure of the HGC. From the SEM image (Figure 6.3a), the product consists mainly of 3D fluffy carbon of about 4–20 μm in size with uneven surface, which is in fact composed of thin carbon sheets with a lateral size of about 1–10 μm (Figure 6.3b). From the high-magnification SEM image in the inset of Figure 6.3a, the carbon framework displays layered structure with plentiful mesopores. According to the EDS spectrum of HGC (Figure 6.4b), the carbon content accounts for about 86.26 wt% (91.76% in atomic percent) and the S-doping content is about 5.80 wt% (2.31% in atomic percent). The other elements of O (7.05 wt%), Si (0.12 wt%) and Ca (0.77 wt%) stem from the strong adsorption of CO_2 and H_2O on the porous HGC and the

impurities in CaC_2. The elemental mappings for C and S (Figure 6.4a) indicate the uniform distribution of sulfur throughout the product, further confirming the S-doping in the HGC. The TEM image of the carbon sheets and the corresponding SAED pattern are shown in Figure 6.3c, while the distinct diffraction rings in the inset confirm the high graphitization of carbon. From the HRTEM image of single carbon sheet (Figure 6.3d), the planar spacing is about 0.34 nm, matching well with graphite. Moreover, some disordered carbon could also be observed on the surface of the graphitized nanosheet. As a consequence, the HGC including 3D frameworks and 2D nanosheets reveals long-range ordered rearrangement of carbon atoms occurring during the selective thermo-chemical etching of CaC_2 by sulfur.

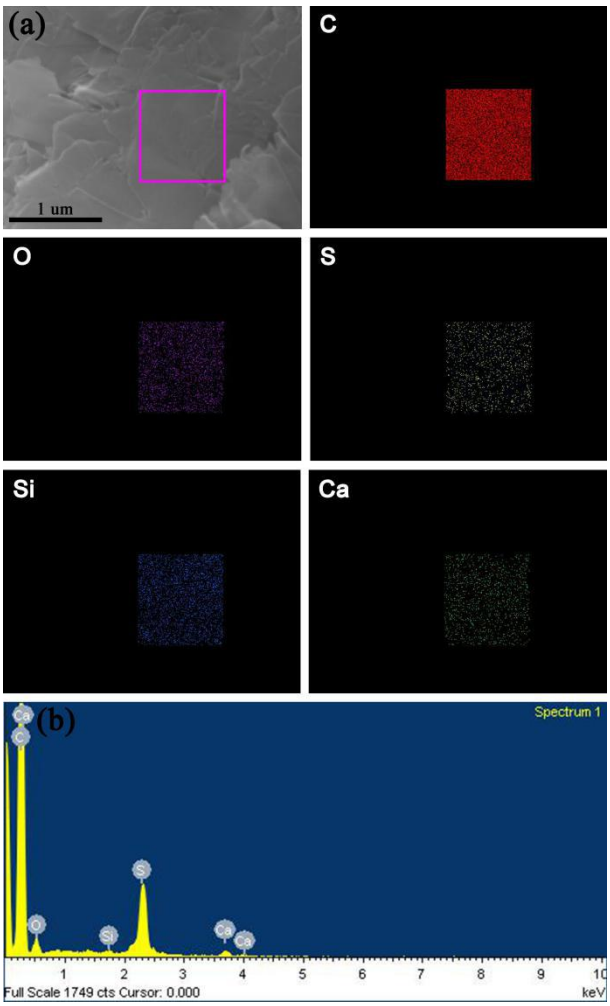

Figure 6.4 (a) SEM image together with the corresponding EDS elemental mappings, and (b) EDS spectrum of the HGC.

6.3.2 Electrochemical properties for lithium storage

Starting from the aforementioned electro-optical characterizations, we argue that the obtained HGC characterized by high graphitization degree, mesoporous structure, high surface area and slight S-doping might indeed endow with good electrochemical lithium storage performance as LIBs anode. The assembled LIBs were discharged and charged galvanostatically in a narrow voltage range of 0.01–1.5 V (*vs.* Li^+/Li) instead of the widely used 0.01 V to 2.5 V or even 3 V as we were aiming for realistic applications. For the first discharge profile (Figure 6.5), three plateaus at about 1.7, 0.75, and 0.1 V can be observed, which are due to the reaction of chemically bonded sulfur with Li^+,[23,31] electrolyte decomposition and formation of a solid electrolyte interface (SEI) film on the surface of active materials,[21,26] and to the insertion of Li^+ into graphitic layers,[21,32] respectively. Upon the subsequent charge process, a plateau at around 0.1 and a sloped curve above 0.3 V are observed, delivering a charge (reversible) capacity of 296.9 mAh g^{-1} at the current density of 50 mA g^{-1} when the charge cut-off potential is set at 1.5 V. Meanwhile, a large initial irreversible capacity loss could be observed, a common feature for carbon-based materials which can generally be assigned to the formation of a SEI layer. To be noticed that due to the choice of adopting a narrow voltage range, the reaction during the first cycle between chemically bonded sulfur with Li^+ determines a strongly irreversible reaction, which in turn partially contributes to the cell capacity loss. After the first cycle the capacity becomes stable showing also a highly reversible process, as evidenced by the overlapped charge/discharge curves shown in Figure 6.6a. Even though the reversible capacity of HGC as anode for LIBs is considerably lower than those of previously reported carbon-based materials[5,18,21,32] due to the narrow voltage range adopted in this work, the HGC exhibits excellent cycling stability (Figure 6.6b). The initial Coulombic efficiency (CE) is relatively low of 33.5% in comparison to standard graphite anodes, which can be attributed to the relatively large surface area of mesoporous HGC as well as to the existence of disorders in the structures.[21] The CE of the second cycle increases dramatically to 87% and further to more than 95% after

5 cycles. After 100 cycles at the current density of 50 mA g^{-1} the reversible capacity of HGC is 273.5 mAh g^{-1} with a CE close to 99.5%.

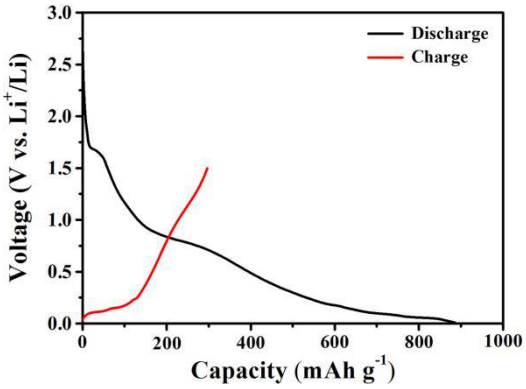

Figure 6.5 The initial galvanostatic charge-discharge voltage profiles at the current density of 50 mA g^{-1} for the HGC electrode when applied to LIBs.

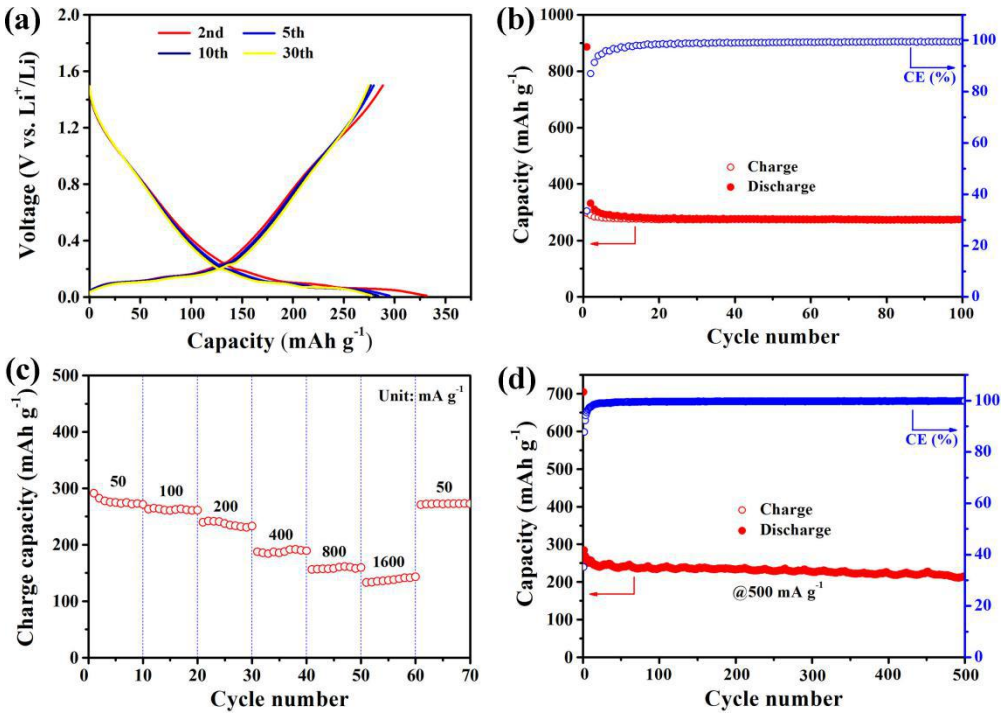

Figure 6.6 Electrochemical performances of HGC electrode for LIBs. (a) Galvanostatic charge-discharge voltage profiles for selected cycles at the current density of 50 mA g^{-1}, (b) cycling performance and CE at 50 mA g^{-1}, (c) rate performance at various current densities, and (d) cycle performance and CE at the high current density of 500 mA g^{-1}. Cut-off potentials: 0.01 and 1.5 V.

In order to investigate the possibility of applying HGC to high power LIBs, its

rate performance was evaluated at elevated current densities up to 1600 mA g^{-1}. As shown in Figure 6.6c, the HGC displays an excellent rate capability with reversible capacities of 276.6, 262.3, 236.6, 188, 158.5, and 137.8 mAh g^{-1} at 50, 100, 200, 400, 800, and 1600 mA g^{-1}, respectively. Importantly, when the current density was changed back to the initial 50 mA g^{-1}, the corresponding capacity was recovered almost entirely by settling to a value equal to 272.4 mAh g^{-1}, very similar to the initial 276.6 mAh g^{-1}. This reversible capacity capability demonstrates that the HGC electrode is characterized by a robust electrochemical structure resulting in a good stability even after high rate cycling. Furthermore, a 500 cycles long cycle analysis of HGC at the high current density of 500 mA g^{-1} was also conducted, as depicted in Figure 6.6d. The HGC showed good cycling stability for over 500 cycles with a reversible capacity of 214.2 mAh g^{-1}. The average CE after the first cycle was about 99.6%.

6.3.3 Electrochemical properties for sodium storage

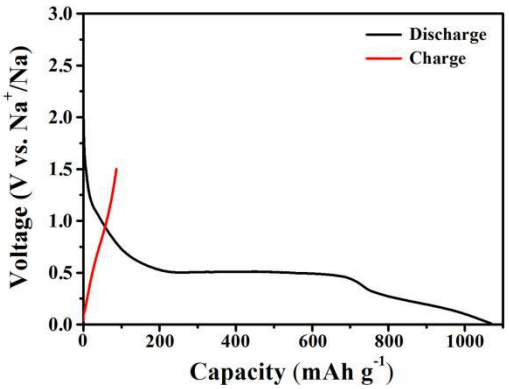

Figure 6.7 The initial galvanostatic charge-discharge voltage profiles at the current density of 50 mA g^{-1} for the HGC electrode when applied to NIBs.

Besides the possibility of employing HGC within LIBs, their effectiveness was also tentatively investigated within sodium-storage systems as the emerging SIBs technology is known to carry the prominent advantage of cost effectiveness even though at expense of electrochemical performance.[33] The galvanostatic charge-discharge profiles are illustrated in Figure 6.7. Here a long discharge plateau at

about 0.5 V (*vs.* Na^+/Na) is observed in the first cycle due to the decomposition of electrolyte on the surface of the carbon material resulting in SEI film formation. The initial reversible capacity is found to be 86.5 mAh g^{-1} at 50 mA g^{-1}, much lower than that for LIBs. During the subsequent cycles (Figure 6.8a), the HGC shows sloped charge/discharge voltage profiles without visible plateaus with the reversible capacity becoming fairly stable. Interestingly, a difference can be found when comparing the charge/discharge voltage profiles for LIBs and SIBs, is that the voltage plateaus below 0.2 V for LIBs is absent for SIBs, which could explain the lower sodium storage capacity. The relatively low capacity for sodium storage reflects that HGC is possibly not suitable for SIBs due to the absence of stable Na–C binary compounds and to the relatively large Na^+ ion dimension that makes Na^+ ions difficult to be intercalated into graphite.[33] Nevertheless, owing to the existence of numerous pores and defects inside HGC, a stable reversible capacity around 81 mAh g^{-1} with CE close to 98% during cycling at 50 mA g^{-1} could be delivered (Figure 6.8b).

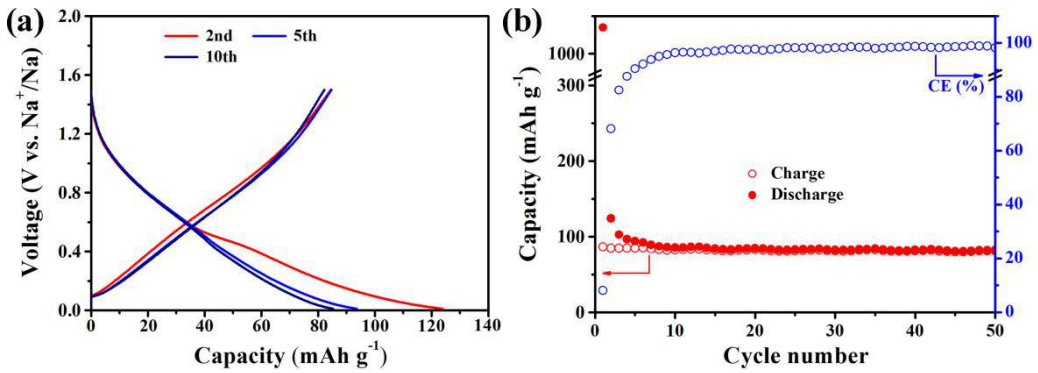

Figure 6.8 Electrochemical performances of HGC electrode for NIBs. (a) Galvanostatic charge-discharge voltage profiles for selected cycles at the current density of 50 mA g^{-1} and (b) cycling performance and CE at 50 mA g^{-1}. Cut-off potentials: 0.01 and 1.5 V.

6.4 Conclusions

In summary, a facile and economical route to prepare highly graphitized carbon from low cost CaC_2 at moderate temperature was developed. The CaC_2-derived carbon is characterized by a high graphitization degree and it mainly consists of 3D mesoporous

frameworks and 2D nanosheets. The synthesized HGC, once employed as anode material for rechargeable LIBs, exhibits excellent lithium storage performance with reversible capacity of 272.4 mAh g^{-1} at 50 mA g^{-1} after 100 cycles and 214.2 mAh g^{-1} at the high current density of 500 mA g^{-1} after 500 cycles as well as a good rate capability. Furthermore, the sodium-storage behavior of HGC was also investigated, resulting in a limited electrochemical performance due to the high graphitization degree. Finally, we expect that the introduced approach to prepare carbon materials from CaC_2 could be especially exploited by the carbon industry with also the consequence of possibly broadening the research and development on other kinds of carbides.

6.5 References

1. V. Georgakilas, J.A. Perman, J. Tucek, R. Zboril, *Chem. Rev.* 115 (2015) 4744–4822.
2. Y. Gogotsi, V. Presser, Carbon Nanomaterials, CRC Taylor & Francis, Boca Raton, 2013.
3. W. Gu, G. Yushin, *WIREs Energy Environ.* 3 (2014) 424–473.
4. V. Presser, M. Heon, Y. Gogotsi, *Adv. Funct. Mater.* 21 (2011) 810–833.
5. Z. Kou, B. Guo, Y. Zhao, S. Huang, T. Meng, J. Zhang, et al., *ACS Appl. Mater. Interfaces* 9 (2017) 3702–3712.
6. A. Tolosa, B. Kruner, S. Fleischmann, N. Jackel, M. Zeiger, M. Aslan, et al., *J. Mater. Chem. A* 4 (2016) 16003–16016.
7. E. Zera, W. Nickel, G.P. Hao, L. Vanzetti, S. Kaskel, G.D. Soraru, *J. Mater. Chem. A* 4 (2016) 4525–4533.
8. J. Xu, C. Wu, P. Yan, J. Wang, R. Zhang, X. Zhang, et al., *Electrochim. Acta* 174 (2015) 411–416.
9. J. Xu, R. Zhang, P. Chen, S. Ge, *J. Power Sources* 246 (2014) 132–140.
10. C. Wu, J. Gao, Q. Zhao, Y. Zhang, Y. Bai, X. Wang, et al., *J. Power Sources* 269 (2014) 818–824.
11. C. Dai, X. Wang, Y. Wang, N. Li, J. Wei, *Mater. Chem. Phys.* 112 (2008) 461–465.
12. L. Zheng, Y. Wang, X. Wang, N. Li, H. An, H. Chen, et al., *J. Power Sources* 195 (2010) 1747–1752.
13. L. Zheng, Y. Wang, X. Wang, X. Wang, H. An, L. Yi, *J. Mater. Sci.* 45 (2010)

6030–6037.

14. Y. Xie, Q. Huang, B. Huang, *Carbon* 48 (2010) 2023–2029.
15. Y. Li, Q. Liu, W. Li, H. Meng, Y. Lu, C. Li, *ACS Appl. Mater. Interfaces* 9 (2017) 3895–3901.
16. Y. Xie, Q. Huang, B. Huang, *Carbon* 47 (2009) 2292–2295.
17. H.L. Zhu, Y.J. Bai, Y.X. Qi, N. Lun, Y. Zhu, *Carbon* 50 (2012) 1871–1878.
18. F.D. Han, B. Yao, Y.J. Bai, *J. Phys. Chem. C* 115 (2011) 8923–8927.
19. D. Osetzky, *Carbon* 12 (1974) 517–523.
20. N.F. Fedorov, G.K. Ivakhnyuk, V.V. Samonin, *J. Appl. Chem. USSR* 54 (1981) 2253–2255.
21. R. He, Z. Wang, X. Jin, *Carbon* 116 (2017) 246–254.
22. Y. Chen, Q. Xu, Q. Song, H. Li, Z. Ning, X. Lu, et al., *Electrochem. Commun.* 64 (2016) 1–4.
23. T. Li, C. Wei, Y.M. Wu, F.D. Han, Y.X. Qi, H.L. Zhu, et al., *ACS Appl. Mater. Interfaces* 7 (2015) 5107–5115.
24. Y. Zhou, R. Ma, S.L. Candelaria, J. Wang, Q. Liu, E. Uchaker, et al., *J. Power Sourc*es 314 (2016) 39–48.
25. D. Zhang, Y. Hao, L. Zheng, Y. Ma, H. Feng, H. Luo, *J. Mater. Chem. A* 1 (2013) 7584–7591.
26. W. Ai, Z. Luo, J. Jiang, J. Zhu, Z. Du, Z. Fan, et al., *Adv. Mater.* 26 (2014) 6186–6192.
27. M. Thommes, K. Kaneko, A.V. Neimark, J.P. Olivier, F. Rodriguez-Reinoso, J. Rouquerol, et al., *Pure Appl. Chem.* 87 (2015) 1051–1069.
28. S. Song, F. Ma, G. Wu, D. Ma, W. Geng, J. Wan, *J. Mater. Chem. A* 3 (2015) 18154–18162.
29. K.J. Hong, S.O. Kim, *Energy Storage Mater.* 2 (2016) 27–34.
30. T. Li, N. Lun, Y.X. Qi, C. Wei, Y.K. Sun, H.L. Zhu, et al., *J. Power Sources* 273 (2015) 472–478.
31. S. Zheng, P. Han, Z. Han, H. Zhang, Z. Tang, J. Yang, *Sci. Rep.* 4 (2014) 4842.
32. L. Huang, Q. Guan, J. Cheng, C. Li, W. Ni, Z. Wang, et al., *Chem. Eng. J.* 334 (2018) 682–690.
33. W. Wang, W. Li, S. Wang, Z. Miao, H.K. Liu, S. Chou, *J. Mater. Chem. A* 6 (2018) 6183–6205.

Chapter 7 Summary and outlook

The work in this thesis has investigated various anode materials for NIBs from different aspects, which presents fundamental studies focused on surface and interface engineering of anatase TiO_2, degradation mechanisms that occur in alloy-type anode of Sn during sodiation-desodiation, and facile synthesis of carbon materials from low cost carbon source of CaC_2 as well as its application for NIBs and LIBs.

In Chapter 3 and Chapter 4, to improve the electrochemical performance of anatase TiO_2 by cost-effective fabrication approach, nanostructured anatase TiO_2 was simply prepared and modified by a facile surface modification approach of Al_2O_3 coating and a dual-modification approach of Mo doping combined with AlF_3 coating, respectively. In Chapter 3, the influence of different electrolytes and the role of Al_2O_3 surface coating were investigated. The Al_2O_3-modified TiO_2 exhibited enhanced cycling performance compared to the pristine one owing to the irreversible formation of Na−Al−O surface layer after sodiation which was confirmed by post-mortem XPS analysis. The study on the influence of different solvents on the electrode cycling performance revealed that the binary EC:PC solvent mixture could lead to an excellent cyclability with no need of the commonly used FEC additive. In Chapter 4, the as-prepared dually modified TiO_2 sample exhibited significantly enhanced sodium storage performance comparing with the pristine and single Mo-doped TiO_2, benefiting from the combined positive impacts of Mo doping and AlF_3 surface coating. This study revealed that AlF_3 coating is effective to enhance the sodium storage capability and the dual-modification approach is indeed more desirable compared to the single one. All these results suggest the importance of a proper surface and interface engineering in enhancing the performance of NIB anodes. Particularly, in future design of composite anode materials for NIBs, besides the benefits from surface engineering of the electrode materials we should also consider the boundary conditions such as the employed electrolytic solutions.

In Chapter 5, the Na-ion diffusivity and mechanical instability in Sn was investigated by employing a Sn thick film as the anode, which revealed three main damage mechanisms resulting from the sodiation: dry lake-bed fracture, pore formation and whisker nucleation. This is a unique result, as no other studies have reported the formation of pores and whiskers during sodiation. The Sn whiskers can penetrate the separator and short-circuit the electrochemical cell, thus may be a safety concern for NIBs and should be further examined in porous electrodes that use Sn as the active material. Nanopore formation has not been highlighted before as a damage mechanism during sodiation and may explain the capacity fade observed in nanostructured Sn particles in porous electrodes that do not display fracture. Furthermore, the planar geometry of the present Sn anodes allowed a first estimate to be obtained for the diffusion coefficient of Na^+ in Sn as 6.45×10^{-12} cm^2 s^{-1}.

In Chapter 6, we developed a facile and economical route to prepare carbon materials from low cost CaC_2 at moderate temperature by using a sulfur-based reaction. The as-prepared carbon was comprehensively analyzed by various techniques, showing that it is characterized by a high graphitization degree and mainly consisted of 3D mesoporous frameworks and 2D nanosheets. When used as anode materials for NIBs, it displayed relatively low capacity, however, it exhibited excellent lithium storage performance with high reversible capacity as well as a good rate capability. Highly graphitized carbon is not suitable for NIBs because of the relatively large Na^+ ion. Hard carbon as NIB anode is more appealing. However, we expect that the introduced approach to prepare carbon materials from CaC_2 could be especially exploited by the carbon industry with also the consequence of possibly broadening the research and development on other kinds of carbides.

In summary, the fundamental studies on various NIB anodes in this thesis could help us better understand the importance of surface and interface engineering in improving the electrochemical performance and rational design of micro-/nano-structures and/or nanocomposites for advanced NIB anodes. Of course,

in request of suitable anode materials for NIBs, a great deal of work needs to be done:

(1) develop an advanced synthetic methodology characterized by low cost and good scalability;

(2) explore new electrode materials with high performance;

(3) to better understand the sodium mechanisms of the anode materials by using DFT methods, nuclear magnetic resonance (NMR) spectroscopy, X-ray adsorption spectroscopy (XAS), Mossbauer spectroscopy and other techniques;

(4) in-depth studies of the structure and kinetics of electrode materials and the electrode/electrolyte interfaces with the help of advanced characterization techniques, particularly *in situ* techniques, such as X-ray diffraction, neutron diffraction, soft X-ray absorption spectroscopy, and Raman spectroscopy;

(5) prototype work for full-cell NIB technology is needed. In consideration of currently most of the work is based on Na half cells, it is essential to evaluate the performance of the electrode materials in full cell NIBs with the aim of improving the energy density of a NIB system thus promoting the commercialization of NIBs.

Appendix A Publications

1. **T. Li***, U. Gulzar, X. Bai, S. Monaco, G. Longoni, M. Prato, S. Marras, Z. Dang, C. Claudio, R.P. Zaccaria*, Surface and interface engineering of anatase TiO_2 anode for sodium-ion batteries through Al_2O_3 surface modification and wise electrolyte selection, *J. Power Sources* 2018, **384**, 18−26.

2. **T. Li**, U. Gulzar*, X. Bai, M. Lenocini, K.E. Aifantis, C. Capiglia*, R.P. Zaccaria, Insight on the failure mechanism of Sn electrodes for sodium-ion batteries: evidence of pore formation during sodiation and crack formation during desodiation, *ACS Appl. Energy Mater.* 2019, **2**, 860−866.

3. **T. Li**, U. Gulzar, R.P. Zaccaria, C. Capiglia*, S.A. Hackney, K.E. Aifantis*, Determining the Na^+ diffusivity in Sn anodes and probing the damage mechanisms of sodiation, in preparation

4. **T. Li***, X. Bai, U. Gulzar, Z. Dang, M. Prato, S. Marras, C. Capiglia, R.P. Zaccaria*, Towards enhanced sodium storage of anatase TiO_2 via a dual-modification approach of Mo doping combined with AlF_3 coating, in preparation

5. **T. Li**, X. Bai, U. Gulzar, C. Capiglia, Y.-J. Bai*, R.P. Zaccaria*, Facile synthesis of highly graphitized carbon via reaction of CaC_2 with sulfur and its application for lithium/sodium-ion batteries, *J. Power Sources* under review

6. **T. Li**, X. Bai, U. Gulzar, G. Longoni, Y.-J. Bai*, C. Capiglia*, W. Deng, X. Zhou, Z. Liu, Z. Feng, R.P. Zaccaria*, A comprehensive understanding of lithium-sulphur batteries technology, *Adv. Funct. Mater.* under review

7. U. Gulzar, **T. Li**, X. Bai, S. Goriparti, R. Brescia, C. Capiglia*, R.P. Zaccaria, Nitrogen-doped single wall carbon nanohorns enabling effective utilization of Ge nanocrystals for next generation lithium ion batteries, *Electrochim. Acta* 2019, **298**, 89−96.

8. U. Gulzar, **T. Li**, X. Bai, M. Colombo, A. Ansaldo, S. Marras, M. Prato, S. Goriparti, C. Capiglia*, R.P. Zaccaria, Nitrogen-doped single-walled carbon nanohorns as a cost-effective carbon host toward high-performance lithium−sulfur batteries, *ACS Appl. Mater. Interfaces* 2018, **10**, 5551−5559.

9. X. Bai$^{\perp}$, **T. Li**$^{\perp}$, Z. Dang, Y.-X. Qi, N. Lun, Y.-J. Bai*, Ionic conductor of Li_2SiO_3 as an effective dual-functional modifier to optimize the electrochemical performance of $Li_4Ti_5O_{12}$ for high-performance Li-ion batteries, *ACS Appl. Mater. Interfaces* 2017, **9**, 1426−1436. (co-first author)

10. U. Gulzar, S. Goriparti, E. Miele, **T. Li** , G. Maidecchi, A. Toma, F. De Angelis, C. Capiglia*, R.P. Zaccaria*, Next-generation textiles: from embedded supercapacitors to lithium ion batteries, *J. Mater. Chem. A* 2016, **4**, 16771−16800.

11. X. Bai, **T. Li**, U. Gulzar, R.P. Zaccaria, C. Capiglia, Y.-J. Bai*, Comprehensive understanding lithium-sulfur batteries: current status and outlooks, *Advanced Battery Materials*, 355−398, Chunwen Sun (ed.), 2019 WILEY-Scrivener Publishing LLC, USA. Book chapter http://www.vbripress.com/book/amseries/